Nonparametric Imaging Algorithms for UWB Pulse Radars

by

Takuya Sakamoto

Acknowledgments

Preface

Recently, ITS (Intelligent Transport System) has attracted great attention. It is hoped that developing technologies for ITS will lead to an intelligent automobile which can drive itself autonomously. They require techniques of environment measurement. Moreover, it is supposed that rescue robots in the future will be able to go into places in which people cannot go because of a hostile environment. Such robots require techniques of 3-dimensional imaging for locationing. Above-mentioned applications require accurate and reliable measurement method because they affect human's life. Radars utilizing ultra-wide-band (UWB) pulses are attractive as an environment measurement method for various applications including the examples described above. Pulse radars have an advantage that they can be used even in critical situations where optical techniques cannot be used. Additionally, they can be used even in dense smoke, fog, vegetations and so on. Pulse radars are used as ground penetrating radars (GPRs) also, which is important for detecting pipes in built-up areas, as well as for archaeological inspection.

Estimating target shapes using waveform data, which we obtain by scanning an omni-directional antenna, is known as one of ill-posed inverse problems. Parametric methods such as the model-fitting method have problems concerning calculation time and stability. We propose fast and stable non-parametric algorithms for high-resolution estimation of target shapes in order to solve the problems of parametric algorithms. First, we investigate accurate estimation of point targets by estimating target locations and scattered waveforms, simultaneously. Suitable filtering is essential for accurate ranging, which requires an accurate waveform estimation. We present a high-resolution estimation algorithm IHCT (Iterative Hyperbolic Coherent Transform) which estimates target location and scattered waveforms, whose accuracies are interdependent. This technique relies on iterative improvements of estimated waveforms. The performance of the algorithm is contrasted with conventional ones and statistical bounds. Next, we clarify the problem of applying IHCT to multiple targets. Coherently integrated signals for multiple targets can not be used as an estimated waveform because of interference waves from other targets. We propose an interference suppression algorithm based on a neural network, and show an application example of the algorithm.

Next, we propose a fast imaging algorithm, SEABED, which can estimate target shapes accurately. We clarify the existence of a reversible transform between target shapes and delay time, which we call BST (Boundary Scattering Transform). SEABED is based on

the BST which enables quick and accurate estimation. We show application examples of SEABED algorithm with numerical simulations. The performance of SEABED algorithm for inhomogeneous media is also studied.

High-resolution imaging algorithms including SEABED algorithm utilize the carrier phase of received signals. However, their estimation accuracy suffers degradation due to phase rotation of the received signal because the phase depends on the shape of the target. We propose a phase compensation algorithm for high-resolution pulse radar systems. This algorithm improves the estimation accuracy without sacrificing the resolution using the proposed algorithm.

Pulse radars are promising candidates for 3-dimensional environment measurement also, which is required for autonomous robots. Estimating 3-dimensional target shapes by scanning an omni-directional antenna is a more difficult task than estimation of 2-dimensional shapes. We have clarified the existence of a reversible transform between received data and target shapes for 3-dimensional systems as well as in 2-dimensional systems. The calculation time can be remarkably reduced by applying this transform because the transform directly estimates target shapes. We propose a new algorithm 3-D SEABED, based on the transform and show an application example using numerical simulations.

Contents

List of Tables

List of Figures

Chapter 1

General Introduction

1.1 Introduction

Over 100 million anti-personnel mines are embedded in over 70 countries. About 24000 people are killed or injured every year by these anti-personnel mines. It is desirable to detect and recognize all anti-personnel mines and get rid of them. Over 8000 and 40000 people are killed by traffic accidents per year in Japan and the United States, respectively. It is expected to realize an intelligent automobile which can drive itself autonomously and safely in the near future. It is hoped that rescue robots will work instead of humans in hazardous areas to save people. However, they have not been realized yet because of the difficulties of developing this technology. One of the difficulties is related to environment recognition, which requires imaging techniques. Radar imaging is one of the most interesting topics because they have a great deal of possibility for many applications including the above-mentioned ones. We study the UWB pulse radar technique as a promising candidate for these purposes in the present study. We develop efficient algorithms to realize an innovative technology.

1.2 Locationing for Robots

In robotics, it is indispensable to recognize 3-dimensional objects. This recognition process requires high spatial resolution and a longer range, especially for robotics problems. Various kinds of sensing techniques for robots have been studied already, as reviewed in [1]. Widely used types of sensing in robotics are the following:

- Active triangulation

- Laser range finders

- Passive optical imaging

- Ultrasonic sensing

- Radars

The requirements of sensing techniques for robotics are the following:

- Speed (Data acquisition speed should be high.)

- Integration (Physical packaging should be small.)

- Robustness (Sensors should work in difficult environment conditions.)

Robustness of the sensors in low-light, dust, fog, etc. is important especially for rescue robots and autonomous driving cars.

1.2.1 Active Triangulation

Historically, the active triangulation technique is the first one which was applied to the range imaging for robotics. A laser is projected onto the scene, and a camera observes the scene. The depth z to the point is calculated as

$$z = \frac{B}{x_0/f + \tan\alpha}, \tag{1.1}$$

where B is the baseline separation of the laser and the camera optical centers, f is the focal length of the camera lens, x_0 is the laser spot location, and α is the projection angle of the laser. This technique has an advantage of simplicity in its implementation. However, it also has some critical problems as follows: 1) The illumination condition should be adjusted. 2) The frame rate of the scanners is restricted.

1.2.2 Laser Range Finders

The laser range finder is a powerful tool to obtain the range data. The laser range finder is mainly used indoors with mapping and localization techniques. Modulated laser beams are transmitted and their echoes are received, which is very similar to radar systems. We have to scan the laser beams to observe a wide range of targets because laser beams are highly directional. Laser range finders utilize mechanical motion for this scanning. As for signals, AM (Amplitude Modulation) lasers and FM-CW (Frequency Modulated Continuous Wave) lasers use an amplitude modulation and frequency modulation to measure the range, respectively. FM-CW lasers require complex design although their ranging is more accurate than that of AM lasers. AM lasers perform at a range of only tens of meters at most because they are sensitive to ambient natural light. Laser range finders have problems as follows 1) Output power is limited for eye safety. 2) Their sizes are comparatively large and heavy.
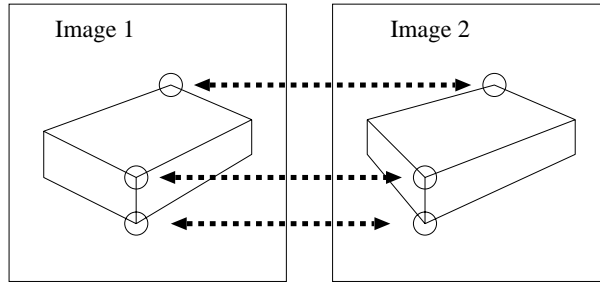
Figure 1.1: Extraction of corresponding points in multiple images.

One of the disadvantages of the scanning laser range finders, is the long data acquisition time due to the mechanical scanning mechanism. Several concepts have been proposed for non-mechanical scanning, one of which is AO (Acoustico-optical) devices for beam steering. AOs are crystals placed in the path of the laser beam, with which electric scanning is realized. This technique has disadvantages as follows: 1) Loss of power by AO device. 2) Complex optical effects affecting focusing and diffraction of the beam.

1.2.3   Passive Optical Imaging Techniques

Passive stereo vision is one of the oldest research topics in the computer vision community. Some kinds of techniques of 3-dimensional shape reconstruction with passive stereo cameras have been studied. Among them, the volumetric intersection method and stereo method are often used for this purpose [2]. The volumetric intersection method is based upon silhouettes constraint. The silhouettes constraint requires that the volume obtained by projecting the 2-dimensional image should contain the 3-dimensional target. The imaging accuracy of this technique is not sufficient although it requires relatively short calculation time. Nobuhara et al. [2] improved the accuracy of the 3-dimensional imaging by modifying the reconstructed image by the volumetric intersection method. They utilized a parametric deformable mesh model and updated the parameters to reduce the inconsistency of the image and observed data.

On the other hand, a stereo method needs to extract corresponding points among multiple images by searching through the image by comparing local neighborhoods [3]. The first step of the algorithm is to detect pairs of corresponding points in the multiple images as in Fig. 1.1. Next, the location of the points are expressed with some parameters which are solved using some algorithms such as a least-mean-square method. Many optimization algorithms have been studied for this purpose, which is reviewed by Sakaue et al. [4]. This can be translated as applying a triangulation technique, which enables us to estimate the range of the points. This technique has a limitation due to the triangulation geometry. It is difficult to select a suitably long baseline because of the trade-off between high resolution and reduced ambiguity in matching. Jeong et al. [5] proposed a fast

stereo matching technique. They utilized MAP (Maximum A Posteriori) estimation for the matching problem, and reduced this procedure to an unconstrained optimization problem. A variety of algorithms for passive stereo are reviewed by Dhond et al. [6]. Other passive optical imaging techniques with a camera images are reviewed in [7]. Depth estimation with only one image is also studied, which includes shape estimation using shading, texture, contour and focus/defocus.

Another optical locationing system utilizes curved mirrors with camera. It was reported to be effective for robot navigation to utilize omni-directional optical images by using mirrors [8]. Many kinds of shapes are proposed for the mirror, these being, a conical mirror, a spherical mirror, a hyperboloidal mirror and a paraboloidal mirror. Joochim et al. [9] proposed an imaging algorithm for robot navigation based on a polar coordinate transform from an omni-directional image obtained by a hyperboloidal mirror. They have shown the optical technique with a hyperboloidal mirror is effective for robots to avoid the obstacles.

Ukida et al. [10] proposed a unique optical imaging technique with 3 colored lights and an optical scanner. They proposed a 3D shape reconstruction system using three light sources which are red, green and blue. The target is illuminated by using these three lights from different places. Then, the image is obtained by an ordinary image scanner. Their system can accurately reconstruct the 3D shape of targets using experimental data. However, the accuracy of their method depends on the color of the target itself, which can be a serious problem.

Optical imaging techniques have an advantage that the cost of CCD (Charge-Coupled Device) cameras are getting cheaper. Passive stereo techniques have a remarkable advantage in size reduction, which makes it easy to implement them inside small robots. Ozawa [11] studied the feasibility of driving assistance with optical image signal processing. For example, the passive stereo techniques have been applied to the rovers Spirit and Opportunity in the Mars pathfinder project and the prototype robot Qrio made by Sony Inc. In this way, passive optical techniques are attractive imaging tools. However, they have some critical problems. First, the multiple cameras should be placed apart from each other to ensure the difference of the images obtained. The distance between the cameras depends on the distance to the target. Additionally, the algorithms have instability for some targets. For example, they cannot estimate the situation if the camera is placed in front of a monotone large object because corresponding points and silhouettes cannot be extracted from the observed image. Finally, they do not work in dense smoke or fog, which makes the optical technique unreliable, especially for rescue robots or autonomous driving car systems. The idea of sensor fusion with optical and radar techniques can be effective for robust observation, which enable us to solve the problems in both techniques.

1.2.4   Ultrasonic Techniques

Ultrasonic techniques are utilized for imaging especially for medical examination. Ultrasonic waves can penetrate human bodies, which makes it possible to reconstruct the image of invisible regions within our bodies. Ultrasonic can be also used for imaging of targets in the air. However, their application is restricted by the absorbing effect.

Ylitalo et al. [12] applied the near-field SAR (Synthetic Aperture Radar) algorithm to the experimental data for a monostatic system with 3.5MHz of ultrasonic signals.The cysts in a tissue-mimicking background were clearly reconstructed by their study. Yagle et al. [13] studied the feasibility of inverse problem algorithms for acoustic media. They defined a discrete Schrodinger equation and proposed algorithms for the inverse problems based on it. Lockwood et al. [14] studied a linear sensor array system for 3-dimensional imaging. They proposed a sparse array to reduce the number of transducers, which is also critical for real-time operation. Bronstein et al. [15] proposed a diffraction tomography algorithm for ultrasound imaging. They utilized NUFFT (NonUniform Fast Fourier Transform) to calculate the signal in the wave-number domain instead of using interpolation and extrapolation.

Compared to ultrasonic techniques, radar systems have advantages as follows: 1) Radiowaves can propagate further than ultrasonics, which have a significant loss in the air. 2) Polarimetric information can be used. On the other hand, ultrasonic systems can utilize comparatively slow sampling rate and signal processing, which is an advantage in regard to the cost and the power consumption. It is promising to develop sensor fusion techniques with sonar and radar systems because their performance can compensate the other's weak-points.

1.3   Ground Penetrating Radars

Many studies have also been done in developing radar techniques to detect and image underground targets. One of the objectives is mine detection, which is a serious problem. For example, Bosnia-Herzegovina has six million land mines buried throughout previous battle field sites. High-resolution imaging is required to safely remove all the land mines. Moreover, many pipes for gas and water; cables for communications and power supply; and other various objects are buried underground in most cities, which can lead to a critical accident when excavating tunnels and holes for construction. GPR (Ground Penetrating Radar) systems are promising to solve these social issues.

However, imaging algorithms for GPR have to solve problems of inhomogeneity because the relative permittivity and conductivity of the soil largely depend on the water content. If the media is able to be modeled by layered media, it can be dealt with by expressing them by some parameters. Catapano [16] proposed an imaging algorithm for homogeneous targets in stratified media. The attenuation characteristic of soil needs suitable selection of the signal frequency, which means that there is a trade-off between the

detectable range and the resolution. Most of the GPRs utilize baseband pulses which satisfy UWB conditions due to this trade-off. Nonplanar air-ground interface can also be a problem when the antenna is scanned apart from the interface. Walker et al. [17] proposed a non-iterative technique for compensating this effect by the PPB (Plane-to-Plane Backpropagation) method, which was derived by reformulating the time-domain SAR (Synthetic Aperture Radar) algorithm with Snell's law.

For the same purpose, seismic probing is also used, which utilizes the frequencies of 1-100Hz. Seismic probing can be applied to detection of buried pipes underground although it is used especially for geological investigations of natural resources. For seismic probing, migration algorithms are mainly used for imaging, which we describe in detail later.

1.4 Radar Signal Processing

1.4.1 Radar Systems for Robots

Fig. 1.2 shows a schematic block diagram of the radar system for robots. This system is almost the same as conventional bistatic radar systems. Note that the monostatic radar systems utilize one antenna as both, a transmit antenna and a receive antenna as shown in this figure. Multistatic radar systems utilize multiple receive antennas instead of one antenna in this figure. The signal processor is the place where imaging algorithm is implemented, whose output is the image of the environment of the robot. The image data is input into the actuators to move the robot itself, which changes the environment situation including the target directions. Therefore, real-time observation should be realized for the application to robots, which is the most important requirement for the imaging algorithm for robotics.

We assume two types of antenna placement in the present work. One is a multistatic radar system, which is used in Chapter 2. The other is a monostatic radar system, which is used in Chapter 3-5. Multistatic radar systems utilize multiple antennas for observation, which has an advantage that antenna scanning is not required. On the other hand, monostatic radar systems utilize only one antenna, which has advantages of the cost and size. Figs. 1.3 and 1.4 show the antenna placements for multistatic and monostatic radar systems, respectively.

1.4.2 Radiowave and Lightwave

Both of radiowaves and lightwaves belong to the electromagnetic waves. Radiowaves and lightwaves are defined as the electromagnetic waves with lower frequency and higher frequency, respectively. In general, the boundary of the frequency which divides them is around 3THz (the wavelength of 100μm). Optical techniques, including the laser range finders and the passive optical techniques, assume roughness of the target surfaces. Most of the objects around us in a daily life, which are walls, desks, floors and so on, can be
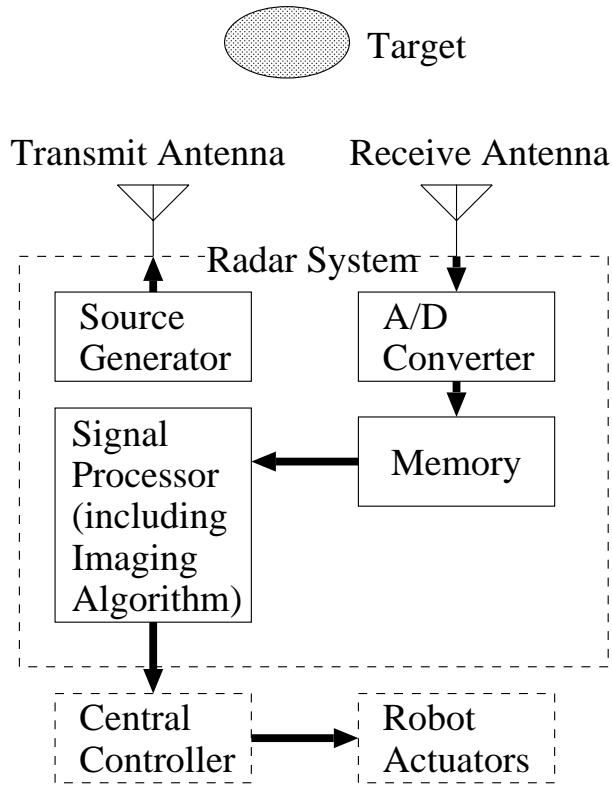
Figure 1.2: The radar system for robots.

assumed to be rough surface for the wavelength of lightwaves. As for the laser range finders, this feature enables us to observe the distance to a target without scanning the laser source. On the other hand, for the wavelength of radiowaves, the target surfaces are often smooth just like mirrors for lightwaves. Therefore, we can observe the echoes only from the points with the stationary phase and non-continuous boundaries. Fig. 1.5 shows a raypathes of laser lightwaves and radiowaves for certain objects. Fig. 1.6 shows a schematic table of the visible regions of a rectangular by using radiowaves and lightwaves. Radiowaves can observe the reflection echo and the diffraction echoes from the non-continuous boundaries.

The laser range finders and the passive optical techniques can estimate the shape of the surface directly, although passive techniques may require some textures on the surface. To the contrary, radars cannot estimate the target surface directly except for the point of stationary phase. Radars can estimate target shapes by estimating the edge points instead of estimating the surface, which means that the target are modeled as a set of point targets. Radar cannot utilize sharp beams like the laser beams, and thus requires effective radar imaging algorithms. We deal with the locationing algorithm for

7
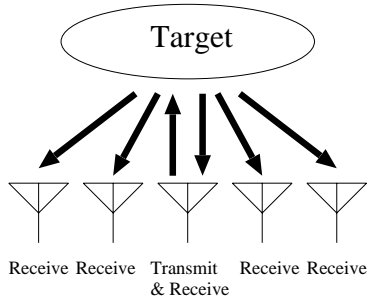
Figure 1.3: Antenna placement for multistatic radar systems.
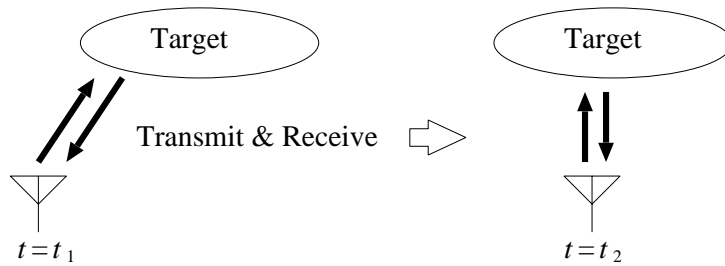
Figure 1.4: Antenna placement for monostatic radar systems.

point targets in the present study. Furthermore, we also utilize the characteristic of the reflection and the diffraction echoes, to develop a reversible transform for fast and accurate imaging of continuous bodies.

1.4.3   Ultra Wideband Signals

FCC (Federal Communications Commission) has set a standard for UWB (Ultra Wide Band) technologies in 2002. Ultra wide band is defined by the FCC in Part 15 regulations. Part 15 regulations of the FCC contain all updates and changes made by the Commission as of May 30, 2002. A UWB signal is defined in Part 15 regulations as follows:

- Bandwidth. For the purpose of this subpart, the bandwidth is the frequency band bounded by the points that are 10 dB below the highest radiated emission, as based on the complete transmission system including the antenna. The upper boundary is designated f_H and the lower boundary is designated f_L. The frequency at which the highest radiated emission occurs is designated f_M.

- Center frequency. The center frequency, f_C, equals $(f_H + f_L)/2$.

- Fractional bandwidth. The fractional bandwidth equals $2(f_H - f_L)/(f_H + f_L)$.
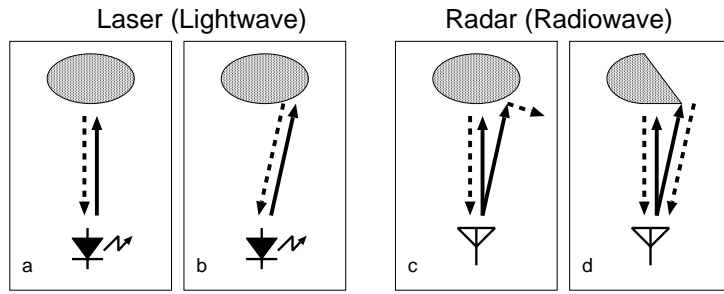
8

Figure 1.5: The ray pathes of radiowaves and lightwaves.

Figure 1.6: The visible region of a rectangular with radiowaves and lightwaves.

- Ultra wideband transmitter. An intentional radiator that, at any point in time, has a fractional bandwidth equal to or greater than 0.20 or has a bandwidth equal to or greater than 500 MHz, regardless of the fractional bandwidth.

Fig. 1.7 shows the limitation of the EIRP (Equivalent Isotropically Radiated Power) for the UWB signals. This definition is different from the definition by DARPA (Defense Advanced Research Projects Agency) in military technology communities, which is shown in Table. 1.1. It is a characteristic of UWB that any licenses are not required only if the output power is restricted within a certain limit. The output power density is limited to smaller than -41.3dBm/MHz for 3.1GHz to 10.6GHz in order to avoid the interference with the conventional wireless communication systems such as satellite communications and IEEE802.11a. UWB technologies are supposed to be applied to high-speed communication systems and high-resolution radar systems. Cramer et al. [18] studied the characteristics of UWB propagation for communication use.

The fundamental patent for a UWB technology was taken by Ross in 1973 [19]. The studies on UWB technologies have been done mainly for military use by 1990. However,
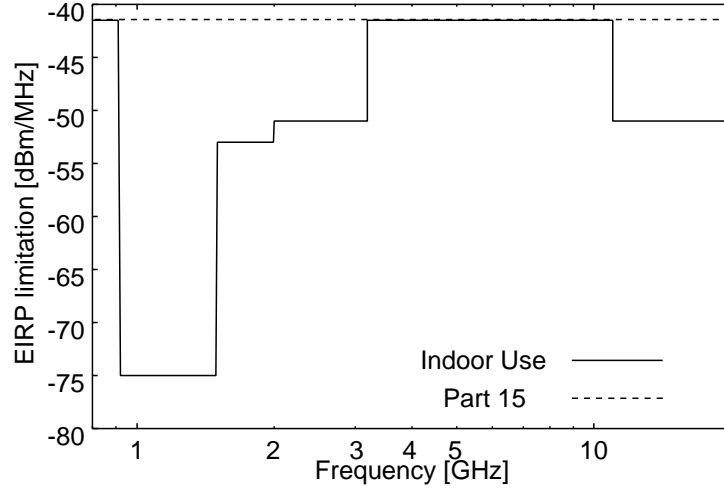
Figure 1.7: The limitation of EIRP for UWB technologies.

Table 1.1: Definitions of UWB.

	FCC	Military
Bandwidth	500 MHz	1.5 GHz
Fractional Bandwidth	20%	25%

the situation has changed suddenly after the FCC report on this technology, which opened a new possibilities of development for public welfare. UWB radars have a variety of applications including rescue robots and autonomously driving cars.

1.4.4 Matched Filter and Wiener Filter

Matched filters are often used for pulse radar systems, which maximize the S/N of the output signal. The matched filter $M(\omega)$ is expressed as

$$M(\omega) = G^*(\omega), \tag{1.2}$$

where $G(\omega)$ is the Fourier transform of the desired received waveform, and * denotes the complex conjugate of the variable. The matched filter can be regarded as a special case of the Wiener filter, which is expressed as

$$W(\omega) = \frac{G^*(\omega)}{(1 - \eta) + \eta |G(\omega)|^2}, \tag{1.3}$$

where η is a controlling parameter. If η is suitably selected, the output waveform of the Wiener filter becomes close to the Dirac's delta function in the criterion of least mean

square. The Wiener filter shrinks to the matched filter if the η is set to 0, which is effective for the signals with low S/N. We should note that both of the matched filter and the Wiener filter require the accurate waveform of the desired signal.

1.4.5 FDTD Method and Simulation Model

We utilize FDTD (Finite Difference Time Domain) method to calculate the received signal in numerical simulations. FDTD method is one of effective calculation algorithms for analysis of electromagnetic field [20]. Among many approaches to electromagnetic computation, including method of moments, finite element, geometric theory of diffraction, and physical optics, the FDTD technique is applicable to the widest range of problems.

The principle of FDTD method is following. Maxwell's equations are given as

$$\nabla \times \boldsymbol{E} = -\frac{\partial \boldsymbol{B}}{\partial t}, \tag{1.4}$$

$$\nabla \times \boldsymbol{H} = \boldsymbol{J} + \frac{\partial \boldsymbol{D}}{\partial t}, \tag{1.5}$$

where $\boldsymbol{E}$, $\boldsymbol{B}$, $\boldsymbol{H}$, $\boldsymbol{J}$, $\boldsymbol{D}$ and t are electric field, magnetic flux density, magnetic field, current density, electric flux density and time, respectively. We can denote $\boldsymbol{B} = \mu \boldsymbol{H}$ and $\boldsymbol{D} = \varepsilon \boldsymbol{E}$, where μ and ε are permittivity and permeability, in an isotropic medium. By utilizing these expressions, we can rewrite Maxwell's equations as

$$\nabla \times \boldsymbol{E} = -\mu \frac{\partial \boldsymbol{H}}{\partial t}, \tag{1.6}$$

$$\nabla \times \boldsymbol{H} = \boldsymbol{J} + \varepsilon \frac{\partial \boldsymbol{E}}{\partial t}. \tag{1.7}$$

The FDTD method discretizes time and space, where electric field and magnetic field are placed on the grids called Yee cell as shown in Fig. 1.8. We define $F^n(i,j,k)$ as the field F at a point $(x,y,z) = (i\Delta s, j\Delta s, k\Delta s)$ and time $t = n\Delta t$, where Δs and Δt are the space interval and the time interval, respectively. For example, the x component of Eq. (1.6) can be discretized as

$$\frac{H_x^{n+\frac{1}{2}}(i, j+\frac{1}{2}, k) - H_x^{n-\frac{1}{2}}(i, j+\frac{1}{2}, k)}{\Delta t} = -\frac{\dfrac{E_z^n(i, j+1, k)}{\mu(i, j+1, k)} - \dfrac{E_z^n(i, j, k)}{\mu(i, j, k)}}{\Delta s}$$
$$-\frac{\dfrac{E_y^n(i, j+\frac{1}{2}, k+\frac{1}{2})}{\mu(i, j, k)} - \dfrac{E_y^n(i, j+\frac{1}{2}, k-\frac{1}{2})}{\mu(i, j, k-1)}}{\Delta s}. \tag{1.8}$$

In the similar way, other components of the electromagnetic fields are updated at each time interval.

11
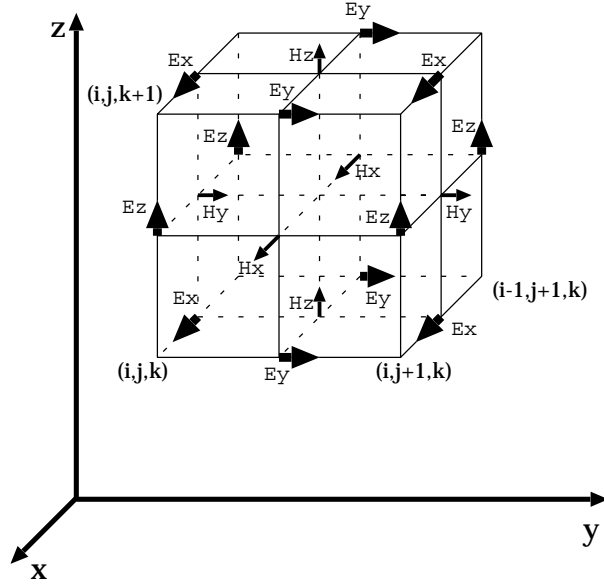
Figure 1.8: The Yee cell for FDTD method.

In the present study, we model a transmitting and receiving antenna as a grid with a forced current and a simple uniform grid, respectively. Mono-cycle pulses are often used as an impulse signal, which satisfy the condition of UWB signal. In order to generate a mono-cycle pulse, we set the waveform of the forced current $J_z(t)$ as

$$J_z(t) = -(1 + \cos(kt))\sin(kt), \tag{1.9}$$

for $-\pi \leq kt \leq \pi$ and $J_z(t) = 0$ otherwise. The waveform of $J_z(t)$ is shown in Fig. 1.9. The electric filed in far-field can be calculated as in Fig. 1.10, which can be used to determine the matched filter. The electric field E_z in the far-field satisfies

$$E_z(t) \propto \mathrm{j}\omega J_z(t), \tag{1.10}$$

where ω is the angular frequency of the signal. The term $\mathrm{j}\omega$ can be interpreted as a differential operator in this equation. Fig. 1.11 shows the waveform of the electric field observed at a point apart from the forced current by 4 wavelengthes at the center frequency of the pulse. The fractional bandwidth of this waveform is 96.3%, which satisfies the condition of UWB. We see that the third peak appears in this waveform, which does not exist in the current waveform. This is caused by the low-frequency-suppression effect of the radiation.

12
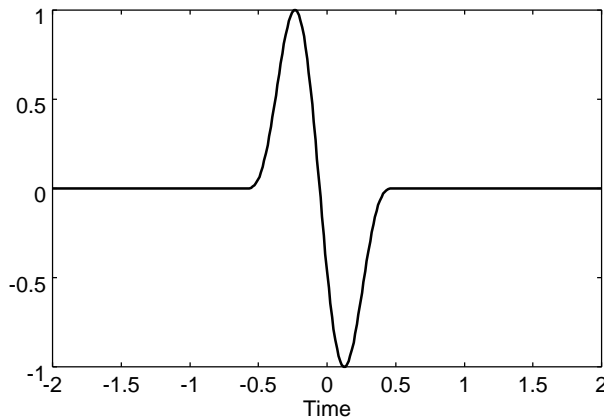
Figure 1.9: Current waveform at the transmitting point.
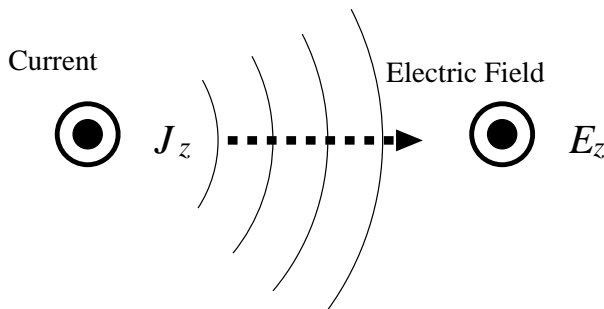
Figure 1.10: The source current and transmitted waveform.

1.4.6 Polarimetry for Imaging

electromagnetic waves have an advantage in its polarimetry. Utilizing polarization for imaging is helpful to discriminate and identify the shape of targets. Polarization property of a target is expressed by the scattering matrix (S-matrix) as

$$
\begin{pmatrix} E_x^{\mathrm{s}} \\ E_y^{\mathrm{s}} \end{pmatrix} = \begin{pmatrix} S_{xx} & S_{xy} \\ S_{yx} & S_{yy} \end{pmatrix} \begin{pmatrix} E_x^{\mathrm{i}} \\ E_y^{\mathrm{i}} \end{pmatrix},
\tag{1.11}
$$

where $(E_x^{\mathrm{i}}, E_y^{\mathrm{i}})^{\mathrm{T}}$ is the incident field, and $(E_x^{\mathrm{s}}, E_y^{\mathrm{s}})^{\mathrm{T}}$ is the scattered field. For example, the S-matrix of a pipe with the direction of x has a characteristic $S_{xx} > S_{yy}$ and $S_{xy} \simeq S_{yx}$ [21]. As for the S-matrix of a plate, $S_{xx} \simeq S_{yy}$ and $S_{xy} > S_{yx}$ or $S_{xy} < S_{yx}$ may be observed, although these characteristics depend on the direction of the plate. Suwa et al. [22] developed a frequency extrapolation using polarization characteristics. Frequency extrapolation is one of high-resolution techniques for band-limited systems.

13
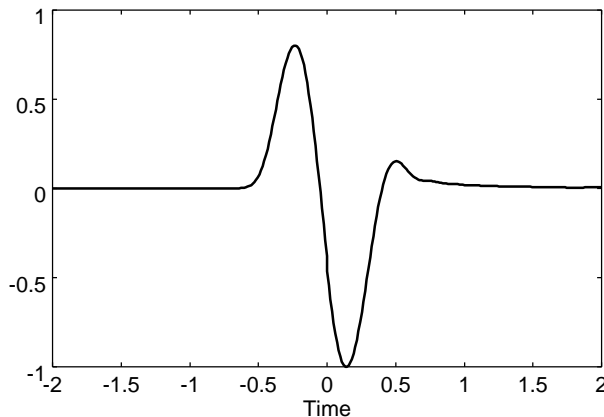
Figure 1.11: Transmitted waveform at the far zone from the antenna.

1.5 Inverse Problem and Algorithms

1.5.1 Inverse Problem

Estimating target shapes using signals obtained by a scanned omni-directional antenna is known as one of ill-posed inverse problems. Inverse problems are called so because it is the opposite concept of forward problems. Many physical problems are described with an integral equation such as

$$\int_{\tau_0}^{\tau_1} f(\tau)h(t,\tau)\mathrm{d}\tau = g(t), \tag{1.12}$$

where $f(\tau)$ is the system, $h(t,\tau)$ is the input and $g(t)$ is the output. Eq. (1.12) is called a Fredholm integral equation of the first kind. We have to solve this equation using a numerical approach because no analytical solution is known.

It is defined as a forward problem to estimate the output $g(t)$ when the system $h(\tau)$ and the input $f(t,\tau)$ are given as in Fig. 1.12. For example, estimation of electric field can be done by many algorithms such as FDTD or moment method, which are forward problems. It is comparatively easy to estimate the electric field if the media and the targets are given although it may take a long calculation time depending on the algorithm. Moreover, the solution is accurate and stable to some extent.

To the contrary, estimating target shapes using the signals received at some places is called an inverse problem. This can be translated as estimating the system $f(\tau)$ when the input $h(t,\tau)$ and the output $g(t)$ are given. If the number of the input is too small, it is difficult to estimate the system accurately. Here, the number of the input is equivalent to a condition number, which is the number of the discretized variable t. In general, inverse problems are difficult because the obtained information is not sufficient for estimation, which requires some a priori information about the situation. On the other hand, if the

14
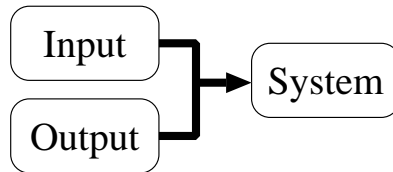
Figure 1.12: Forward problems and inverse problems.

condition number is too large, the solution can be unstable because we have to utilize a discrete algorithm instead of a continuous one as in Fig. 1.13. It is challenging to develop algorithms to solve inverse problems. Fig. 1.14 shows the concept of the ill-posed inverse problem in the field of radar imaging.

1.5.2 Target Models and Algorithms

First, we briefly explain the model types of imaging algorithms for radar systems. Every imaging algorithm needs a model to describe the target shape. Fig. 1.15 shows examples of target model. The left-hand side model in this figure is a grid model in which each grid has a permittivity (plus permeability and conductivity, if needed). The simplest kind of this model was proposed by Otto et al. [23], which was named LSF (Local Shape Function). They may be tensors if they are anisotropic materials. Anyway, the number of parameters to express the target are enormous depending on the required resolution and the dimension. Especially, it is difficult to express 3-dimensional target shape using this grid model. Instead, we can also use the boundary model with points in the right-hand side figure. In this model, we can reduce the number of parameters using a priori information that the targets have clear boundaries. It is obvious that this model can be used for limited range of targets and media. Ferraye et al. [24] proposed a completely different model called contour deformation with a level set method, about which we explain later.

15
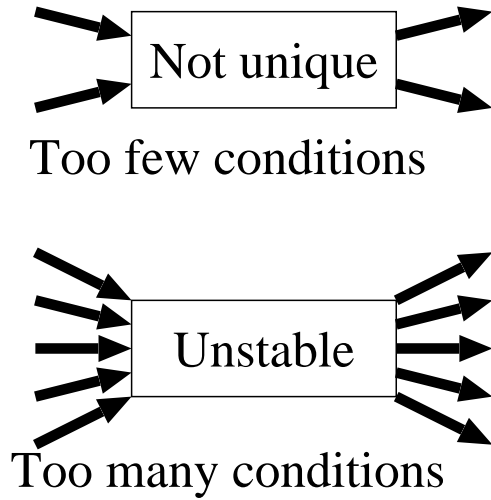
Figure 1.13: Condition number and inverse problem.
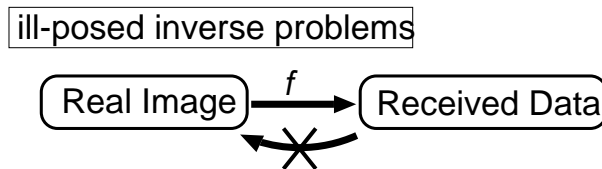
Figure 1.14: Ill-posed inverse problem in radar imaging.

Next, we have to determine the parameters of the model using the received signals and a priori information. The simplest technique is "parametric algorithms", which is based on optimization algorithms. This kind of algorithms update the parameters iteratively to minimize (or maximize) a certain evaluation function. The optimization process is done by conventional algorithms such as quasi-Newton method, Levenberg-Marquardt method, conjugate gradient method and its extensions. In spite of the simpleness of the basic idea of the parametric algorithms, the enormous calculation time is often unacceptable. Especially, even the boundary model may not be used in realtime in a 3-dimensional system. In order to avoid this difficulties, we should adopt another approach, which we call "nonparametric algorithms". This thesis proposes some nonparametric algorithms for quick imaging for UWB pulse radar systems.
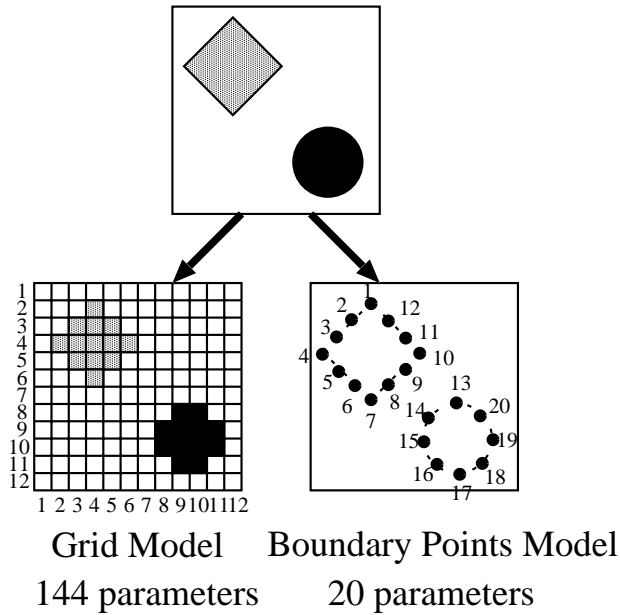
Figure 1.15: Target model and the number of parameters.

1.6 Imaging Algorithms for Radar Systems

1.6.1 Direction Finding and Point Locationing

Imaging of point targets is equal to estimating the target locations and their permittivity. The target location can be divided into two values: direction and range. In general, ranging is easier than estimation of the direction for UWB pulse radars because of its wide bandwidth. As for estimation of direction of arrival (DOA), a relatively large number of studies have been done, most of which assume far field and narrow bandwidth. They include MUSIC algorithm and ESPRIT algorithm, which are based on the idea of signal subspace. However, it is important for our purpose to deal with the DOA estimation problem within the near field and with a wide band. Hung et al. [25] and Sivanand et al. [26] proposed estimation methods of DOA with focussing matrices. Focussing matrices are used to make a valid covariance matrix for wide-band signals, in which we can obtain a coherent covariance matrices of difference frequency by multiplying a certain matrices. A similar technique was proposed by Gelli et al. [27]. They also utilized a new method to obtain a coherent combination of different frequencies. Their algorithm deals with wide-band signals. However, they assume independent sources and plane waves, which are not valid for our purpose.

Instead, some studies tried to estimate the location of a point target. It can be applied to locationing of pipes in 2-dimensional imaging. Schmidt proposed a point source local-

ization algorithm based on the idea of signal subspace, which is used for MUSIC algorithm [28]. Okada et al. [29] utilized the LoG (Laplacian of Gaussian) filtering algorithms known in the field of image processing for locationing of a circular target. They applied Laplacian of Gaussian filter to the actual data image and showed an application example to extract an underground pipe. Bermani et al. [30] proposed a detection method of cylindrical objects by means of neural networks. They also estimated the location, permittivity and the conductivity of the cylinder with a neural network by using the data obtained by receivers surrounding the target cylinder. Chen et al. [31] proposed a source localization algorithm based on maximum-likelihood criterion. Their algorithm assumed near-field targets and wide-band signals. Nagamune et al. [32] developed an imaging algorithm for embedded pipes based on a fuzzy expert system. Miwa et al. [33, 34] applied MUSIC algorithm to a borehole radar system for localization of cylindrical targets and point targets.They modified MUSIC algorithm to deal with a target near transmitting and receiving antennas. Liu et al. [35] also studied imaging technique for borehole radar systems. Quinquis [36] applied Fourier imaging technique, ESPRIT algorithm and MUSIC algorithm to get an image of complex-shaped target based on the idea that the target can be represented by some point targets. They utilized two receivers for one transmitter, which enable us to cancel the antenna characteristic by calculating the ratio of the two signals if the two receiver have the same property. Although the locationing algorithm of point sources is not sufficient for comprehensive imaging, their ideas are important.

1.6.2   Synthetic Aperture Radar

Synthetic aperture radar (SAR) systems are utilized for imaging of geography with airplanes and satellites [37]. Recently, the SAR techniques with polarimetry and interferometry have become an attractive topic for remote sensing fields [38, 39]. The techniques enable us to make a precise maps and the distribution of vegetation. This technique can be used for near-field imaging with UWB pulse radars. Bond et al. [40] applied this technique for a UWB pulse radar system for early detection of breast cancer.

In general, a small antenna has a wide beam, which restrict the minimum antenna size to achieve high-resolution imaging for conventional radar systems. SAR systems coherently integrate signals observed at various places, which realize an equivalent wide antenna aperture, or a sharp beam. Narayanan et al. [41] studied a SAR imaging algorithm for UWB radar systems, which is followed by their experimental application examples. Their experiment includes through-wall imaging, in which targets behind a wall was reconstructed although they are not clear. SAR techniques have been also applied to GPR systems, which realizes high horizontal resolution and improvement of S/N [21]. Fig. 1.16 shows the antenna and target locations in $x - y$ plane. We define the received signal $s(X, Y)$, where $(X, 0)$ is the antenna location and Y is the time normalized by signal prominent period. x, y and X all are normalized by the wavelength at the center frequency of the pulse. The SAR imaging algorithm for GPR systems can be expressed
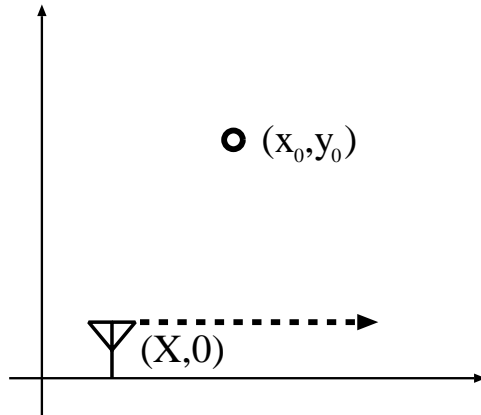
Figure 1.16: Antenna and target locations.

$$S(x,y) = \int_{-\infty}^{\infty} s(X, \sqrt{(X-x)^2 + y^2})\mathrm{d}X. \tag{1.13}$$

Fig. 1.17 and 1.18 show the target shape and the permittivity of the media for the application example of GPR SAR algorithm in Eq. (1.13). These figures are the same situation in Section 4, which enable us to contrast the results. Fig. 1.19 shows the reconstructed image by GPR SAR algorithm. We see many undesired response around the real target in this figure. These false images are caused by the interference between unrelated signals, which is an inherent problem of GPR SAR algorithm. Additionally, the calculation time for GPR SAR algorithm takes 9 minutes with a Xeon 2.8GHz processor, which is unacceptable for quick examination before excavation for construction. Therefore, a fast and accurate imaging algorithm is required to be developed also for GPR systems.

ISAR (Inverse Synthetic Aperture Radar) is another imaging algorithm which utilize the motion of targets, especially its rotation, instead of the scan of antennas. In general, ISAR can be applied to a variety of fields, obtaining a high-resolution images. The main concept of ISAR is fundamentally same as that of SAR algorithm. When the antenna is in the far-field zone of the object, the processing reduces to an interpolation plus a 3-D inverse discrete Fourier transform [42]. However, if the antenna is in the near-field, the planar wavefront approximation is not valid and the direct Fourier inversion cannot be used for imaging. Some studies tried and overcame these difficulties [43, 44]. Fortuny [43] proposed a new 3-D near-field ISAR algorithm which utilizes an azimuth convolution between a near-field focusing function and the frequency domain backscattered fields. Broquetas et al. [44] proposed an inverse synthetic aperture radar algorithm which estimates the RCS image instead of the target reflectivity itself, which can work even in near-field. In spite of their successful results, some limitations exist. They assume the motion of the targets is known, which is difficult to achieve our purpose. Moreover, the calculation time cannot
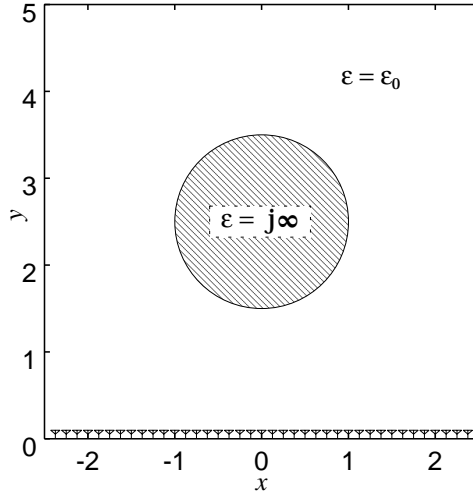
Figure 1.17: Target shape for application of GPR SAR.

be acceptable, which is caused by the fundamental concept of SAR and ISAR algorithm.

1.6.3 Domain Integral Equation

Imaging algorithms based on domain integral equation is one of parametric approaches. In their algorithm, targets and media were modeled as grids of permittivity. The domain integral equation is expressed as

$$\boldsymbol{E}(\boldsymbol{r}) = \boldsymbol{E}_{\text{inc}}(\boldsymbol{r}) + \int k_0^2 C(\boldsymbol{r}') \boldsymbol{E}(\boldsymbol{r}') G(\boldsymbol{r}, \boldsymbol{r}') \mathrm{d}\boldsymbol{r}', \qquad (1.14)$$

where G is the Green's function between two points. $C(\boldsymbol{r}) = \varepsilon(\boldsymbol{r}) - \varepsilon_{\text{b}}$ is the contrast of the target, where ε_{b} is the relative permittivity of the background. $\boldsymbol{E}(\boldsymbol{r})$ and $\boldsymbol{E}_{\text{inc}}(\boldsymbol{r})$ are the total electric field and the incident electric field, respectively. The second term of this equation on the right-hand side indicates the scattered electric field. This equation means that the scattered electric field is caused by the total electric field multiplied by the green function. Franchois et al. [45] solved the domain integral equation with a regularizing term to get a stable solution.It is required to stabilize the solution because the domain integral equation is one of ill-posed inverse problems. Abubakar et al. [46] proposed a 3-dimensional imaging algorithm to solve the nonlinear integral equation in Eq. (1.14). The both of $\boldsymbol{E}(\boldsymbol{r})$ and $C(\boldsymbol{r})$ are unknown in the equation. They defined $W(\boldsymbol{r}) = C(\boldsymbol{r})\boldsymbol{E}(\boldsymbol{r})$, which is seen just like one variable. By using this expression, they divided Eq. (1.14) to two equations. They optimized the evaluation function which includes two factors to satisfy the two equations.

Eq. (1.14) is a nonlinear integral equation because the total electric field $\boldsymbol{E}(\boldsymbol{r})$ cannot be expressed by a linear function of $C(\boldsymbol{r})$. It is generally difficult to solve Eq. (1.14)
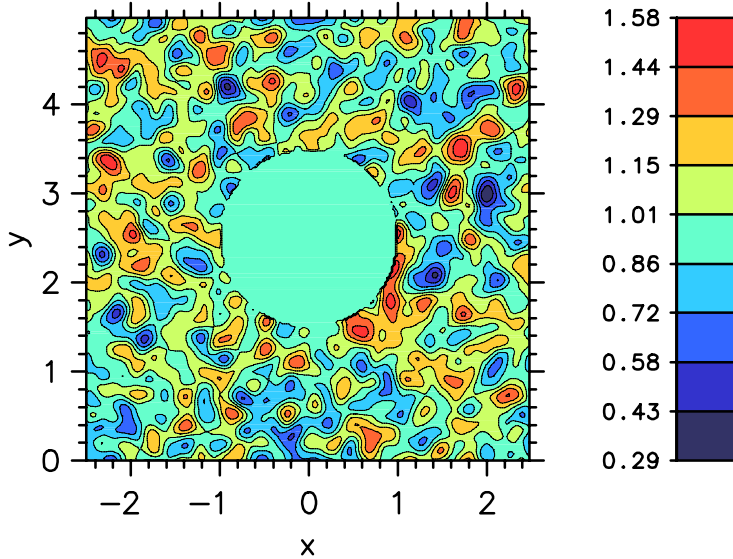
Figure 1.18: Permittivity ε_r of random media.

because of its nonlinearity. To simplify the nonlinear problem, the first-order Born approximation has been widely used which is valid for weak scatterers. The first-order Born approximation is also simply called Born approximation, which is equivalent to the first-order Rytov approximation [47]. Born approximation is formulated as

$$
\boldsymbol{E}(\boldsymbol{r}) = \boldsymbol{E}_\mathrm{inc}(\boldsymbol{r}) + \int k_0^2 C(\boldsymbol{r}') \boldsymbol{E}_\mathrm{inc}(\boldsymbol{r}') G(\boldsymbol{r}, \boldsymbol{r}') \mathrm{d}\boldsymbol{r}', \tag{1.15}
$$

which is a linear integral equation. It is obvious that the $\boldsymbol{E}$ inside the integral in Eq. (1.14) is simply replaced by $\boldsymbol{E}_\mathrm{inc}$ in Eq. (1.15). This is the simplest approximation to solve the domain integral equation, which can be applied only if scattering is weak enough not to disturb the incident electromagnetic waves. Eq. (1.15) can be solved by diffraction tomography [48, 49, 50] or Tikhonov regularization technique. Diffraction tomography is described in the later section. Tikhonov regularization can be applied to Eq. (1.15) as

$$
\mathrm{minimize}_C \quad \left| \boldsymbol{E}(\boldsymbol{r}) - \boldsymbol{E}_\mathrm{inc}(\boldsymbol{r}) - \int k_0^2 C(\boldsymbol{r}') \boldsymbol{E}_\mathrm{inc}(\boldsymbol{r}') G(\boldsymbol{r}, \boldsymbol{r}') \mathrm{d}\boldsymbol{r}' \right|^2 + \alpha \left| L\{C\} \right|, \tag{1.16}
$$

where L is some differential operator, and $\alpha(> 0)$ is the parameter of the compromise between minimizing the main error and the regularization constraint. If α is zero, the optimization problem can be unstable because Eq. (1.15) is an inverse problem even after the linearization. Budko et al. [51] proposed a hybrid imaging of solution of the integral equation with Born approximation with synthetic aperture imaging. They pointed out that the estimation with Born approximation can accurately extract the boundary. On
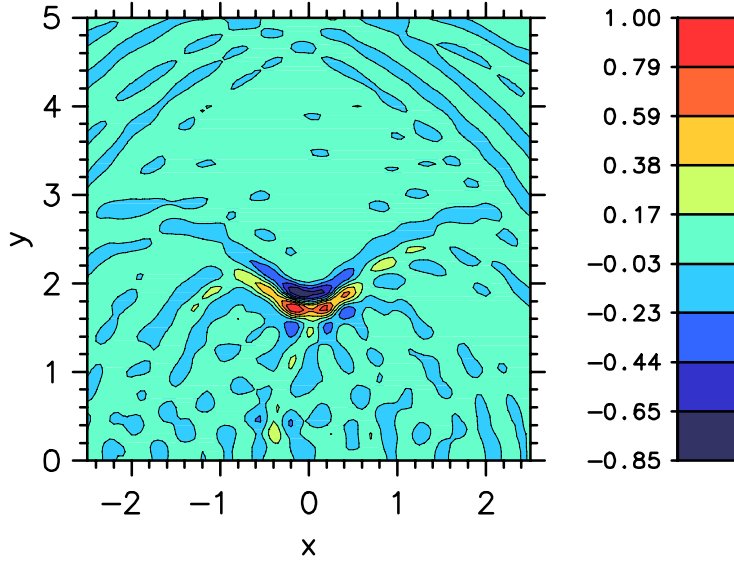
Figure 1.19: Reconstructed image by GPR SAR algorithm.

the other hand, the estimation accuracy of the permittivity is not sufficient. They utilized the synthetic aperture algorithm to obtain the accurate estimation of the permittivity.

A quasi-linear approximation is better than the first-order Born approximation for strong scatterers [52, 53]. The first-order quasi-linear approximation supposes

$$\boldsymbol{E}(\boldsymbol{r}, \boldsymbol{r}_{\mathrm{t}}) = \chi(\boldsymbol{r})\boldsymbol{E}_{\mathrm{inc}}(\boldsymbol{r}, \boldsymbol{r}_{\mathrm{t}}), \tag{1.17}$$

where $\chi(\boldsymbol{r})$ is the ratio of the total electric field to the incident electric field. Here, this approximation assume $\chi(\boldsymbol{r})$ does not depend on the position of the transmitting antenna. Therefore, the nonlinear integral equation is linearized as

$$\boldsymbol{E}(\boldsymbol{r}) = \boldsymbol{E}_{\mathrm{inc}}(\boldsymbol{r}) + \int k_0^2 C_0(\boldsymbol{r}')\boldsymbol{E}_{\mathrm{inc}}(\boldsymbol{r}')G(\boldsymbol{r}, \boldsymbol{r}')\mathrm{d}\boldsymbol{r}', \tag{1.18}$$

where $C_0(\boldsymbol{r})$ is a new object function

$$C_0(\boldsymbol{r}) = \chi(\boldsymbol{r})C(\boldsymbol{r}). \tag{1.19}$$

We see that Eq. (1.18) can be easily solved because Eq. (1.15) and Eq. (1.18) have the same form. We can get $C(\boldsymbol{r})$ using Eq. (1.19) and

$$\chi(\boldsymbol{r}) = 1 + k^2 \int G(\boldsymbol{r}, \boldsymbol{r}')C_0(\boldsymbol{r}')\mathrm{d}\boldsymbol{r}', \tag{1.20}$$

where χ is the sum of the contribution from each point.

22

Cui et al. [54] proposed a high-order quasi-linear approximation as an extension of the first-order quasi linear approximation. They utilize a high-order coefficient $\chi^{(m)}(\boldsymbol{r})$ instead of $\chi(\boldsymbol{r})$. Here, $\chi^{(M)}(\boldsymbol{r})$ is calculated as

$$\chi^{(m+1)}(\boldsymbol{r}) = 1 + A^{(m+1)}(\boldsymbol{r})\chi^{(m)}, \tag{1.21}$$

$$A^{(m+1)}(\boldsymbol{r}) = k^2 \int G(\boldsymbol{r}, \boldsymbol{r}')C_0(\boldsymbol{r}')/\chi^{(m)}(\boldsymbol{r}')\mathrm{d}\boldsymbol{r}', \tag{1.22}$$

where we define $\chi^{(0)}(\boldsymbol{r}) = \chi(\boldsymbol{r})$. The term $C_0(\boldsymbol{r}')/\chi^{(m)}(\boldsymbol{r}')$ is the estimated $C(\boldsymbol{r}')$ in the m-th iteration. They have shown that the second order approximation generated clear image compared to the first-order and zeroth-order approximation, where the zeroth-order quasi-linear approximation is equivalent to the first-order Born approximation.

Chew et al. [55] proposed another extended linearized domain integral equation, which was named distorted Born approximation. This method updates the target image in order to cancel the residual of the evaluation function considering Green's function for two-times scattering neglecting multiple scattering more than two-times. This method is also known to be equivalent to Newton-Kantorovich method, which modifies an image to cancel the residual of the evaluation function by updating the total field instead of Green's function [56, 57]. The difference between the quasi linear approximation and the distorted Born approximation is schematically shown in Fig. 1.20. In this figure, the quasi linear approximation expresses the total field with the direct wave multiplied by the contributions from other targets and the direct wave. Distorted Born approximation expresses the total field with the direct wave and diffracted wave from other targets. The distorted Born approximation has been applied to experimental data by Lobel et al. [58, 59]. They showed that metallic cylinder and metallic strip were clearly reconstructed by the approximation and conjugate-gradient method. It is also effective to apply Tikhonov regularization algorithm to the distorted Born approximation. However, the effect of smoothing of the regularization can degrade some kinds of target shapes. Lobel et al. [60] applied an edge-preserving regularization to an imaging using the distorted Born approximation. They dealt with a reconstruction problem of microwave tomography with receivers around a target. Dourthe et al. [61] applied the same regularization term to GPR (Ground Penetrating Radar) data and confirmed its effectiveness by a numerical simulation.

Born iterative method was proposed by Moghaddam et al. [62], which first calculates the total electric field by assuming the first-order Born approximation. Next, the domain integral equation is solved with the calculated total electric field, and then the total electric field is updated. This procedure is repeated iteratively in the algorithm. Chaturvedi et al. [63] introduced a regularization term for the Born iterative method. They calculated Green's function for each antenna position and each target pixel position and stored them in a table to refer to calculate the scattered field. Yu et al. [64] extended the Born iterative method to deal with a target embedded in a lossy half-space. They analytically derived Green's function for a lossy half-space.

The algorithm based on the domain integral equation assumes that antenna scans
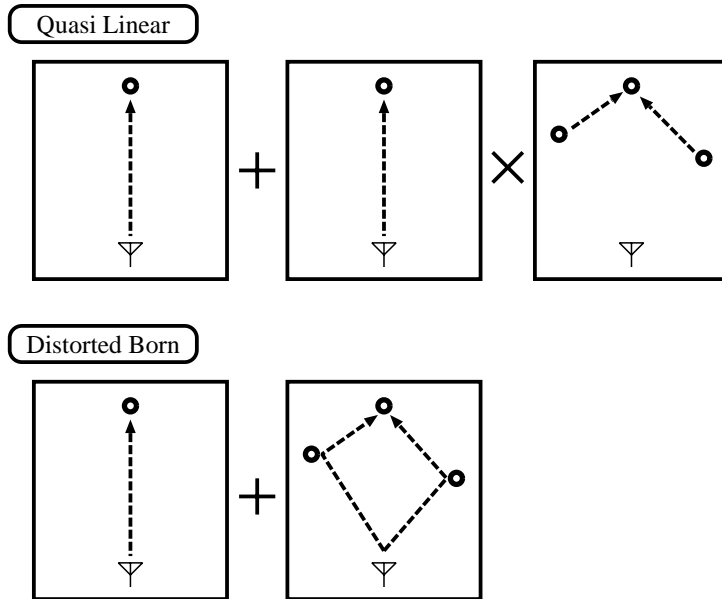
Figure 1.20: Total field expression for quasi linear approximation and distorted Born approximation.

around target, which is not realistic for implementation into robots. Most of the papers utilizing the domain integral equations assume many receivers or many observation points in order to stabilize the solution. This assumption is not valid for our purpose because we assume that the antenna scanning should be done only from one side.

1.6.4 Diffraction Tomography

Diffraction tomography is known as one of algorithms for radar imaging [48, 49, 65, 66]. X-ray CT (Computed Tomography) algorithms mainly for medical use was extended to the diffraction tomography for radio waves to deal with the diffracted waves which are neglectible for X-ray systems. Here, we discuss the diffraction tomography algorithm only for 2-dimensional case for simplicity. The diffraction tomography algorithm is based on the first-order Born approximation as in the previous section. This approximation can linearize the problem, which can be easily dealt with in the frequency domain. The fundamental equation of the diffraction tomography is expressed as

$$\boldsymbol{E}(\boldsymbol{r}_{\mathrm{t}}, \boldsymbol{r}_{\mathrm{r}}) = \boldsymbol{E}_{\mathrm{inc}}(\boldsymbol{r}_{\mathrm{t}}, \boldsymbol{r}_{\mathrm{r}}) - \frac{k^2}{16\varepsilon_0} \int \int C(\boldsymbol{r}) H_0^{(1)}(k|\boldsymbol{r}_{\mathrm{t}} - \boldsymbol{r}|) H_0^{(1)}(k|\boldsymbol{r}_{\mathrm{r}} - \boldsymbol{r}|) \mathrm{d}\boldsymbol{r}, \qquad (1.23)$$

where $\boldsymbol{r}_{\mathrm{t}}$ and $\boldsymbol{r}_{\mathrm{r}}$ are the positions of the transmit antenna and the receive antenna, respectively. $H_0^{(1)}(\cdot)$ is the 0-th order Hankel function of the first kind. Eq. (1.23) holds

24

under the assumption of the first-order Born approximation. This equation shows that the scattered field can be expressed as the convolution of the target image and the Hankel functions. We can estimate $\gamma(\boldsymbol{r})$ by deconvolution processing, which can be realized in the frequency domain. The diffraction tomography is performed in 4 steps as follows.

- Interpolating the missing data for FFT (Fast Fourier Transform).

- Applying FFT to the interpolated data.

- Applying the inverse filtering for deconvolution.

- Applying IFFT to get the final image.

The interpolation is sometimes difficult because sampled points are limited by how to scan antennas. Nahamoo et al. [50] proposed an interpolation-free algorithm for diffraction tomography, which requires to rotate the target by 90 degrees and to observe the echo two times. They have shown the high-resolution image of their algorithm. The image obtained by the diffraction tomography degrades if the length of scanning is not sufficient, which is quantitatively discussed by Cui et al. [67].

In spite of these efforts, the resolution of diffraction tomography is not sufficient especially for large and conductive scatterers. Moreover, it is required for high-resolution imaging to scan the antenna around the target, which is somewhat similar to observation of forward scattering in X-ray tomography. These conditions restrict the application range of the diffraction tomography techniques.

1.6.5 Model Fitting Method

Model fitting method is one of parametric imaging algorithms which utilize the evaluation function and optimization algorithms [68, 69]. In model fitting method, target shapes are expressed as a group of point targets. The location of the set of point targets are expressed as some parameters. The parameters are updated iteratively to minimize the difference between the observed data and the estimated data. The estimated data is calculated in the algorithm, which is a simple forward problem. The evaluation function to minimize is expressed as

$$F = \sum_{j,l} |\boldsymbol{E}(t_j, \boldsymbol{r}_l) - \boldsymbol{E}_{\mathrm{obs}}(t_j, \boldsymbol{r}_l)|^2, \tag{1.24}$$

where $\boldsymbol{E}(t, \boldsymbol{r})$ and $\boldsymbol{E}_{\mathrm{obs}}(t, \boldsymbol{r})$ is the estimated electric field and the observed data at the position $\boldsymbol{r}$ and time t, respectively. This equation assumes the least-mean-square criteria for estimation. This algorithm is easy to understand because the difficulties in the inverse problem are included only in the evaluation function.

Otto et al. [23] utilized above-described LSF model, which has a large number of parameters to optimize. In order to solve this problem, they linearized the problem and solved for the grid-modeled target shapes by using conjugate gradient method. Harada et

al. [70] applied conjugate gradient method to optimize the evaluation function which is the L_1-norm of the difference between the received signal and the calculated signal based on the assumed targets. Sato et al. [71] utilized the expression with Green's function to get the estimated signal. For example, the Green's functions in 2-dimensional electromagnetic wave are $H_0^{(1)}(kr) = J_0(kr) + jN_0(kr)$ (The 0-th order Hankel function of the first kind) and $H_0^{(2)}(kr) = J_0(kr) - jN_0(kr)$ (The 0-th order Hankel function of the second kind), which are the solutions of the Helmholz equation in polar coordinates. Instead of using Green's function, Sato et al. [72] proposed an extended ray tracing algorithm, which can deal with the effect of diffraction. In their study, simple techniques with Green's function cannot be used because their algorithm was for inhomogeneous media. They adopted the modified Marquardt method as an optimization algorithm, whichs require a good initial guess.

Rekanos et al. [73] used the finite-element method to calculate the forward problem and Polak-Ribiere nonlinear conjugate gradient optimization algorithm. This algorithm is one of extensions of the conjugate gradient algorithm, and has the best performance compared to other algorithms such as Fletcher-Reeves algorithm or Hestenes-Stiefel algorithm. Chiu et al. [74, 75] added a regularization term to the evaluation function to stabilize the solution. By the regularization, high-resolution images were obtained stably. FBTS (Forward-Backward Time-Stepping) Method is another imaging algorithm based on the concept of model fitting method [76]. They assume 4 transmitters and 8 receivers around the target and obtain the received data. First, they calculate the received signal by FDTD method with a rough guess of the target shape. The field radiated from an 'equivalent impressed current' of the difference between the measured fields and the calculated fields, is propagated back into the object region, which is also calculated by FDTD method. They update the target shape and physical constants to minimize the difference between the real signal and the estimated signal considering the back-propagated equivalent current and regularization conditions. The algorithm can estimate the target shape and constants even if it is an anisotropic object.

Chiu et al. [74, 75] also dealt with a similar algorithm based on the Green's function. In order to avoid the local optimum point, they used the genetic algorithm (GA), which enable us to get the global optimum solution. However, they assumed 32 receivers around the target, which is difficult to realize. Moreover, GA takes a long calculation time in general, which is not suitable for realtime implementation. Qing et al. [77, 78] attempted to improve the convergence of GA for electromagnetic inverse scattering. They proposed a hybrid algorithm of GA and Newton-Kantorovitch method for speed-up of the imaging. Qing also proposed imaging algorithm with an evolution strategy (DES) [79] and DES with individuals in groups (GDES) instead of GA [80]. In GDES algorithms, all populations are organized into different groups. Individuals in the same group have the same number of targets because the number of targets is unknown. The proposed model of target shape is expressed by the closed cubic B-splines local shape functions, which is effective for stable imaging. Ferraye et al. [24] proposed an imaging algorithm based on contour deformations

26

with a level set method. In this algorithm, the target boundaries are expressed as the zero level sets of a certain function. This function has a negative value inside the target and a positive value outside the target, which leads to a natural regularization. The estimated boundaries move to the normal direction by the update procedures to minimize a cost function. This technique enables us to estimate the shape of multiple complex-shaped objects.

Discrete model fitting methods work well even in inhomogeneous media and layered media as described above. However, it has been pointed out that the solution depends on the initial value because the non-linearity of the evaluation function is quite high. It can be unstable if the suitable initial value is not given. Moreover, the calculation of forward problem takes long time especially for estimation of 3-dimensional shapes. This is because the number of parameters increases exponentially depending on the dimension of the problem.

1.6.6 Migration Algorithms

Migration for Seismic Prospecting

Migration is a well-known imaging technique especially for seismic prospecting [81]. Migration is the process that repositions reflected energy from its common-midpoint position to its true subsurface location. Migration estimates the image as a set of grids step by step iteratively. Migration algorithm has a high performance for geophysical prospecting. Additionally, migration algorithms are applicable for general media and targets. However, their resolutions are limited to the order of the signal wavelength. Moreover, iterative processing leads to the problem that migration algorithm requires a long calculation time, which is not acceptable for the realtime implementation of our purpose.

Migration for Electromagnetic Wave

The migration algorithm explained in the previous section was intended to be applied to seismic wave which is a scalar wave. On the other hand, electromagnetic wave is a vector wave, for which the traditional migration algorithm cannot be applied directly. However, some studies have applied the seismic migration to electromagnetic wave, which works to some extent. Leuschen et al. [82] developed a migration algorithm for vector wave with an idea of matched-filter, which is unique and interesting. The assumed coordinates is depicted in Fig. 1.21. They reconstruct the image $S(\boldsymbol{r}')$ as

$$S(\boldsymbol{r}') = \sum_{n=1}^{N} \int \sum_{m=1}^{M} H(\boldsymbol{r}_n'', \boldsymbol{r}', \boldsymbol{r}_m; \omega) U_n(\boldsymbol{r}_m; \omega) \mathrm{d}\omega \qquad (1.25)$$

in the frequency domain, where N transmitters and M receivers are assumed, and H represents the matched filter and U_n represents the received data for the n-th transmitter.

Matched filters maximize the output power at $t = 0$ if the complex conjugate of the matched filter is equal to the received signal.

The scattered electric field $\boldsymbol{E}_{\text{sca}}(\boldsymbol{r})$ is expressed as

$$\boldsymbol{E}_{\text{sca}}(\boldsymbol{r}) = -\int \overline{G}(\boldsymbol{r}, \boldsymbol{r}')[k^2(\boldsymbol{r}') - k_{\text{b}}^2(\boldsymbol{r}')]\boldsymbol{E}(\boldsymbol{r}')\mathrm{d}\boldsymbol{r}', \tag{1.26}$$

where $\overline{G}(\boldsymbol{r}, \boldsymbol{r}')$ is the background dyadic Green's function, and k and k_{b} are the ordinary wavenumber and the Born-approximated wavenumber, respectively. If the scatterer is small enough, the next equation approximately holds.

$$\boldsymbol{E}_{\text{sca}}(\boldsymbol{r}) \simeq -\omega^2 \mu_0 \overline{G}(\boldsymbol{r}, \boldsymbol{r}')\boldsymbol{E}_{\text{inc}}(\boldsymbol{r}'), \tag{1.27}$$

where $\boldsymbol{E}_{\text{inc}}$ indicates the incident field. By using this approximation, the matched filter H can be written as

$$H(\boldsymbol{r}, \boldsymbol{r}', \boldsymbol{r}'') = \boldsymbol{u}_{\text{r}}^{\text{H}}\{-\omega^2 \mu_0 \overline{G}(\boldsymbol{r}, \boldsymbol{r}')\mathrm{j}\omega\mu_0 \overline{G}(\boldsymbol{r}', \boldsymbol{r}'')T\boldsymbol{u}_{\text{t}}\}, \tag{1.28}$$

where $\boldsymbol{u}_{\text{r}}$ and $\boldsymbol{u}_{\text{t}}$ are the effective length of the receive antenna and the transmit antenna, respectively, which contains the information of polarization. The final image is expressed as

$$S(\boldsymbol{r}') = \{\mathrm{j}\omega\mu_0 \overline{G}(\boldsymbol{r}', \boldsymbol{r})[-\mathrm{j}\omega R\boldsymbol{u}_{\text{r}}]^*\}\{\mathrm{j}\omega\mu_0 \overline{G}(\boldsymbol{r}', \boldsymbol{r}'')T\boldsymbol{u}_{\text{t}}\}, \tag{1.29}$$

where R and T are the received waveform and transmitted waveform, both of which are known after the observation. Eq. (1.29) is divided into two values on the right-hand side. The first term is the electric field generated by a current source $[-\mathrm{j}\omega R\boldsymbol{u}_{\text{r}}]^*$, which can be interpreted as $\mathrm{d}R(-t)/\mathrm{d}t$ in the time domain. This electric field corresponds to the back projection of the migration algorithm. The second term is simply the incident field $\boldsymbol{E}_{\text{inc}}$ with the Born approximation. Eq. (1.29) can be physically interpreted as the intersection of the backpropageted field with the incident field. FDTD method is used to calculate the electric filed in Eq. (1.29). The performance of this algorithm has been confirmed by numerical simulations and experiments [82]. This algorithm can clearly estimate conducting spheres, which are placed nearby although the calculation time is unacceptable because of the utilization of FDTD method.

Kruk et al. [83] also proposed a new migration algorithm for electromagnetic wave for ground penetrating bistatic radar systems. They formulate the electromagnetic field considering polarization of transmitters and receivers. They compared the obtained image to those of other conventional techniques, SAR and Gatzdag algorithm. Gatzdag algirithm, which is similar to SAR, utilizes the method of stationary phase which assumes that the most dominant component in integration should be the point where the phase rotation has a small change.

Migration algorithms are ones of nonparametric algorithms, which is not based on minimizing cost functions. However, all the grid points require iterative calculation, which leads to enormous calculation time. It is required to develop nonparametric algorithm without iterative procedures in order to achieve a fast imaging.
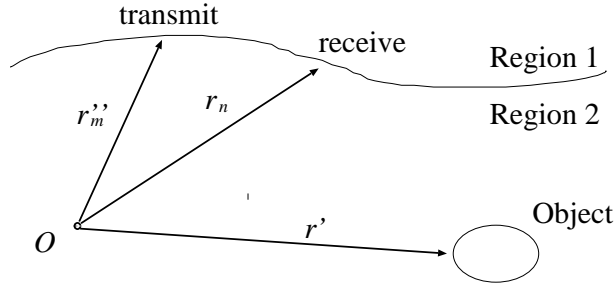
Figure 1.21: The assumed coordinates for the electromagnetic wave migration.

1.7 Scope and Contribution of the Present Work

In the present study, we propose non-parametric imaging algorithms, which accomplishes fast and accurate estimation of target shapes under some constraints. First, we propose an algorithm for estimation of target location and waveforms simultaneously. This algorithm can estimate the location of point targets accurately, which is close to the theoretical limit. Next, we propose a novel non-parametric imaging algorithm for the target in a homogeneous media. This algorithm can estimate target shapes quickly and accurately, which is achieved by utilizing a reversible transform between target shapes and delay time. We also examine the performance of this algorithm in inhomogeneous media. We propose a phase compensation algorithm to enhance the accuracy of the proposed imaging algorithm. Finally, we extend this imaging algorithm to the 3-dimensional case. The performance of the proposed algorithms are confirmed by numerical simulations.

In Chapter 2, we propose an algorithm which estimates target location and scattered waveforms simultaneously. In section 2.2, we introduce the signal image by normalizing distance and time. We explain the concept of Wiener filter and its limitation in section 2.3. Next, Cramer-Rao lower bound, which is the theoretical limit in general estimation problems, is explained in section 2.4. In section 2.5, we introduce HCT (Hyperbolic Coherent Transform) and IHCT (Iterative HCT) which includes the proposed algorithm. In section 2.6, we show the performance of IHCT comparing with those of conventional algorithm and theoretical limit. In section 2.7, we clarify the problem of IHCT for multiple targets, and propose the interference suppression algorithm using neural networks.

In Chapter 3, we propose a non-parametric imaging algorithm based on a reversible transform. In section 3.3, we show the existence of the reversible transform BST (Boundary Scattering Transform), and also show that BST can deal with scattered waves. In section 3.4, we define quasi wavefronts and propose the extraction of quasi wavefronts from the received signals. In section 3.5, we propose a false image reduction algorithm, where the false image is caused by multiple scattering. Additionally, we propose an edge detection algorithm. The whole process is named SEABED (Shape Estimation Algorithm

base on BST and Extraction of Directly scattered waves) algorithm. We also show the application example of the SEABED algorithm with numerical simulations, and clarify the limitation of the SEABED algorithm. In section 3.6, we investigate the performance of the SEABED algorithm against noisy environment.

In Chapter 4, we show an application example of the SEABED algorithm to inhomogeneous media. In section 4.3, we first examine the algorithm for homogeneous media. In section 4.4 and 4.5, we show application examples of the algorithm for random media and layered media, respectively.

In Chapter 5, we propose a phase compensation algorithm for high-resolution pulse radars. In section 5.3, we explain the phase shift effect at an caustic using GO (Geometric Optics) theory, and show an example of the data obtained by FDTD. In section 5.4, we show an application example of the SEABED algorithm, and point out the offset error caused by the phase shift phenomenon. In section 5.5, we propose a phase compensation algorithm based on an analytical process. We put a stress on that the phase shift phenomenon can be naturally expressed with quasi wavefronts. In section 5.6, we show an application example of the proposed phase compensation algorithm. In section 5.7, we investigate the performance of the proposed algorithm in a noisy environment.

In Chapter 6, we propose a 3-dimensional imaging algorithm by extending the SEABED algorithm. In section 6.3, we introduce 3-D BST and 3-D IBST by extending BST and IBST. In section 6.4, we propose a 3-D SEABED by utilizing 3-D IBST, which is natural extension of the SEABED algorithm. In section 6.5, we show the application example of the 3-D SEABED algorithm.

Chapter 2

An Estimation Algorithm of Target Location and Scattered Waveforms

2.1 Introduction

In this chapter, we deal with locationing algorithms for point targets. Radiowave scattering is occurred at edges of targets, which enables us to estimate the target shape without directly estimating the surfaces of the targets. We propose an algorithm for estimation of target location and waveforms simultaneously. A UWB pulse radar is attractive as an environment measurement method for various applications including household robots. However, the accuracy of a UWB pulse radar is not sufficient without a suitable filtering, which is a critical issue. Waveform estimation is very important for pulse radar systems because it improves locationing accuracies. Waveforms of scattered pulses are unknown without estimating target shape because scattered waveforms depend on the shape of the target. The difference between the scattered waveforms and the assumed waveforms degrades the estimation accuracy. Our objective is to develop a non-parametric high-resolution target locationing algorithm by improving the ranging accuracy iteratively. Therefore, it is required to estimate target locations and scattered waveforms simultaneously. Furthermore, the algorithm should be applicable for a general situation including a near field and a far field.

We propose a high-resolution estimation algorithm of target locations and scattered waveforms for UWB pulse radar systems. First, we explain the algorithm and formulate the procedure. We then examine the performance of our algorithm by contrasting it with conventional methods and statistical bounds using numerical simulations. Next, we clarify the problem of applying the proposed algorithm to multiple targets. We propose an algorithm of suppressing the interference based on a neural network algorithm. Finally, we show an application example of the proposed interference suppression algorithm.
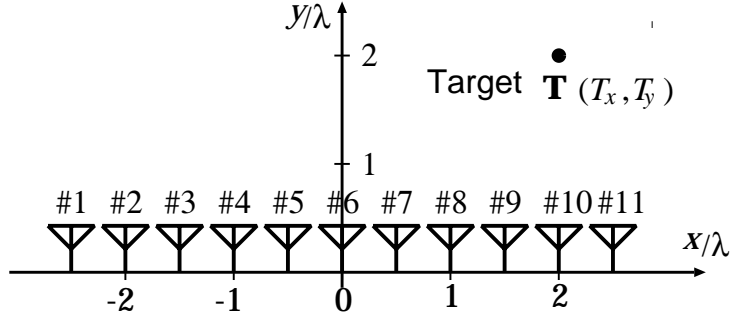
Figure 2.1: The location of the sensor array.

2.2 System Model

We assume an M-element linear sensor array with intervals of half-wavelength at the center frequency of the pulse, and one point target located within its near field. This is because it is more general and difficult to deal with a target in a near field rather than in a far field. We assume that each sensor is omni-directional and the effect of mutual coupling can be neglected. In the situation where these assumptions are not satisfied, we should compensate for the effects as discussed in Sec. 2.6. We transmit the pulse with the center sensor of the array, and receive the scattered signal with all the sensors. The received data with each sensor is input into an A/D converter, and stored into a memory. We define $\boldsymbol{T} = [T_x, T_y]$ as the real target location. Fig. 2.1 shows the location of the sensor array and the coordinates, where λ is the center wavelength of the transmitted signals. The transmitted pulse is a mono-cycle pulse, which is suitable for radar systems because it has no DC power. The used pulse has a relative bandwidth of 96.3%, which satisfies the condition of UWB determined by FCC (Federal Communications Commission) that UWB has a relative bandwidth of more than 20% of the carrier frequency, or an absolute bandwidth larger than 500 MHz. The scattered wave is a spherical wave because the target is within the near field. Therefore, the signal delay draws a hyperbola as a function of the location of the sensors. We assume that the observer has no information of scattered waveforms.

We deal with a 2-dimensional problem in this chapter We also define a signal image $s(x, y)$ as

$$s\left((m - (M + 1)/2)\, d/\lambda,\, ct/\lambda\right) \equiv s'_m(t), \tag{2.1}$$

where $s'_m(t)$ is the received signal with the m-th sensor, c is speed of the light, and $d = \lambda/2$. This definition of a signal image is advantageous because space x and time y are normalized by wavelength. Our algorithm estimates the target location $\boldsymbol{T}$ using the signal image $s(x, y)$. Table 1 shows the simulation parameters.

Table 2.1: Simulation Parameters.

Sensor Array	$M = 11$
Sensor Interval	0.5λ
IHCT Iteration	40times
Observation Duration	24λ
Sampling	83 samples/λ

2.3 Waveform and Filtering

In this section, we explain the importance of estimating waveforms in the proposed algorithm. Wiener filter is often used for estimation of the turn-around-time because it is an effective denoising filter. Wiener filter for signal $G(\omega)$ is expressed as

$$W(\omega) = \frac{G^*(\omega)}{(1 - \eta) + \eta |G(\omega)|^2},$$
(2.2)

where $\eta = 1/(1 + (\text{S/N})^{-1})$. $W(\omega)$ works as an inverse filter for large S/N ($\eta \simeq 1$). On the other hand, it works as a matched filter for small S/N ($\eta \simeq 0$). Here, we define the signal power $S = \max |s(x, y)|^2$. $W(\omega)$ is the optimal filter, in the sense that it minimizes the mean square error between the output signal and the impulse function. However, we can not directly apply Wiener filter to our purpose, because $W(\omega)$ requires the scattered waveform $G(\omega)$. This is the reason why our proposed method is important.

2.4 Theoretical Limit of Locationing Accuracy

In this section we derive the theoretical limit for our problem. The derived theoretical limit is based on Cramer-Rao lower bound (CRLB) [84]. We define $R_{\boldsymbol{T}-\boldsymbol{T}_i}$ as the covariance matrix of the estimation error of the target location, and $\boldsymbol{T}_i = (x_i, y_i)$ as the estimated target location for i-th iteration. The original expression of CRLB is

$$R_{\boldsymbol{T}-\boldsymbol{T}_i} \geq J^{-1}(\boldsymbol{T}),$$
(2.3)

where $J(\boldsymbol{T})$ is Fisher information matrix expressed as

$$J(\boldsymbol{T})_{j,k} = -\text{E}\left\{\iint \frac{\partial^2 \log p(s|\boldsymbol{T})}{\partial T_j \partial T_k} \mathrm{d}x \mathrm{d}y\right\},$$
(2.4)

where $p(s|\boldsymbol{T})$ is the conditional probability density function of $s(x, y)$ and $j, k \in \{x, y\}$. We define E{} as an expectation, which means an ensemble average. We can not directly use Eq. (2.3) because the estimation error is expressed as $e_i = |\boldsymbol{T} - \boldsymbol{T}_i|$. We thus define

$q(\Delta \boldsymbol{T})$ as the probability density function of $\Delta \boldsymbol{T} = \boldsymbol{T} - \boldsymbol{T}_{\mathrm{e}}$, where $\boldsymbol{T}_{\mathrm{e}}$ is the theoretical best estimation. We assume $q(\Delta \boldsymbol{T})$ as

$$q(\Delta \boldsymbol{T}) = \frac{(\det J(\boldsymbol{T}))^{1/2}}{2\pi} \exp\left[-\frac{1}{2}\Delta \boldsymbol{T} J(\boldsymbol{T})\Delta \boldsymbol{T}^{\mathrm{T}}\right]. \tag{2.5}$$

Assuming Eq. (2.5) gives

$$e_i \geq e_{\mathrm{CRLB}} = \int_{-\infty}^{\infty} |\Delta \boldsymbol{T}| q(\Delta \boldsymbol{T}) \mathrm{d}\Delta \boldsymbol{T}. \tag{2.6}$$

e_{CRLB} is the theoretical limit for the estimation of target location. We calculate e_{CRLB} for each S/N in order to contrast with the simulation results. We call e_{CRLB} as CRLB for simplicity in the following sections.

2.5   The Proposed Method for Locationing

In this section, we explain the proposed algorithm. We define Hyperbolic Coherent Transform (HCT) as

$$H(\omega, \boldsymbol{T}_i) \equiv \iint_{-\infty}^{\infty} s(x, y) \frac{\mathrm{e}^{\mathrm{j}\omega[u(x,\boldsymbol{T}_i)-y]}}{\sqrt{u(x,\boldsymbol{T}_i)}} \mathrm{d}x\mathrm{d}y, \tag{2.7}$$

where we define

$$u(x, \boldsymbol{T}_i) \equiv |\boldsymbol{T}_i| + \sqrt{(x - x_i)^2 + y_i^2}. \tag{2.8}$$

HCT works as the Fourier transform for y. $u(x, \boldsymbol{T}_i)$ is a delay time compensation for x. $\sqrt{u(x, \boldsymbol{T}_i)}$ is required in order to improve S/N of HCT, which we explain in the appendix. HCT estimates $F(\omega)$, which is the Fourier transform of the scattered waveform, using coherent integration of the received signals. We can describe the algorithm of target location estimation as

$$\mathrm{maximize}_{\boldsymbol{T}_{i+1}} \left| \int_{-\infty}^{\infty} \frac{H(\omega, \boldsymbol{T}_{i+1}) P_i^*(\omega)}{1 - \eta + \eta |P_i(\omega)|^2} \mathrm{d}\omega \right|^2, \tag{2.9}$$

where $P_i(\omega)$ is the waveform used for constructing Wiener filter. Eq. (2.9) means to maximize the power of the filtered signal at $t = 0$, which is calculated in the frequency domain. This is based on the fact that substituting $t = 0$ for $\exp(\mathrm{j}\omega t)$, the integral kernel of the inverse Fourier transform, the integral kernel shrinks to 1. Eq. (2.9) includes all algorithms which depends on the definition of $P_i(\omega)$. We set the initial waveform $H(\omega, \boldsymbol{T}_0)$ as the Fourier transform of the transmitted waveform. We optimize Eq. (2.9) using Quasi-Newton method, where we set the initial value of $\boldsymbol{T}_i$ to the optimized $\boldsymbol{T}_{i-1}$. We determine the initial value of $\boldsymbol{T}_1$ using a simple grid search.

34
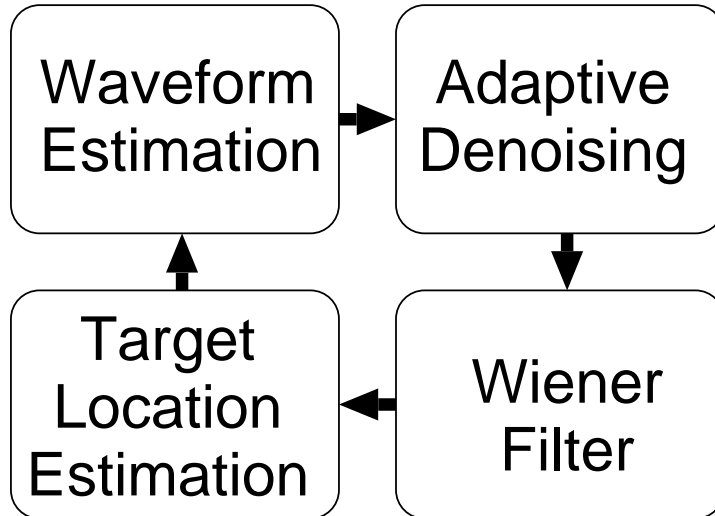
Figure 2.2: The outline of IHCT.

We set $P_i(\omega)$ to

$$P_i(\omega) = (H(\omega, \boldsymbol{T}_i) * \mathrm{sinc}(t_0\omega)) |P_{i-1}(\omega)| \qquad (2.10)$$

for the proposed algorithm. We call the proposed algorithm IHCT (Iterative HCT) because it is based on an iterative improvement of estimation. Eq. (2.10) works as extraction of dominant-frequency waveform. The final form of $P_i(\omega)$ is a narrow-band filter, which is apparently inferior to the ideal matched filter as a single filter for signal detection. However, the major problem of a narrow bandwidth is the ambiguity in finding the peak location, which is solved by the wide-band filter at earlier stages. A better resolution is obtained by accurately determining the phase of the dominant-frequency component. Convolution of $\mathrm{sinc}(t_0\omega)$ is a simple windowing, which prevents the waveform from having an extremely narrow band. We set t_0 to the pulse duration of the transmitted signal. Fig. 2.2 shows the outline of IHCT. We also define IHCTW (IHCT Without waveform estimation) which is a conventional method. We set $P_i(\omega)$ for IHCTW as $P_i(\omega) = H(\omega, \boldsymbol{T}_0)$, which is the transmitted waveform. Moreover, we investigate IHCTK (IHCT with Known scattered waveform) which represents the ideal situation. We set $P_i(\omega)$ for IHCTK as $P_i(\omega) = F(\omega)$, which is the true scattered waveform. IHCTK is not realistic because $F(\omega)$ is unknown in an actual case. Table 2 shows $P_i(\omega)$ for each method.

2.6 Performance Evaluation of IHCT Algorithm

In this section we investigate the performance of the proposed method by contrasting with the conventional method and the theoretical limit. We assume the received waveform is

35

Table 2.2: $P_i(\omega)$ (Denoised HCT) for each method.

IHCT	$(H(\omega, \boldsymbol{T}_i) * \mathrm{sinc}(t_0\omega))\,|P_{i-1}(\omega)|$
IHCTW	$H(\omega, T_0)$
IHCTK	$F(\omega)$

the 1st order differential of the transmitted waveform. Fig. 2.3 illustrates the waveform of $P_i(\omega)$ for $i = 1, 5$ and 10. The bandwidth of the waveform becomes narrower as the iteration proceeds. Fig. 2.4 shows the evaluation function to maximize in Eq. (2.9), where we assume S/N $= \infty$. Here, we use the IHCTK which assumes that the scattered waveform is precisely known. The true target location is $(2.0, 2.0)$, where we see the evaluation function has the peak value. Fig. 2.5 shows the evaluation function without the waveform estimation. This assumption corresponds to IHCTW, which utilize the filter for the transmitted waveform. In this figure, we see that the peak is apart from the true location although two peaks exist around the true location. Fig. 2.6 shows the evaluation function with the proposed algorithm IHCT. There are many peaks in this figure, which is caused by the narrow-band effect of the IHCT algorithm. However, one of the peaks is located at the true location, which enable us to accurately estimate the target location. We also see that a good initial guess is required to optimize this evaluation function because some of peaks can be local optimum points. We can easily get rid of this ambiguity because IHCT algorithm is based on the iterative improvement, which utilizes the solution of the previous step. Furthermore, the initial guess is easily obtained by using UWB pulse radars with a linear search.

Fig. 2.7 shows the locationing accuracy of each algorithm compared to CRLB. Here, we set the target location to $\boldsymbol{T} = (2\lambda, 2\lambda)$. The relationship between the estimation error e_L and the peak S/N is illustrated in the figure. IHCT, IHCTW and IHCTK have poor performance for S/N < 11dB due to invalid initial guess of $\boldsymbol{T}_1$, which is caused by the poor S/N. IHCTK achieves CRLB for S/N ≥ 11dB, which means the optimization in Eq. (2.9) can achieve the theoretical limit only if we know the scattered waveform $F(\omega)$. IHCTW has a floor of estimation error for S/N ≥ 11dB, which is caused by biases due to the fixed reference waveforms. The difference between the transmitted waveform and the scattered waveform causes this error. On the other hand, the performance of IHCT is close to CRLB. The ratio of the estimation accuracy of IHCT to that of CRLB is $1/4$ at most. The estimation error of IHCT has no floor for S/N ≤ 40dB. The estimation accuracy of IHCT is 140 times better than that of IHCTW. Moreover IHCT achieves an accuracy of $10^{-3}\lambda$ for S/N > 34dB, which is sufficiently high for practical use.

Fig. 2.8 shows the estimation error of target location using IHCT for various target locations for S/N $= 40$dB. From the figure, we see that the order of estimation error is $10^{-3}\lambda$ for all target location except for the two areas on both sides of the array. The poor
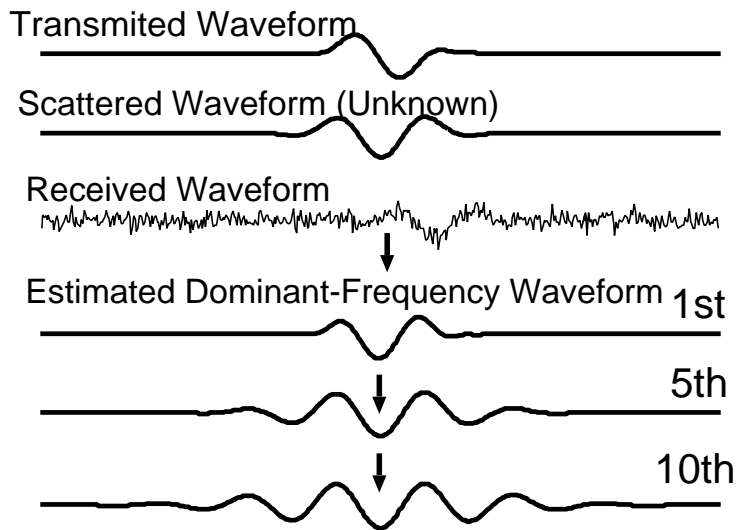
Figure 2.3: Estimated dominant-frequency waveforms.

performance of IHCT in the two areas is caused by the ambiguity of the signal with target locations.

In actual case, the effect of mutual coupling may not be neglected. In such a case, it is possible to compensate for the pattern of mutual coupling because IHCT is based on iterative improvement. The compensation factor can be calculated using the target location estimated at each iteration. We have confirmed the validity of the compensation algorithm of mutual coupling implemented in the IHCT algorithm for a case where the gain varies by 1dB.

We have proposed a locationing algorithm for UWB pulses. If it is applied to narrow-band signals, the resolution degrades because it is difficult to determine the initial value because of the ambiguity due to periodicity of narrow-band signals. We have shown the application example of the algorithm for a target in a near field. However, the proposed algorithm can be applied for a far field as well. As for computational time, the proposed algorithm with iteration of 40 times takes about 50 sec with Xeon 2.8GHz processor.

2.7 Interference Suppression Algorithm for HCT of Multiple Targets

An accurate locationing of targets requires an accurate waveform estimation as described in the previous sections. HCT for a single target can be used as an estimation of the waveform although the noise reduction algorithm is needed. On the other hand, HCT for multiple targets can not be used as a waveform estimation due to the problem of

37
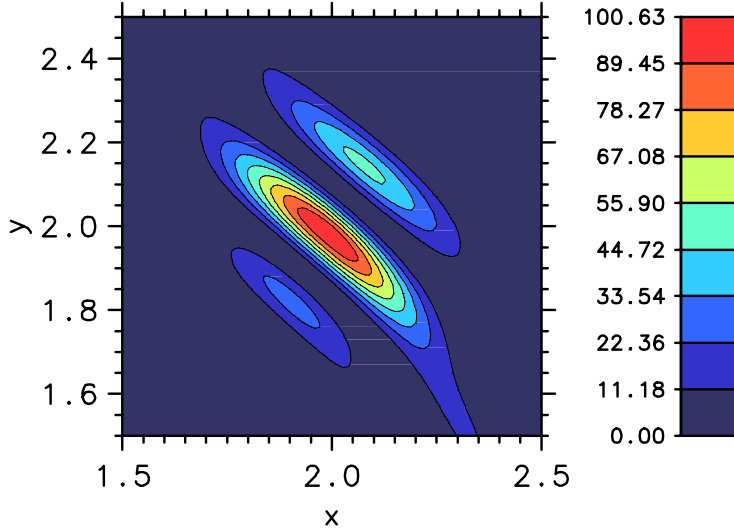
Figure 2.4: Evaluation function with the true filter.

interference. The waveform scattered by a certain target is integrated coherently, and the waveforms scattered by other targets are summed with random delays, which causes cancellation of waves. However, the cancellation of interference waves is not sufficient because the number of antennas is limited, and the signal power is localized. Interference waves can not be neglected especially if the number of targets is large. This residual interference wave is one of the most critical problems when HCT is applied to multiple targets. In this section, we propose an interference suppression algorithm for HCT. We also show the application example of the proposed algorithm using a numerical simulation.

Firstly, we show an example of interference waves. We assume that 5 point targets are located as symbols in Fig. 2.9. Each waveform of the target is the 1st order differential of the transmitted waveform. We assume that we do not have any information about the scattered waveform. We define $h(y, \boldsymbol{T})$ as the IFT (Inverse Fourier Transform) of $H(\omega, \boldsymbol{T})$, and we deal with HCT in the time domain. In Fig. 2.10, the broken line indicates the true scattered waveform, and the solid line indicates $h(y, \boldsymbol{T})$ for $\boldsymbol{T} = (2\lambda, 2\lambda)$. In the figure, we see that undesirable interference waves exist in HCT.

We define $\sigma(y)$ as a standard deviation of waveforms, which is expressed as

$$\sigma(y) = A_\sigma \sqrt{\int_{-\infty}^{\infty} s(x, y)^2 \mathrm{d}x}, \tag{2.11}$$

where we set A_σ to satisfy $\max \sigma(y) = 1$. We also define $e(y)$ as the instantaneous envelope [85] of HCT. $e(y)$ can be expressed as

$$e(y) = A_\mathrm{e} \left| h(y, \boldsymbol{T}) + \frac{\mathrm{j}}{\pi} \int_{-\infty}^{\infty} \frac{h(v, \boldsymbol{T})}{y - v} \mathrm{d}v \right|, \tag{2.12}$$

38
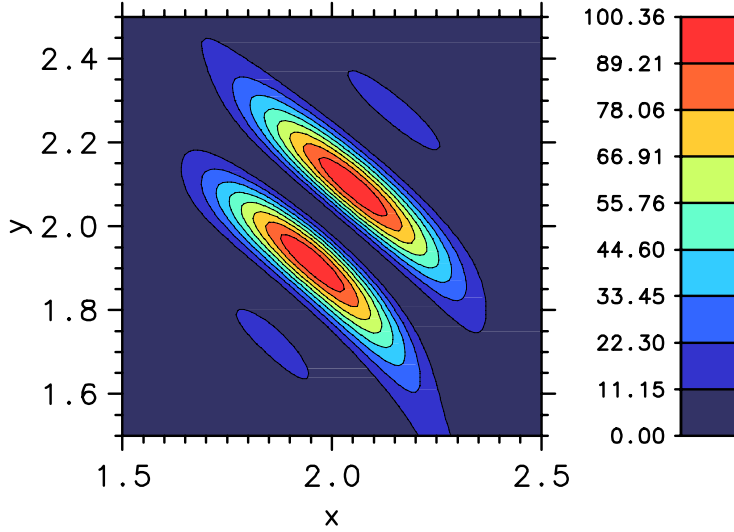
Figure 2.5: Evaluation function with the filter for the transmitted waveform.

where we set A_e to satisfy $\max e(y) = 1$. The integration in Eq. (2.12) means Hilbert Transform of $h(y, \boldsymbol{T})$. Fig. 2.11 shows $\sigma(y)$ and $e(y)$ for the observed data. In the figure, we see that $\sigma(y)$ is small compared to $e(y)$ where the true wave exists. We propose an interference suppression algorithm by utilizing this characteristic. We define an interference-suppressed waveform $\hat{h}(y, \boldsymbol{T})$ as

$$\hat{h}(y, \boldsymbol{T}) = \xi\left(\sigma(y), e(y)\right) h(y, \boldsymbol{T}),\tag{2.13}$$

where $\xi\left(\sigma, e\right)$ is a weight function. We select $\xi\left(\sigma, e\right)$ to satisfy

$$\text{minimize} \quad _\xi \int_{-\infty}^{\infty} \left\{\hat{h}(y, \boldsymbol{T}) - f(y)\right\}^2 \mathrm{d}y,\tag{2.14}$$

where $f(y)$ is the IFT of $F(\omega)$, which is the true scattered waveform. We utilize a neural network in order to optimize $\xi(\sigma, e)$ because $\xi(\sigma, e)$ should be dealt with as a nonlinear function in general. We utilize a 3-layered neural network shown in Fig. 2.12. The ellipse symbols in the figure indicate sigmoid functions. We define $x_{m,n}$ and $y_{m,n}$ as the n-th values in the m-th layer. $y_{m,n}$ are calculated as

$$
\begin{align}
y_{m,n} &= u(x_{m,n}) \tag{2.15}\\
&= 1/\{1 + \exp(-x_{m,n})\},\tag{2.16}
\end{align}
$$

where $u(x)$ is called a sigmoid function. $x_{m,n}$ are calculated as

$$x_{m,n} = \sum_{l=1}^{L} w_{m,l,n} y_{m-1,l} + \beta_{m,n},\tag{2.17}$$
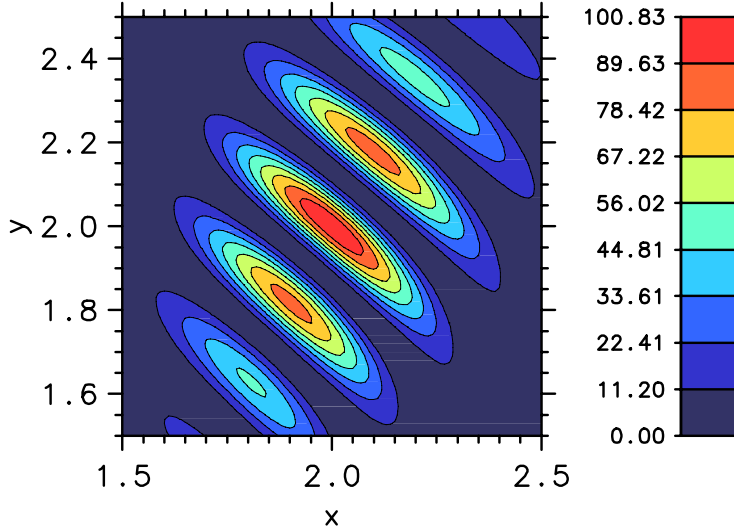
Figure 2.6: Evaluation function with the filter for the estimated waveform of the proposed method (10 iterations).

where, we set $L = 2$. Fig. 2.13 shows the procedure of suppressing interference in the proposed algorithm, assuming the parameters in the neural network is already optimized. In order to obtain the solution of the minimization problem in Eq. (2.14), it is required to know the true scattered waveform $f(y)$. Here, it is impossible to know $f(y)$ prior to the waveform estimation. Therefore, in the proposed algorithm, we utilize the transmitted waveform $h(y, \boldsymbol{T}_0)$ instead of the true scattered waveform $f(y)$. We assume that we know approximate locations of the targets.

The proposed algorithm for an interference suppression is as follows. Firstly, we generate an estimated received signal $s_e(x, y)$ assuming all the signals from targets are equal to $h(y, \boldsymbol{T}_0)$. Then, we calculate $e(y)$ and $\sigma(y)$ from $s_e(x, y)$. In this case, we can solve the minimization problem in Eq. (2.14) because we know the true waveform $h(y, \boldsymbol{T}_0)$. We determine the function $\xi(\sigma, e)$ by solving the optimization problem with $e(y)$, $\sigma(y)$ and $h(y, \boldsymbol{T}_0)$ for $s_e(x, y)$. Fig. 2.14 shows the outline of learning procedure with the neural network in the proposed algorithm. The sum of the error in the figure is minimized for $s_e(x, y)$. We utilize Levengerg-Marquardt-Morrison method for this optimization. Next, we calculate $e(y)$ and $\sigma(y)$ for $s(x, y)$. Then we calculate an interference-suppressed waveform for $s(x, y)$ as in Fig. 2.13. In this way, we obtain waveform $\hat{h}(y, \boldsymbol{T})$ after the interference suppression.

We show an application example of the proposed algorithm. In Fig. 2.15, the broken line and the solid line indicate $h(y, \boldsymbol{T}_0)$ and $h(y, \boldsymbol{T})$ for $s_e(x, y)$, respectively. The interference waveform in the figure is completely different from that of $s(x, y)$ in Fig. 2.10. Fig. 2.16 shows $e(y)$ and $\sigma(y)$ calculated for $s_e(x, y)$. We solve the optimization problem
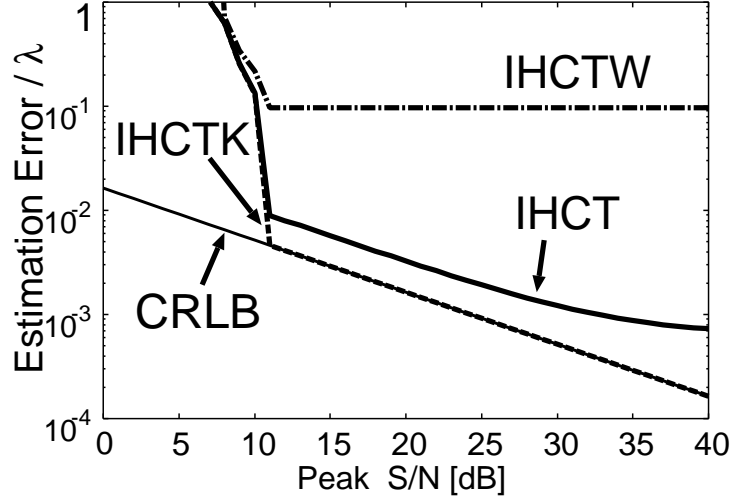
Figure 2.7: Estimation error of the target location.

in Eq. (2.14) and determine the function $\xi(\sigma, e)$. Then, we obtain $\hat{h}^*(y, \boldsymbol{T})$ for $s_e(x, y)$. The solid line and broken line in Fig. 2.17 show $\hat{h}^*(y, \boldsymbol{T})$ and $h(y, \boldsymbol{T}_0)$ respectively. We see that $\xi(\sigma, e)$ can suppress the interference waves to $s_e(x, y)$. Next, we multiply $h(y, \boldsymbol{T})$ by $\xi(\sigma, e)$ in order to suppress the interference of $s(x, y)$. In Fig. 2.18, the solid line and the broken line show the interference-suppressed waveform $\hat{h}(y, \boldsymbol{T})$ and the true waveform $f(y)$ for $s(x, y)$ respectively. In the figure, we see that the proposed algorithm successfully suppresses the interference for $s(x, y)$.

As a result, we clarified that the proposed algorithm has a sufficient performance in suppressing interference waves. Accurate estimations can be accomplished not only for $s_e(x, y)$ but also for $s(x, y)$. Although the function $\xi(\sigma, e)$ is optimized for $s_e(x, y)$, it works well for $s(x, y)$. The learning procedure of the neural network in the proposed algorithm can be accomplished without the true waveforms, because $\xi(\sigma, e)$ depends only on the amplitude distributions of $e(y)$ and $\sigma(y)$ and the true waveform. It should be noted that the proposed algorithm selects strong signals regardless of whether they are from desired or undesired targets. We thus assume that the interference waves have comparatively small power because the signals with large power are chosen firstly.

2.8   Conclusion

UWB pulse radar systems are promising candidates for environment measurement. Firstly, we proposed a high-resolution locationing algorithm for point targets without information of scattered waveforms. The proposed method simultaneously estimates target locations and scattered waveforms for UWB pulse radar systems. The proposed method estimates
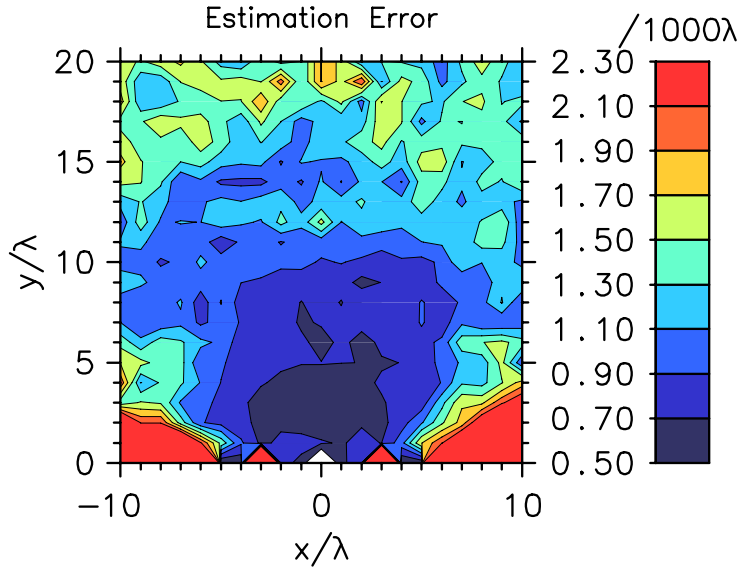
Figure 2.8: Estimation error for various target locations.

dominant-frequency waveforms of scattered waveform iteratively. We also examined the performance of our method by contrasting them with conventional methods and statistical bounds. We evaluated the performance in terms of the estimation accuracy of target locations utilizing numerical simulations. We showed that the performance of the proposed method is close to the theoretical limit. We clarified that the estimation accuracy of the proposed method is 140 times better than that of the conventional method. We also made it clear that the proposed method achieves an accuracy of $10^{-3}\lambda$ for S/N > 34dB.

Next, we proposed an interference suppression algorithm for HCT. Interference waves in HCT can not be neglected especially if the number of targets is large. This residual interference wave is one of the most critical problems when HCT is applied to multiple targets. The proposed algorithm optimizes a weight function, whose variables are the instantaneous envelope of HCT and the standard deviation of waveforms. The proposed algorithm optimizes the weight function by utilizing the transmitted waveform instead of the scattered waveform. We showed an application example of the proposed algorithm, and clarified that the proposed algorithm has a sufficient performance in suppressing interference waves. Further studies are needed in order to apply the interference suppression algorithm to IHCT, which leads to a high-resolution locationing algorithm for multiple targets.

In this chapter, we have investigated the performance of the proposed algorithm only with numerical simulations. An experimental confirmation of the performance of the algorithm will be an important future task.
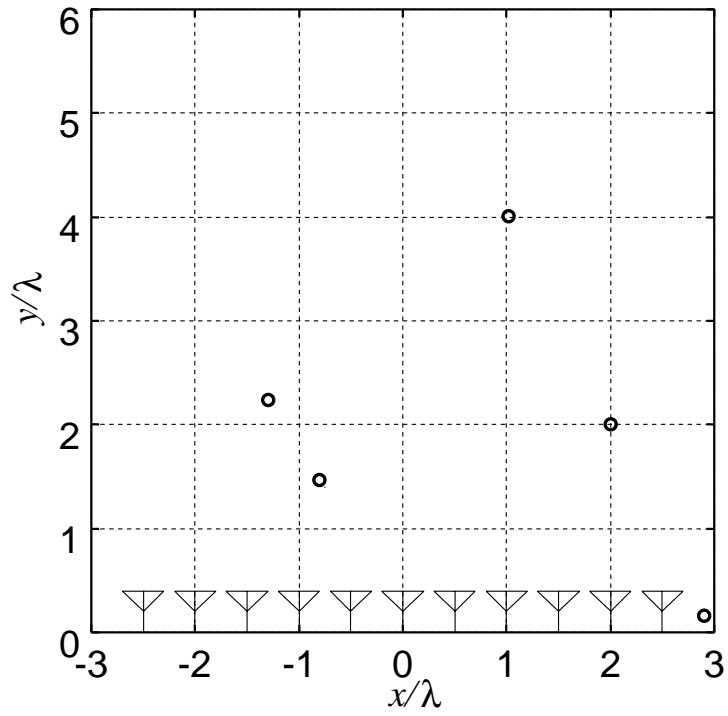
Figure 2.9: Multiple targets location and antennas.
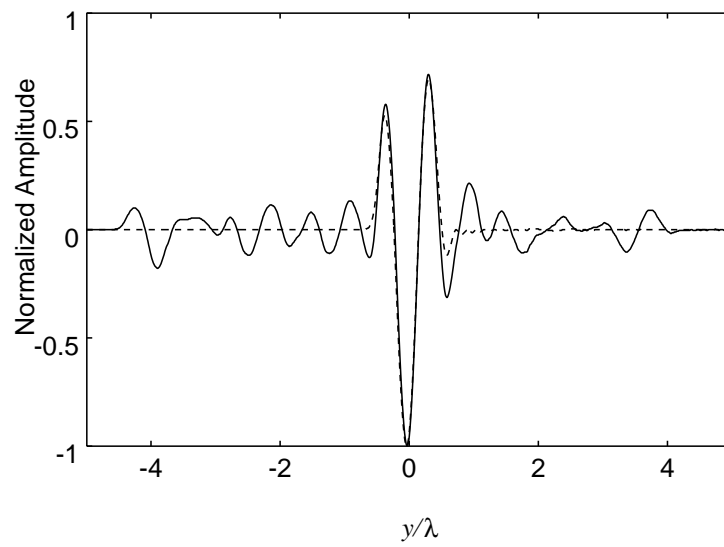
Figure 2.10: HCT for multiple targets and true waveform for $s(x, y)$.
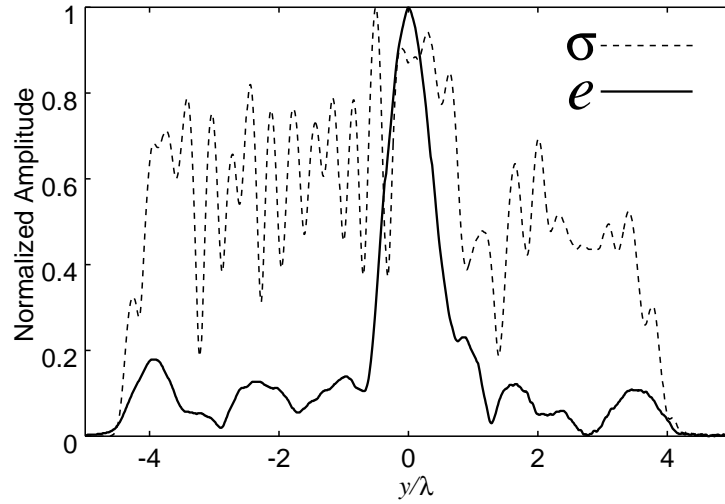
Figure 2.11: $\sigma(y)$ and $e(y)$ for $s(x, y)$.
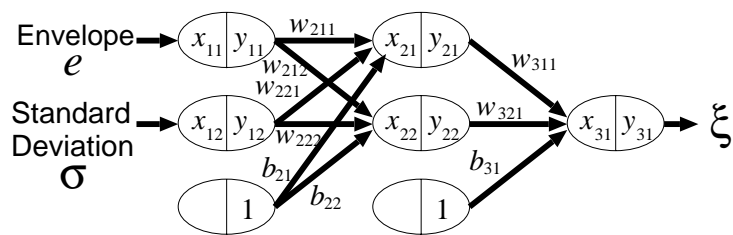
Figure 2.12: Neural network model utilized in the proposed algorithm.
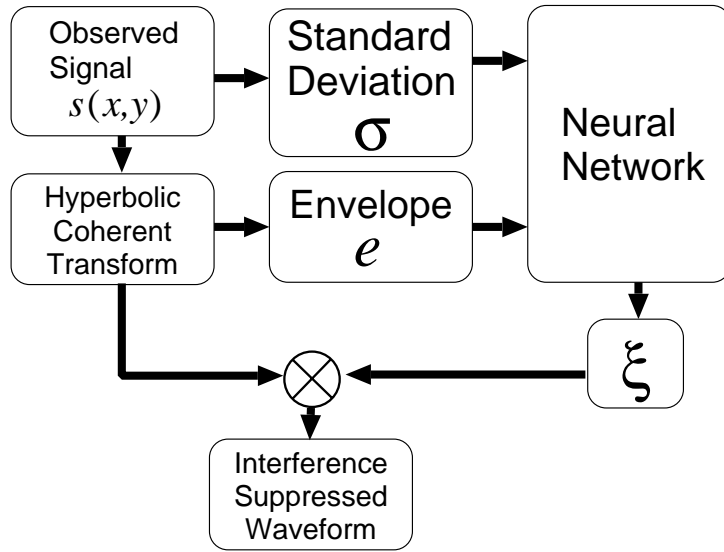
Figure 2.13: The outline of interference suppression in the proposed algorithm.
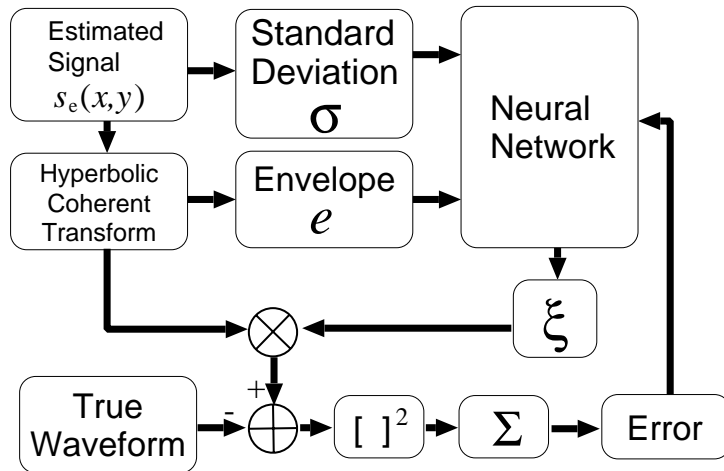
Figure 2.14: The outline of neural network learning procedure in the proposed algorithm.
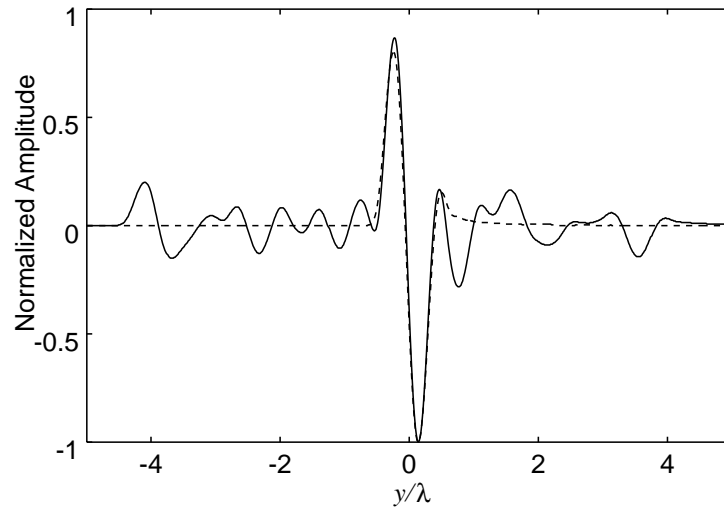
Figure 2.15: HCT for multiple targets and true waveform for $s_{\mathrm{e}}(x, y)$.
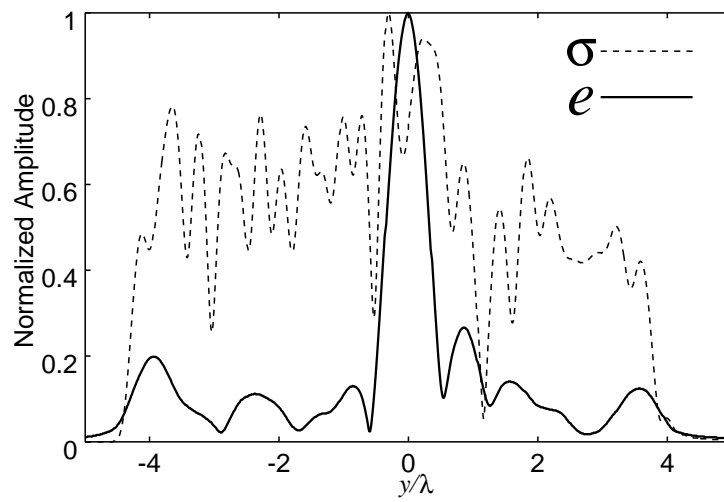
Figure 2.16: Instantaneous envelope of HCT and standard deviation using $s_{\mathrm{e}}(x, y)$.
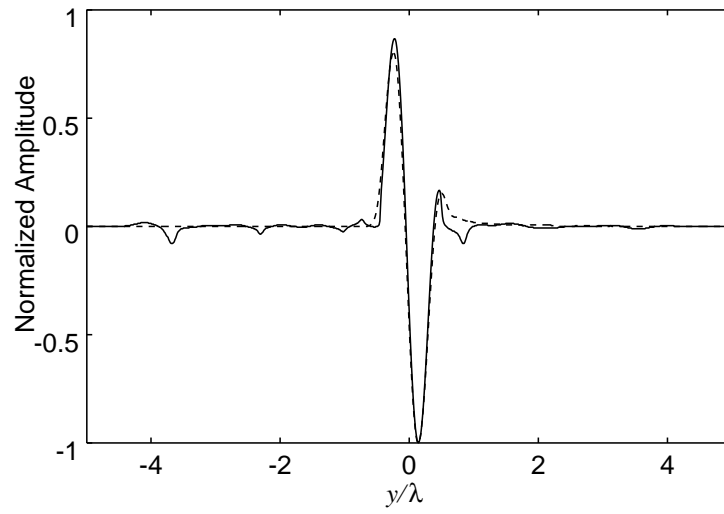
Figure 2.17: Interference suppressed waveform and true waveform for $s_{\mathrm{e}}(x, y)$.
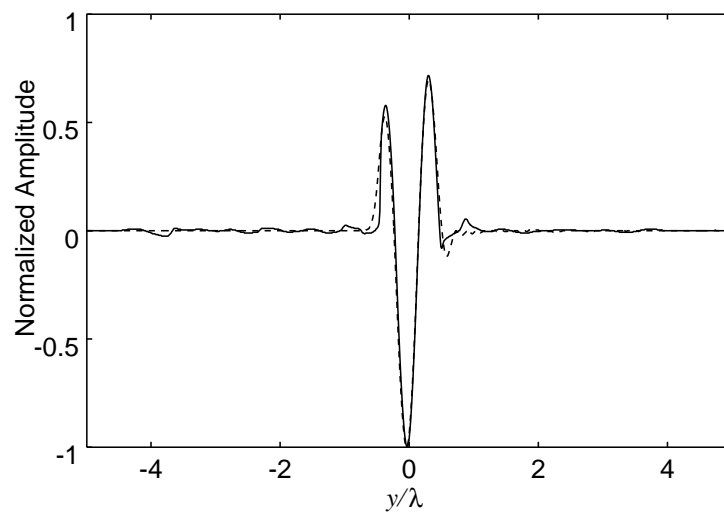
Figure 2.18: Interference suppressed waveform and true waveform for $s(x, y)$.

47

Chapter 3

2-Dimensional Shape Estimation Algorithm Based on Boundary Scattering Transform

3.1 Introduction

In the previous chapter, we proposed locationing algorithms for point targets, which can be applied to edges of targets. In this chapter, we deal with an algorithm to estimate the target surface itself. The reflection wave comes from the points of stationary phase on the target surfaces. We propose a fast imaging algorithm for pulse radar sysesms based on this characteristic. We show the existence of a reversible transform between delay time and target shape. We call the transform IBST (Inverse Boundary Scattering Transform). We propose a non-parametric high-resolution shape estimation algorithm based on IBST. The proposed algorithm using IBST has an advantage that it can uniquely and directly estimate target boundary shapes as lines, although IBST requires targets surrounded by smooth boundaries , uniform media and directly scattered waves.

Firstly, we prove the existence of a reversible transform between delay time and target shape in this chapter. Next, we clarify problems in applying IBST to real data. We propose a selection algorithm and a false image reduction algorithm to solve the problems. Moreover, we propose an edge detection algorithm using IBST. Finally, we show application examples of IBST using a numerical experiment, and investigate the performance of the proposed algorithm.

3.2 System Model

We assume a mono-static radar system in this chapter. An omni-directional antenna is scanned along a straight line. UWB pulses are transmitted at a fixed interval and received

by the antenna. The received data is input into A/D converter, and stored into a memory. We estimate target shapes using the data.

We deal with a 2-dimensional problem, and TE-mode wave. Targets and the antenna are located on a plane. We define r-space as the real space, where targets and the antenna are located. If a set is expressed in r-space, we call it the expression in r-domain. We express r-space with the parameter (x, y). Both x and y are normalized by λ, which is the center wavelength of the transmitted pulse in a vacuum. We assume $y > 0$ for simplicity. The antenna is scanned along x-axis in r-space. We define $s'(X, Y)$ as the received electric field at the antenna location $(x, y) = (X, 0)$, where we define Y with time t and speed of the light c as $Y = ct/(2\lambda)$. We set $t = 0$ to the time which maximizes the instantaneous envelope of electric field at the location of the antenna. We apply a matched filter of transmitted waveform to $s'(X, Y)$. We define $s(X, Y)$ as the output of the filter. We define d-space as the space expressed by (X, Y). If a set is expressed in d-space, we call it an expression in d-domain. We normalize X and Y by λ and the center period of transmitted waveform, respectively.

We propose a non-parametric high-resolution estimation algorithm of target shape using the data $s(X, Y)$. Firstly, we extract quasi wavefronts, which is delay times of direct scattered waves. Next, we obtain approximate estimation of target shapes by applying IBST to the extracted quasi wavefronts. We then apply a selection algorithm and a false image reduction algorithm to the data by using evaluation value of target boundary based on the locations and shapes of targets. Finally, we estimate the target shapes and the edge-point locations. Fig. 3.1 illustrates the outline of the algorithm we propose in this chapter.

3.3 Boundary Scattering Transform and its Inverse Transform

3.3.1 Boundary Scattering Transform

We prove the existence of a reversible transform between quasi wavefronts and target boundary surfaces in this section. Although we deal with a 2-dimensional problem, the algorithm can be easily extended to a 3-dimensional one. Additionally, we assume scanning of the antenna along a straight line, but it can be easily extended to scans along any curves.

We assume that each target has a uniform complex permittivity, and surrounded by a smooth boundary. The target complex permittivity of the target $\varepsilon(x, y)$ satisfies

$$|\nabla \varepsilon(x, y)|^2 = \sum_{q \in H} a_q \delta(y - g_q(x)), \tag{3.1}$$

where δ is Dirac's delta function, and $g_q(x)$ is a differentiable single-valued function. We

define

$$q = \{(x, y) | y = g_q(x), x \in J_q\} \in H, \tag{3.2}$$

where J_q is the domain of $g_q(x)$, a_q is a positive real constant which depends on $q \in H$, and H is the set of all q. We define target boundary surfaces as elements of H. Fig. 3.2 illustrates the coordinates and an example of a target complex permittivity $\varepsilon(x, y)$ in r-space. The assumption of the target model in Eq. (3.1) is general because it includes the case where the target complex permittivity is divided into some areas as in Fig. 3.2.

Next, we define several sets in order to explain Boundary scattering transform. We define P, which is a subset of d-space, as

$$P = \{(X, Y) | \partial s(X, Y) / \partial Y = 0, |s(X, Y)| \geq T_s\}, \tag{3.3}$$

where T_s is a threshold to prevent picking up noise values.

Next, we connect the points close to each other in P. We obtain lines from P in this way. We express each line as p, which we call a quasi wavefront. We define G as the set of all $p \in P$.

Here, we assume that the medium of direct path is vacuum, but the following argument is valid for any uniform media only if the propagation speed of the wave is known. We assume p corresponds to the direct scattered wave of q. By utilizing the relationship between the antenna location and the length of perpendicular line to q from the antenna location, the point (X, Y) on p is expressed as

$$\begin{cases} X &= x + y \mathrm{d}y/\mathrm{d}x \\ Y &= y\sqrt{1 + (\mathrm{d}y/\mathrm{d}x)^2}, \end{cases} \tag{3.4}$$

where (x, y) is a point on q, and we assume $y > 0$ and $Y > 0$. We define the transform in Eq. (3.4) as Boundary Scattering Transform (BST).

Fig. 3.3 shows an example of BST. The upper figure shows the target boundary surface in r-domain, and the lower figure is the corresponding quasi wavefront in d-domain, which is the BST of the upper figure. In general, some quasi wavefronts are generated from one target boundary surface by BST as in the figure.

3.3.2 Inverse Boundary Scattering Transform

If an inverse transform of BST exists, we can estimate target shapes using the transform. In this subsection, we prove the existence of the inverse transform of BST.

IBST is based on a back projection process. When there is a reflection at (X, Y) in d-space, the target is on a circle $C(x, y; X, Y)$ of its center $(X, 0)$ and its radius of Y in r-space. If a reflection forms a curve p, point (X, Y)'s on p produce a group of circles in r-space. The envelope of the group of circles must draw its target shape. This process is

formulated as follows. Firstly, we express the circle for given (X, Y) using a point (x_c, y_c) on it. We define a group of circles $C(x_c, y_c; X, Y)$ as

$$
\begin{aligned}
&C(x_c, y_c; X, Y) \\
&= \left\{ (x_c, y_c) \, | \, y_c > 0, F_C(x_c, y_c; X, Y) = 0 \right\},
\end{aligned}
\tag{3.5}
$$

where $F_C(x_c, y_c; X, Y)$ is expressed as

$$
F_C(x_c, y_c; X, Y) = (x_c - X)^2 + y^2{}_c - Y^2.
\tag{3.6}
$$

Next, we express the envelope of the group of circles $C(x_c, y_c; X, Y)$ using a point (x_e, y_e) on it. We define E_C as the envelope of the group of circles $C(x_c, y_c; X, Y)$. E_C satisfies

$$
\begin{aligned}
&E_C(x_e, y_e; X, Y) \\
&= \left\{ (x_e, y_e) \, | \, y_e > 0, F_C(x_e, y_e; X, Y) = 0, \right. \\
&\qquad\qquad \left. \partial F_C(x_e, y_e; X, Y)/\partial X = 0 \right\}.
\end{aligned}
\tag{3.7}
$$

Here, the partial derivative means the derivative independent only of x_e and y_e, not of Y. Here, we should note that Y is uniquely determined by X with a certain function. The equation of E_C is expressed as

$$
\left\{
\begin{aligned}
x_e &= X - Y \mathrm{d}Y/\mathrm{d}X \\
y_e &= Y\sqrt{1 - (\mathrm{d}Y/\mathrm{d}X)^2}.
\end{aligned}
\right.
\tag{3.8}
$$

We have to check if Eq. (3.8) works as an inverse transform of BST expressed in Eq. (3.4). Substituting Eq. (3.4) to Eq. (3.8), we obtain

$$
y_e^2 - y^2 + (x_e - x)^2 - 2(x_e - x)y\mathrm{d}y/\mathrm{d}x = 0.
\tag{3.9}
$$

Eq. (3.9) holds for any function $g_q(x)$, for any x. Therefore, we conclude that $x = x_e, y = y_e$. This means that Eq. (3.8) satisfies the condition of an inverse transform of BST. As a result, we conclude that the inverse transform of BST is given by

$$
\left\{
\begin{aligned}
x &= X - Y \mathrm{d}Y/\mathrm{d}X \\
y &= Y\sqrt{1 - (\mathrm{d}Y/\mathrm{d}X)^2}.
\end{aligned}
\right.
\tag{3.10}
$$

We define the transform in Eq. (3.10) as Inverse Boundary Scattering Transform (IBST). The existence of the inverse transform is very meaningful because it can be used for a direct and unique estimation of target boundary shapes. The estimated target boundaries are expressed as not an image but lines. This is the advantage and the characteristic of our algorithm.

51

The condition of existence of IBST is differentiability of the quasi wavefront and

$$|\mathrm{d}Y/\mathrm{d}X| \leq 1. \tag{3.11}$$

This inequality in Eq. (3.11) is required because if it is not satisfied, the value of y obtained using IBST in Eq. (3.10) is not a real number, which is not rational. In a situation of Fig. 3.2, a target perpendicular to x-axis produces a straight line of its inclination of 45 degrees in d-space. We assume that we can receive the directly scattered waves from the target boundary. However, if this condition is not satisfied, the estimation accuracies are degraded. Plural quasi wavefronts are generated from one target boundary surface by BST in general. However, if we find out all quasi wavefronts from the received data, it is possible to reconstruct the target boundary surfaces using IBST. Therefore, the plural quasi wavefronts generation has no problem in our algorithm.

3.3.3 Edge Refraction Waves and Boundary Scattering Transform

We have shown that the relationship between quasi wavefronts and target boundary surfaces is expressed as BST and IBST if the complex permittivity satisfies the condition in Eq. (3.1). If IBST is applicable not only for reflection but also for refraction, we see that IBST has a great deal of application range. In this subsection, we investigate the relationship between edge refraction waves and IBST.

If an edge point of a target is located at (α, β), the delay time of received signal is expressed as a hyperbola as

$$Y = \sqrt{(X - \alpha)^2 + \beta^2}. \tag{3.12}$$

The IBST of Eq. (3.12) is $[x, y]^{\mathrm{T}} = [\alpha, \beta]^{\mathrm{T}}$, where T means transpose. BST of the edge point is not defined because the differentiability condition is not satisfied in this case. However, it is possible to estimate the edge point location using IBST. Substituting the hyperbola in Eq. (3.12) to BST in Eq. (3.4), we obtain the differential equation expressed as

$$\mathrm{d}y/\mathrm{d}x = (y^2 - x^2 - \beta^2)/2xy, \tag{3.13}$$

where we assume $\alpha = 0$ because α works only as a parallel translation of x. If the solution of Eq. (3.13) draws a certain curve, it brings a trouble in applying IBST, because it means that a target boundary surface exists which has the same quasi wavefront of an edge point. Therefore, it is important to investigate a differential equation of Eq. (3.13), which is one of Bernoulli-Riccati differential equations. Considering $y \geq 0$, the general solution of the equation is expressed as

$$y = \sqrt{\beta^2 - x^2 - Cx}, \tag{3.14}$$

where C is an integral constant. The BST of Eq. (3.14) is expressed as

$$[X, Y]^{\mathrm{T}} = \left[-C/2, \sqrt{C^2/4 + \beta^2} \right]^{\mathrm{T}}. \tag{3.15}$$

The solution of the differential equation expresses a circle with a radius $\sqrt{\beta^2 + C^2/4}$, and center $[-C/2, 0]^{\mathrm{T}}$. The BST of Eq. (3.15) shrinks to a point on the hyperbola in Eq. (3.12). The differential of a point is not defined, therefore it has no problem in applying IBST to data.

Consequently, IBST is applicable to both of reflection waves and refraction waves. IBST precisely estimates target boundary surfaces and edge point locations if an antenna can receive the directly scattered waves from the target boundary. We propose the algorithm using IBST in this chapter, and show an example of application of IBST in the following sections.

3.4 Quasi Wavefront Extraction from Received Data

3.4.1 Extraction of Quasi Wavefront

In this section, we describe the method of extraction of quasi wavefronts. We have already defined the set P. The procedure of extraction of P is easy because all we should do is to check the derivative of given data. Next, we go on to the procedure of extracting $p \in G$ from P. In an actual procedure, we sequentially connect the points in P which satisfy a required condition. $p \subset P$ are connected closed sets. The i-th set p_i is determined as follows. The first element of p_i is an arbitrary element of P which is not included in $p_1, p_2, \cdots, p_{i-1}$. The domain I_i for p_i is set to X of the first element. The second element of p_i is chosen from P which satisfies $|\mathrm{d}Y/\mathrm{d}X| \leq 1$ in Eq. (3.11). Here, Y should have only one value for the same X. Then, domain I_i is updated according to the newly chosen element. In this way, we expand the set p_i until there is no other element which can be included into p_i. Finally, the extracted p_i has a characteristic as

$$
\begin{aligned}
p_i \;=\; &\{(X, Y) | Y = f_i(X), \\
&\quad |\mathrm{d}f_i(X)/\mathrm{d}X| \leq 1, X \in I_i\},
\end{aligned}
\tag{3.16}
$$

where $f_i(X)$ is a single-valued function whose domain is I_i. Eq. (3.16) means that a unique Y has to exist satisfying $(X, Y) \in p_i$ for any $X \in I_i$. The algorithm described in the next subsection removes the undesirable links generated in this procedure.

3.4.2 Evaluation of Quasi Wavefront

As mentioned in the previous section, $p \in G$ denote quasi wavefronts which correspond to direct scattered waves from targets. Simply extracted quasi wavefronts include false quasi wavefronts generated by noises, ringing of waveforms, and multiple scattering. It is important to remove these false quasi wavefronts.

We define an evaluation value w_i for $p_i \in G$ as

$$
w_i = \left| \int_{X \in I_i} s(X, f_i(X)) \mathrm{d}X \right|^2 .
\tag{3.17}
$$

w_i becomes large when both of the amplitude of the signal along the quasi wavefront, and the width of the domain of $f_i(X)$ are large. If both of positive and negative points exist in a quasi wavefront, the evaluation value becomes small. This characteristic is valid because quasi wavefront should be constructed by connecting points with same phases. Fig. 3.4 illustrates the reason why we adopt the integration of the signal amplitude as an evaluation value. If we adopt the integration of the signal power as an evaluation value, undesirable quasi wavefronts are extracted as shown in the right panel of Fig. 3.4.

We can remove false quasi wavefronts caused by noises and ringing of waveforms by utilizing the evaluation value w_i for most cases. However, the evaluation value for a false quasi wavefront becomes large when the false quasi wavefront is close to real quasi wavefronts. In this case, the evaluation value in Eq. (3.17) is not sufficient. In order to solve this problem, we propose the following algorithm which allows us to subdivide the regions. The procedure described in Sec. 2.4.1 does not exclude situations that $p_1 \cap p_2 \neq \phi$(nullset) for $p_1, p_2 \in G$, $p_1 \neq p_2$ as shown in Fig. 3.5. In such a case we subdivide the quasi wavefront so that the two sets contain only one element in common. In the figure, $p_1 = \{a, b, e, f, g\}$ and $p_2 = \{a, b, c, d\}$. In this case, we divide the quasi wavefront as $p_1 \rightarrow p'_1$ if $w_{p_1} \leq w_{p_2}$. Note that p'_1 has lower evaluation value than p_1. If $w_{p_1} \geq w_{p_2}$ holds, we divide p_2 as $p_2 \rightarrow p'_2$. Here, $p'_1 \cup p_2 = p_1 \cup p'_2 = p_1 \cup p_2$, $p'_1 \cap p_2 = p_1 \cap p'_2$ and $|p'_1 \cap p_2| = |p_1 \cap p'_2| = 1$ are satisfied, where $|p|$ represents the number of elements of the set p. In Fig. 3.5, $p'_1 \cap p_2 = p_1 \cap p'_2 = \{b\}$. After this subdivision, we can remove regions with small w_i by recalculating w_i.

3.4.3 An Example of Application of Quasi Wavefronts Extraction

We show an example of application of the extraction algorithm of quasi wavefront, which we explained in the previous subsection. Fig. 3.6 shows an example of target boundary surface. The upper domain in the figure is filled with perfect electric conductor, and the lower domain is filled with air. The symbols located at the bottom of the figure show the locations of the antenna, where we receive signals. Fig. 3.7 shows the BST of the target in Fig. 3.6. We calculate refraction waves from the edge points in another way, because we can not derive it using BST. In the figure, plural quasi wavefronts are generated. Extraction of these true quasi wavefronts enable us to estimate the target shape using IBST.

Fig. 3.8 shows the received data from the target shown in Fig. 3.6, which we obtain by utilizing FDTD (Finite Difference Time Domain) method. We receive the signal at the 40 locations illustrated in Fig. 3.6, whose intervals are 0.125λ. Here, we assume a noiseless case. There is a false quasi wavefront caused by multiple scattering in the figure. Except for it, other quasi wavefronts are approximately same in Fig. 3.7. Fig. 3.9 shows a set P extracted from the signal in Fig. 3.8. We select the points in d-domain where the differential of the waveform is equal to zero. Here, we remove points with small power

by a ranking algorithm. Numerous undesired points exist in P due to the ringing of the waveform. Fig. 3.10 shows $\cup_{p \in G} p$, which is the set of all quasi wavefronts p extracted from the received signal. As mentioned above, quasi wavefronts $p \in P$ satisfies $|dY/dX| \leq 1$, which is the condition of existence of IBST.

Our algorithm extract quasi wavefronts at large, and they include a part of edge refraction wave shown in Fig. 3.7, because we utilize a ranking algorithm in extraction of P. On the other hand, undesired quasi wavefronts and multiple scattering waves also appear. We apply the quasi wavefront division algorithm to $p \in G$ based on the evaluation values as explained in the previous subsection, and then we recalculate the evaluation values for updated quasi wavefronts. Next, we select the quasi wavefront whose evaluation value is greater than $-n$dB of the maximum evaluation value. Fig. 3.11 shows the updated and selected quasi wavefronts, where an empirically chosen value of $n = 10$ is used. The proposed algorithm above extracts 4 quasi wavefronts from the received signal. These are approximately equal to the real quasi wavefronts in Fig. 3.7 except for the false quasi wavefront caused by the multiple scattering. Although the proposed algorithm extract only a part of the edge refraction quasi wavefronts, it is sufficient for locationing of edge points.

3.5   False Image Reduction for Multiple Scattering and Edge Point Locationing

3.5.1   An Example of Application of IBST

Here, we show an example of the application of IBST. We apply IBST to the quasi wavefronts in Fig. 3.11. We utilize a smoothing algorithm with B-spline function in order to obtain the differential of a quasi wavefront. Fig. 3.12 shows a result of IBST application. The solid line and the broken line in the figure are the real target boundary surface and the estimated target boundary surface respectively. The target shape is estimated by IBST in the figure. However, a false image appears above the real target. This is caused by the multiple scattering, and it is difficult to remove the false image in the algorithm of quasi wavefront extraction as described above.

3.5.2   False Image Reduction Algorithm for Multiple Scattering

In this subsection, we propose an algorithm which removes the false image caused by multiple scattering. We see that the false image is behind the true target boundary from the antenna position. We can remove the false image by using this nature. Firstly, we assume a segment between a point of an estimated target boundary and the antenna position where we receive the directly scattered waveform from the point. If other estimated target boundaries exist near the segment, the reliability of the estimated target boundary

is reduced because the received power from the point is reduced by the obstacle target between the target and the antenna. Therefore, we reduce the evaluation value for the target boundary in that case. We also utilize the evaluation value of the obstacle targets for the penalty value. We formulate this process as follows.

We define a domain F_p using X satisfying $(X, Y) \in p$ and x, y satisfying $(x, y) \in \mathcal{B}^{-1}[p]$ as

$$
\begin{aligned}
F_p \;=\; & \left\{ (x_0, y_0) \,\middle|\, \sqrt{(x - x_0)^2 + (y - y_0)^2} \right. \\
& \left. + \sqrt{(X - x_0)^2 + y_0^2} - \sqrt{(x - X)^2 + y^2} < 1/2 \right\},
\end{aligned}
\tag{3.18}
$$

which is known as the 1st Fresnel zone. Here, we define $\mathcal{B}$ as the BST operator. We propose an algorithm which update the evaluation value w_i to the new evaluation value W_i as

$$
W_i = w_i - \sum_{p_j \neq p_i \in G} w_{p_j} R_{p_j, p_i}
\tag{3.19}
$$

where $R_{r,p}$ means the ratio of the length of a quasi wavefront r whose BST is within F_p to the total length of r. The 2nd term of the right hand side of Eq. (3.19) means the penalty value for the evaluation value. The evaluation value W_i becomes small when other targets are in its 1st Fresnel zone. We utilize not a segment but 1st Fresnel zone for the algorithm because any other objects in the 1st Fresnel zone may significantly reduce the power of the received signal. Fig. 3.13 shows the estimated target boundary surfaces using the new evaluation value W_i. The solid line and the broken lines are the real target boundary surface and the estimated target boundary surfaces, respectively. Here, we select the target boundary surface whose evaluation value is larger than $-n$dB of the maximum evaluation value. Here we use an empirically chosen value of $n = 10$. The proposed algorithm successfully removes the false image of the boundary surface. The degradation of the estimation accuracy on the concave surface compared to the straight surface is caused by the difference between the observed waveform and the reference waveform for the matched filter. The target shape estimation accuracy is approximately 0.15 λ at most.

3.5.3 Edge Point Locationing Algorithm

We obtain the target boundary surface sampled at non-equi-intervals if we apply IBST to the quasi wavefronts sampled at equi-interval of X in d-domain. Fig. 3.14 shows an example of the target boundary surface sampled at non-equi-interval. The solid line is the real target boundary surface, and the cross symbols are the target boundary surfaces. It is possible to detect edge points using IBST because IBST concentrates a quasi wavefront from an edge point to a single point. We propose an edge point locationing algorithm as follows.

Firstly, we count the number of the points within the circle with a radius d and the center which is equal to each point of an estimated boundary. We call the number of the

points the evaluation value for the point. Then, we search the point which maximizes the evaluation value. The found point is considered as an edge point. Next, we search the same way on the condition that the search area is limited to the field which is not within the circles with a radius d and the center which is equal to the found edges so far. This procedure is repeated. We adopt the detected edge points whose evaluation values are larger than $-n$dB of the maximum evaluation value.

We apply the algorithm for edge points detection mentioned above. Here we use an empirically chosen parameters of $d = 0.2\lambda$, and $n = 10$. The two circle symbols in Fig. 3.14 show the detected edge points. The both edge locations are estimated accurately.

3.5.4   The Application Limitation of IBST

In this subsection, we examine the application limitation of IBST. Firstly, we consider a case that we do not obtain a directly scattered wave from a part of target. We show an application example of IBST for a curved target with a cylinder in its foreground. In Fig. 3.15 the solid line and the broken line show the true boundary and the estimated boundary, respectively. We see in the figure that IBST cannot reconstruct the part of the target behind the other object. Additionally, the upper part of the cylinder is not estimated either. In this way, the part of targets without directly scattered wave cannot be estimated by our algorithm.

Next, we explain another limitation of IBST. If the target is a circle whose center is on the scanning line of the antenna, the directly scattered waves shrink to only one point in d-space, which we mentioned in section 3. In this case, we can not estimate the boundary with the extraction algorithm of quasi wavefronts. We may deal with this problem by searching an isolated point with large power. In this case, we should distinguish the peaks caused by circle-shaped surfaces from peaks caused by noises. In anyway, further studies are required to solve the problem.
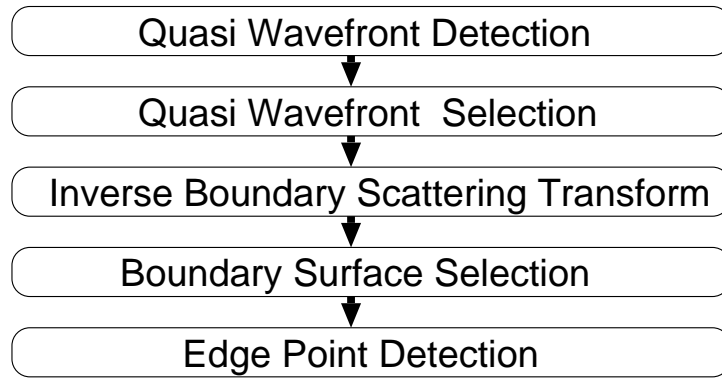
Figure 3.1: Outline of the proposed algorithm.
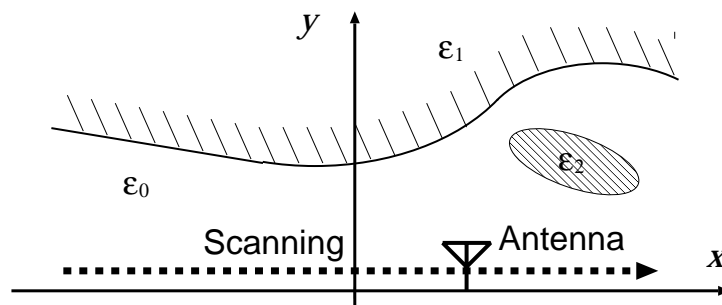
Figure 3.2: The coordinates and an example of a target complex permittivity.
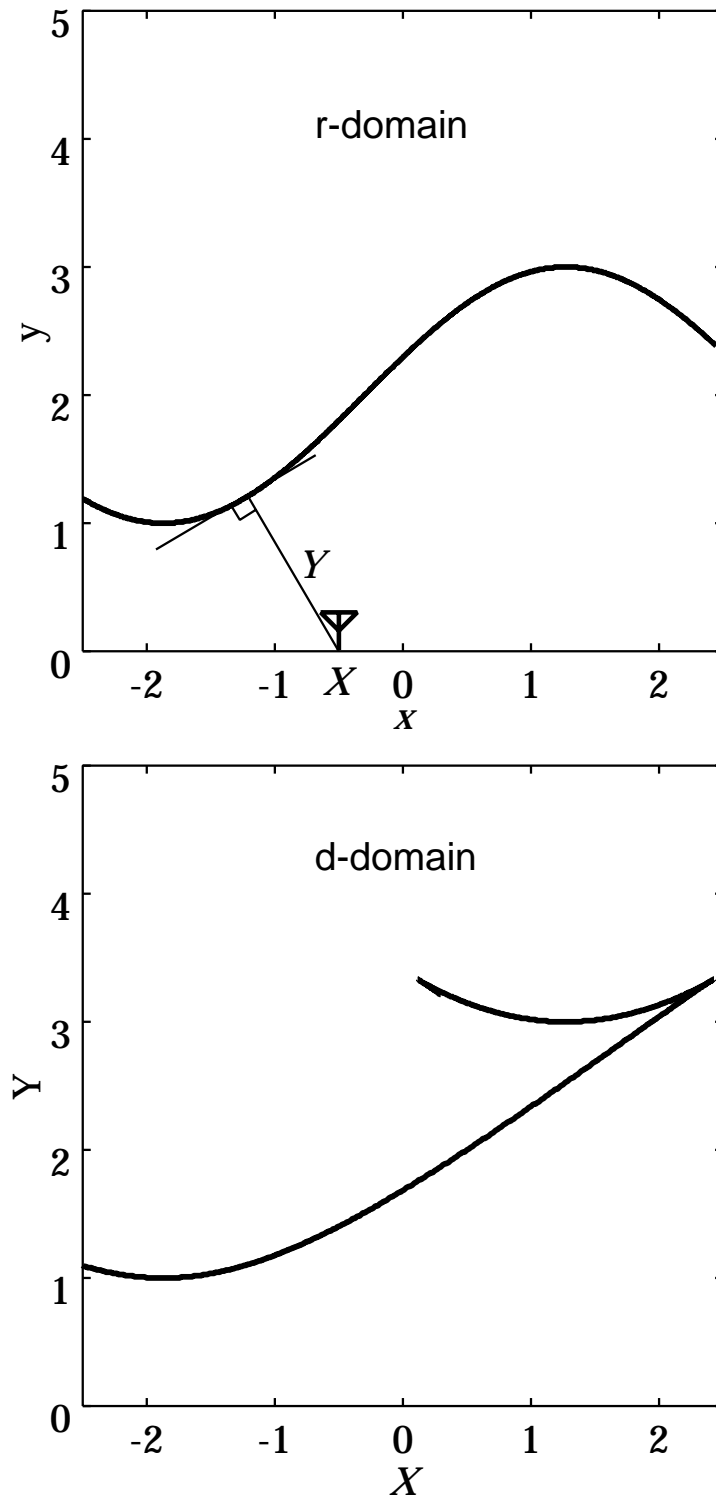
Figure 3.3: An example of Boundary Scattering Transform.
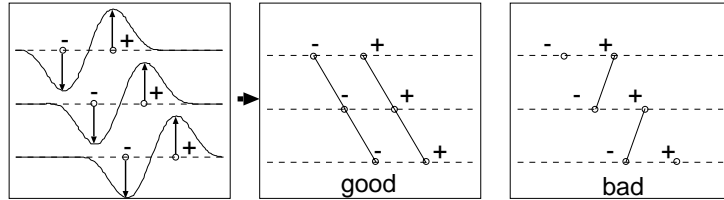
Figure 3.4: Amplitude and quasi wavefronts.
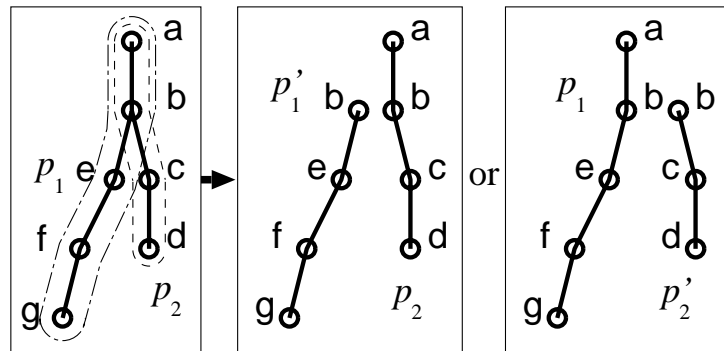
Figure 3.5: Outline of division algorithm for quasi wavefronts.

60
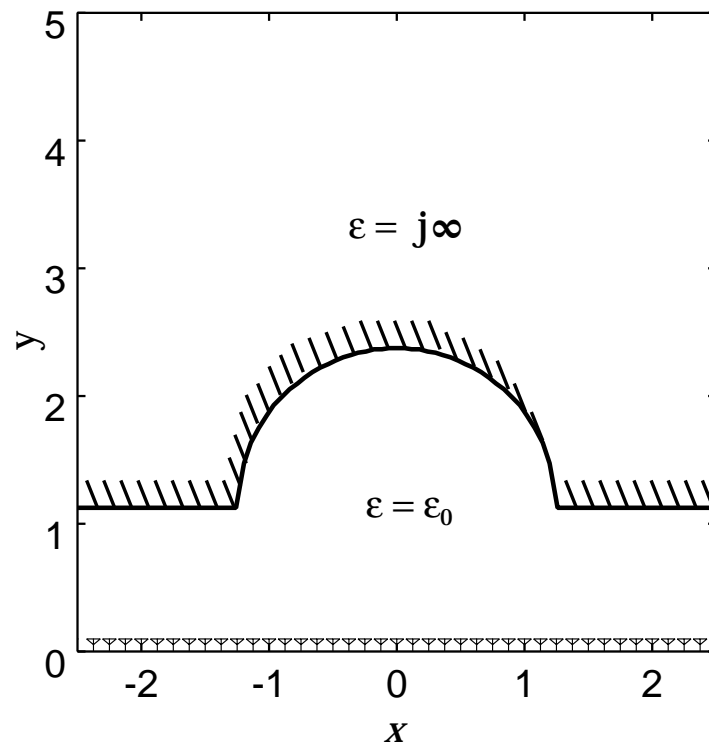
Figure 3.6: The target boundary surface used for the application example.
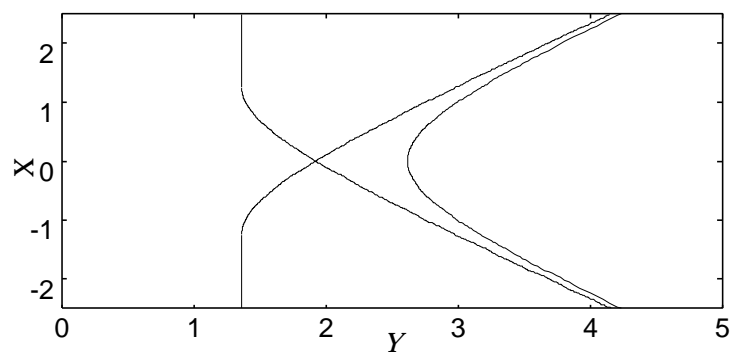
Figure 3.7: BST of the target boundary surface in Fig. 3.6.
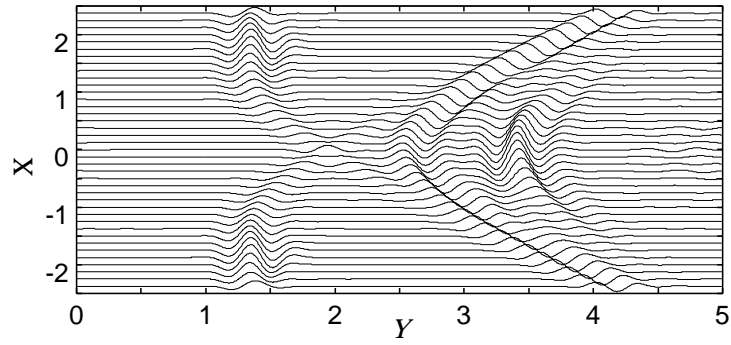
Figure 3.8: An example of received signal $s(X,Y)$.
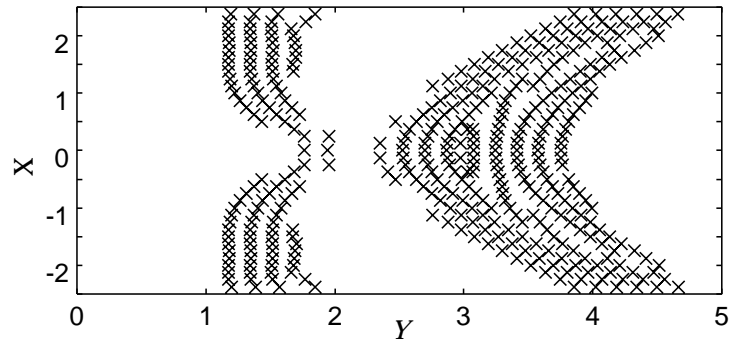
Figure 3.9: Extraction of set P from data $s(X,Y)$.
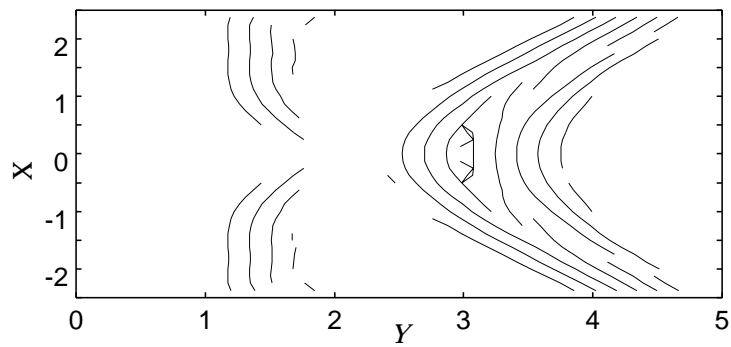
Figure 3.10: Extraction of quasi wavefront $p \in G$ from data $s(X,Y)$.
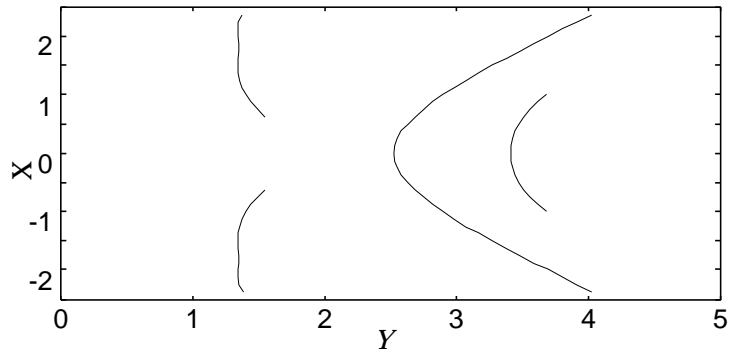
Figure 3.11: Selection of quasi wavefronts using evaluation values.
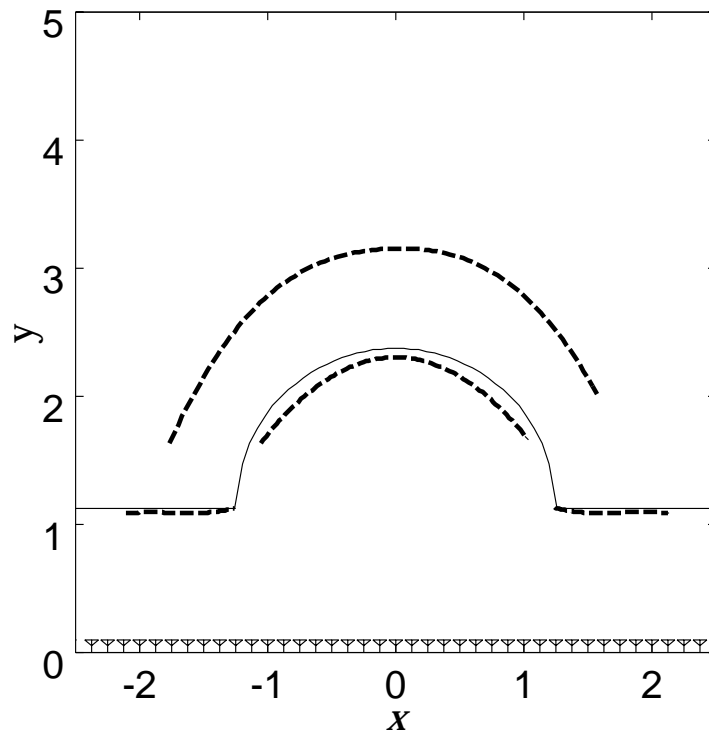
Figure 3.12: An example of application of IBST.

63
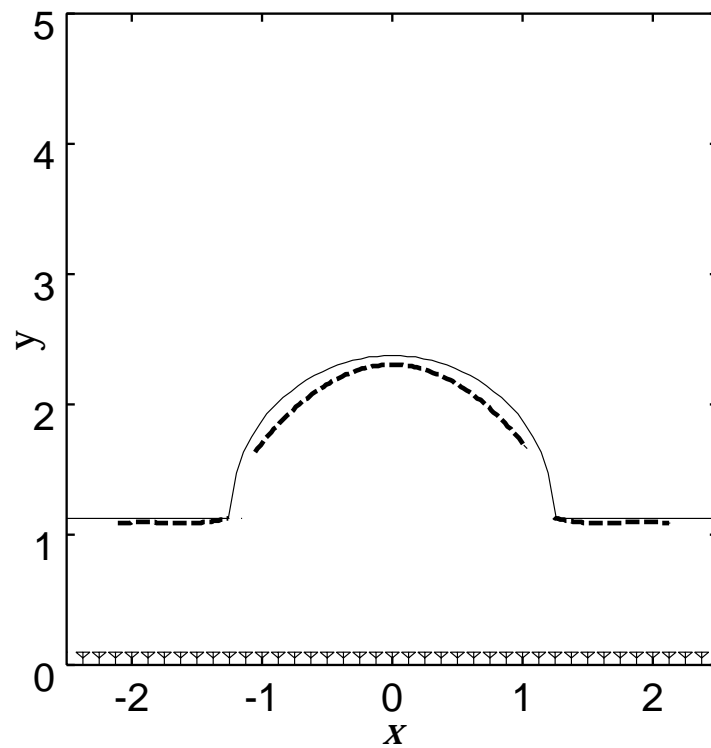
Figure 3.13: The estimated target shape by false image reduction algorithm.
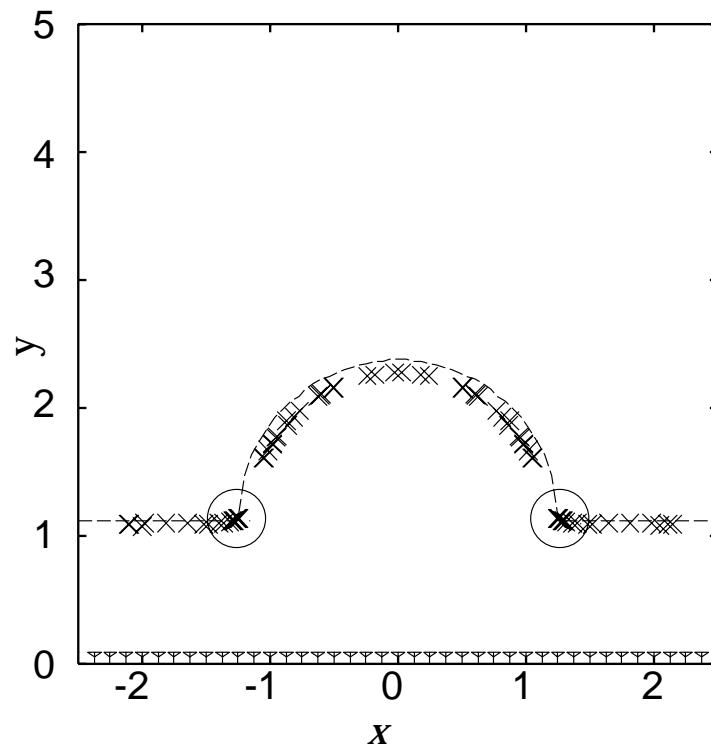
Figure 3.14: The target boundary surfaces sampled at non-equi-interval and the detected edge points.
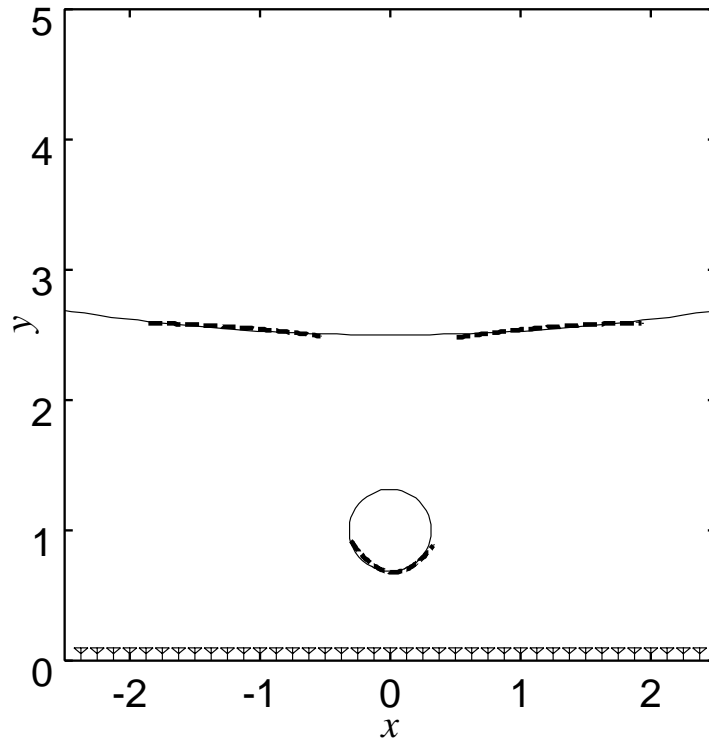
Figure 3.15: An application example of IBST for a target boundary with an obstacle cylinder.
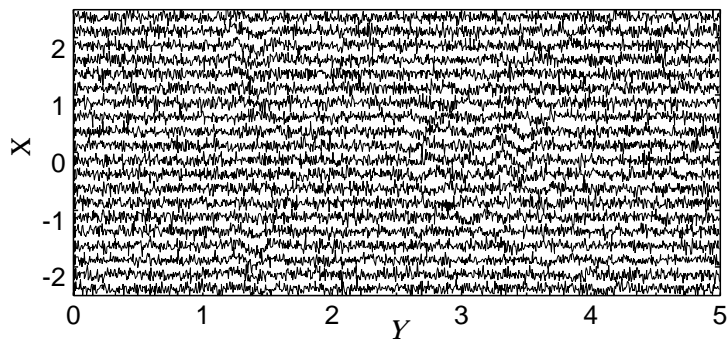
Figure 3.16: A raw signal $s'(X, Y)$ for S/N = 3dB.
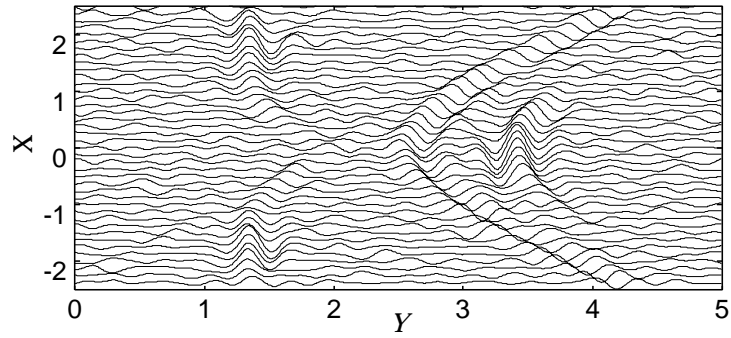
Figure 3.17: A received signal $s(X, Y)$ for S/N $= 3$dB.
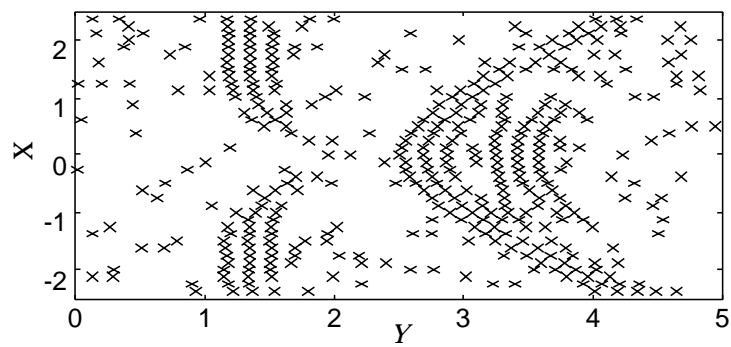
Figure 3.18: Extraction of set P from data $s(X, Y)$ for S/N $= 3$dB.

67
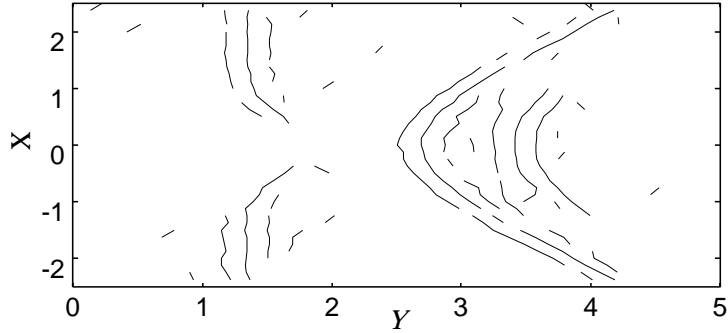
Figure 3.19: Extraction of quasi wavefront $p \in G$ from data $s(X, Y)$ for S/N = 3dB.
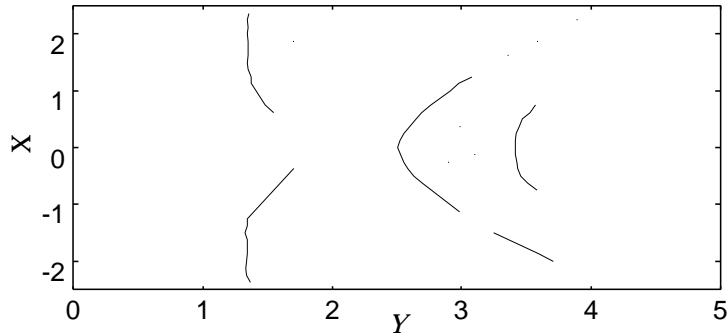
Figure 3.20: Selection of quasi wavefronts using evaluation values for S/N = 3dB.

3.6 Performance against Noise

We investigate the performance of the proposed algorithm in a noisy environment. Fig. 3.16 shows the raw received signal $s'(X, Y)$ for S/N = 3dB. Fig. 3.17 shows $s(X, Y)$, which is the output signal of a matched filter for the raw signal in Fig. 3.16. The signal power is not uniquely defined because the signal is not stationary. Here, we define S as

$$S = \frac{1}{X_{\max} - X_{\min}} \int_{X_{\min}}^{X_{\max}} \max_{Y} |s(X, Y)|^2 \, \mathrm{d}X. \tag{3.20}$$

This definition utilizes the average of a maximum instantaneous power for each antenna location as the signal power.

Fig. 3.18 shows the extracted set P from $s(X, Y)$ in Fig. 3.17 using the proposed algorithm. Many undesired points appear in the figure compared to that in Fig. 3.9. Fig. 3.19 shows $\cup_{p \in G} p$, which is the set of all quasi wavefronts. Most of undesired points in Fig. 3.18 disappear because they do not satisfy the condition $|\mathrm{d}Y/\mathrm{d}X| \leq 1$. Therefore,

68
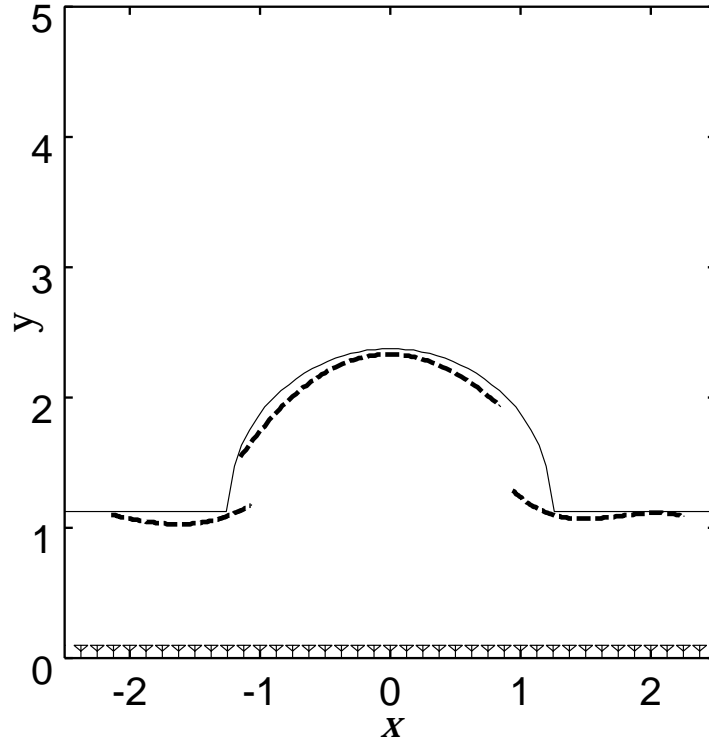
Figure 3.21: The estimated target shape for S/N = 3dB.

meaningful quasi wavefronts are extracted by our algorithm. However, some residual undesired quasi wavefronts remain in the figure. Next, we apply our selection algorithm using evaluation value in Eq. (3.17) to $p \in G$ in Fig. 3.19. Fig. 3.20 shows the selected quasi wavefronts by our selection algorithm. The extracted quasi wavefronts in the figure are slightly different from those in Fig. 3.11. They are distorted by noise, and a part of the quasi wavefront from the concave surface disappears in the figure. However, all desired quasi wavefronts are correctly extracted by the proposed algorithm.

Fig. 3.21 shows the estimated target shape by applying IBST and multiple scattering reduction algorithm to the extracted quasi wavefronts in Fig. 3.20. Although the estimated target shape in Fig. 3.21 is inferior to Fig. A.8, the outline of the target shape is estimated successfully. Consequently, the proposed algorithm has a robustness even for a poor S/N such as 3dB.

3.7   Conclusion

We proposed a non-parametric algorithm of estimating target shapes for UWB pulse radar systems. We clarified the existence of a reversible transform between a target shape and

69

a delay time image, which we call BST and IBST. The proposed algorithm makes use of the transform and achieves a high resolution imaging.

Firstly, we extracted quasi wavefronts from a received signal. We proposed quasi wavefront extraction, division, and selection algorithms using an evaluation value, which remove undesirable quasi wavefronts caused by noise and ringings. Next, we applied IBST to the data to estimate the target shapes. The target shape estimation using IBST has a remarkable performance. Moreover, we proposed a false image reduction algorithm caused by multiple scattering. We have shown that the algorithm removed the false images completely. In addition, we proposed an edge locationing algorithm using IBST, and showed an application example. We clarified that the estimation accuracy is about 0.15 wavelength in the worst case. This error can be suppressed by the phase compensation algorithm proposed in Sec. 5. We also investigated the performance of the proposed algorithm in a noisy environment. The proposed algorithm has a good performance for S/N=3dB. The achieved accuracy is sufficient for most of applications.

Chapter 4

The Performance of SEABED Algorithm for Inhomogeneous Media

4.1   Introduction

Mine detection is an important social issue, for which ground penetrating radars are promising candidates. It is required to develop an efficient algorithm for ground penetrating radars. Some imaging algorithms which we described in the previous chapters may be applied to inhomogeneous media. The conventional algorithms in general have problems of long calculation time and instability even for inhomogeneous media. It is required to develop a fast and stable algorithm for radar imaging for mine detection in inhomogeneous media. The proposed SEABED algorithm has a characteristic that it can quickly and directly estimate a target shape as a line, which is a remarkable advantages compared to conventional ones. We have confirmed the high performance of SEABED algorithm for homogeneous media in the previous chapter. Inhomogeneity of underground is one of the most difficult problem to overcome for mine detection. In this chapter, we examine the performance of SEABED algorithm for inhomogeneous media by numerical simulations.

4.2   Shape Estimation in Homogeneous Media

We assume a mono-static radar system, which is same as the assumption of the previous section. An omni-directional antenna is scanned along a straight line. UWB pulses are transmitted at a fixed interval and received by the antenna. The received data is A/D converted and stored in a memory. We estimate target shapes using the data.

We first show an application example of SEABED algorithm for a cylindrical target in homogeneous media, which is meaningful to compare the result for inhomogeneous media. We assume a cylindrical perfect conductor with radius of 1λ as an example target.
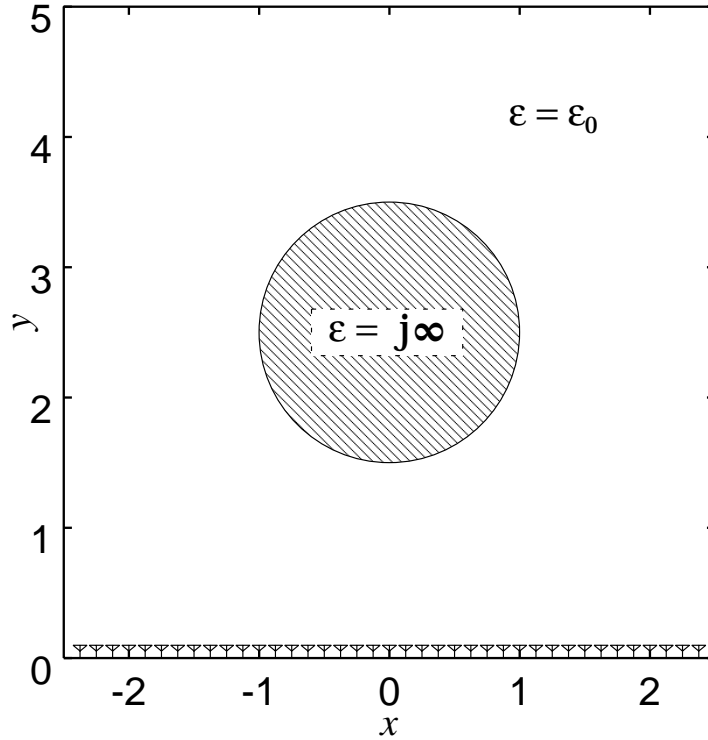
Figure 4.1: Target shape example.

Fig. 4.1 shows an example of target boundary surface. The inner domain is filled with perfect electric conductor, and the outer domain is filled with air. The symbols on the bottom in this figure are the points where the data is obtained. Fig. 4.2 shows the received data $s(X,Y)$ which is calculated with FDTD (Finite Difference Time Domain) method. The antenna receives the signal at 39 locations with intervals of 0.125λ. We assume S/N $= \infty$ for simplicity.

Fig. 4.3 shows the extracted quasi wavefronts from the received data. By applying IBST to the quasi wavefront, we obtain the estimated target shape as in Fig. 4.4. In this figure, the solid line and broken line are the true shape and estimated shape, respectively. The lower side of the target boundary is accurately estimated by SEABED algorithm. The upper side of the target is not estimated because SEABED requires the directly scattered signal. As a result, we can conclude that SEABED algorithm works well for shape estimation of a target in homogeneous media.
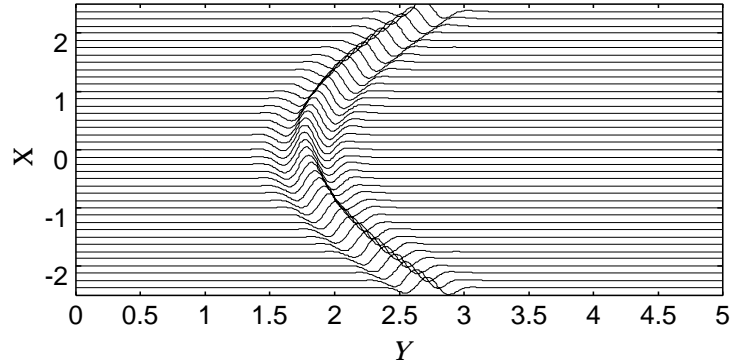
Figure 4.2: Received signal in homogeneous media.
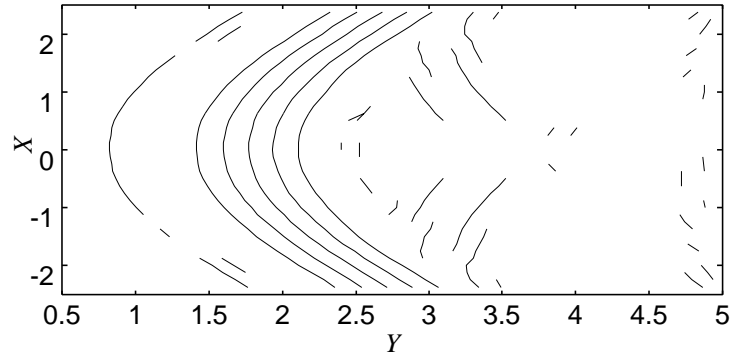
Figure 4.3: Extracted quasi wavefronts in homogeneous media.

4.3 Shape Estimation in Inhomogeneous Media

4.3.1 Performance for Random Media

In this section, we investigate the estimation performance of SEABED algorithm for inhomogeneous media. The target shape is a cylindrical perfect conductor with radius of 1λ which is the same one as shown in Fig. 4.1. The media around the target has highly inhomogeneous dielectric, whose relative permittivity ε_r is shown in Fig. 4.5. This permittivity is obtained by applying a two-dimensional spatial LPF (Low Pass Filter) with the cut-off of the half-wavelength to a random image with a normal distribution. The distribution of the relative permittivity has the mean of 1, and the standard deviation of 0.5. We assume this mean is known as a priori information. The central round region with relative permittivity of 1 corresponds to the region of the target. Fig. 4.6 shows the received signal for the target in this random media. We see many undesirable components in this figure compared to the the signal in homogeneous media. Fig. 4.7 shows the
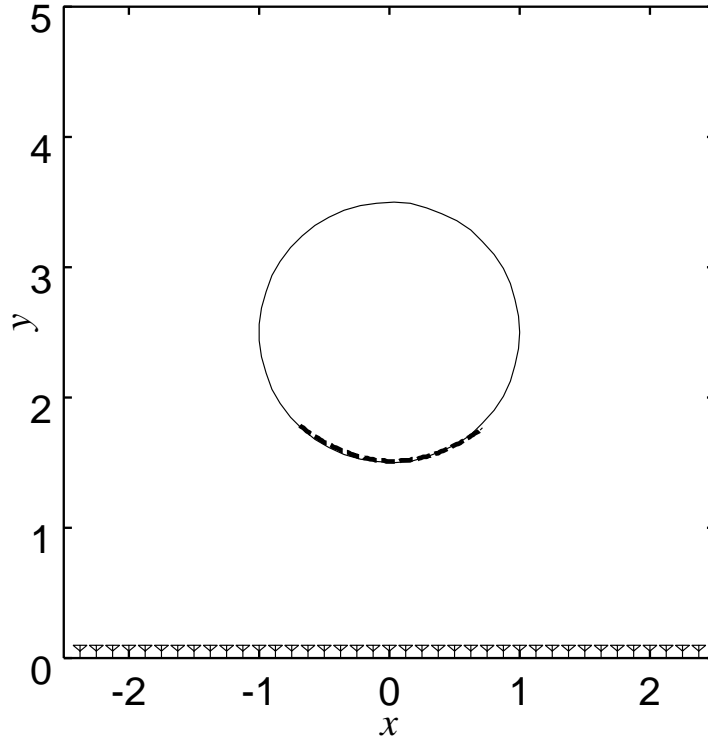
Figure 4.4: Estimated target shape in homogeneous media.

extracted quasi wavefronts from the signal in Fig. 4.6. We see many undesirable quasi wavefronts together with a desirable one. However, most of the undesirable quasi wavefronts are not connected smoothly with each other, which makes their evaluation value small, which enables to eliminate the undesirable components. We apply IBST to the quasi wavefronts whose evaluatin value greater than −5dB of the maximum evaluation value. We utilize the mean of the permittivity when applying IBST. Fig. 4.8 shows the estimated target shape by IBST. The solid line and broken line are the true target shape and the estimated target shape, respectively. We see that the target shape is correctly estimated to some extent although the estimation is less accurate than in the homogeneous media. Additionaly, we see that the undesirable components are removed because their evaluation value become smaller than that of the desirable one. If we set the threshould of evaluation value to −10dB, the estimation image contains undesirable components caused by the random media, which show the importance of the selection of the threshould.
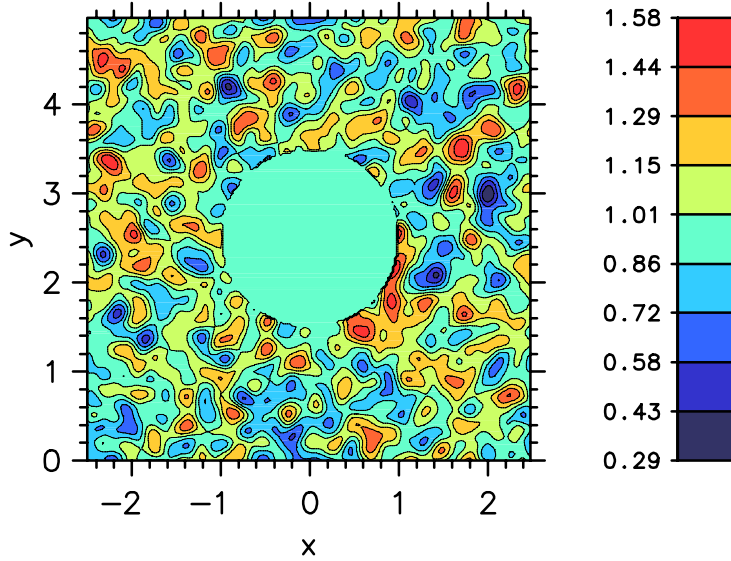
Figure 4.5: Permittivityε_r of random media.

4.3.2 Performance for Layered Media

Next, we investigate the performance of SEABED algorithm for layerd media. The target shape is a cylindrical perfect conductor which is the same one used in the previous chapter. We obtain this permittivity by applying LPF for y-direction with a cut-off of half-wavelength to a random image. The mean of the relative permittivity is 1, which we assume to be a priori information. Fig. 4.10 shows the received signal in the layered media. We can observe many scattered wave from the layers close to the antenna. The scattered wave from the target is smooth compared to those in the random media. Fig. 4.11 shows the extracted wavefronts in the layered media. We see the desired component and undesirable components caused by the layers. We apply IBST to the quasi wavefronts whose evaluatin value greater than -5dB of the maximum evaluation value. Fig. 4.12 shows the estimated target shape in the layered media. The solid line and broken line are the true target shape and estimated target shape, respectively. We see that SEABED algorithm also works well for layered media as in this figure. However, we can observe the offset error caused by the layered media between the antenna and the target.

The imaging took 40 msec with Xeon 2.8GHz processor, which is considerably fast. The calculation time is independent of the media and the shape of targets because SEABED algorithm utilize the reversible transform. We have confirmed the efficiency of SEABED algorithm even in inhomogeneous media.
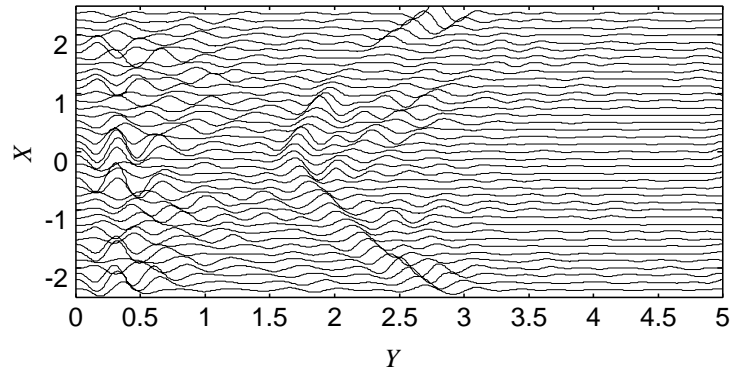
Figure 4.6: Received signal in random media.
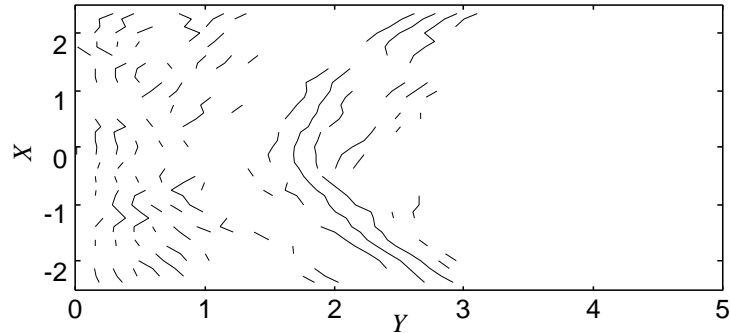
Figure 4.7: Extracted quasi wavefronts in random media.

4.4 Conclusion

We investigated the performance of SEABED algorithm, which we proposed in the previous section, for inhomogeneous media. The simulation result shows that SEABED algorithm works well even in inhomogeneous media on some conditions as follows:

- The mean of random permittivity should be known.

- The threshold for evaluation value of quasi wavefronts should be suitably selected.

Further studies are needed to overcome these difficulties. As for calculation time, the imaging took 40 msec with Xeon 2.8GHz processor. The calculation time of SEABED algorithm is sufficiently short, which enables a realtime operation with this algorithm.

76
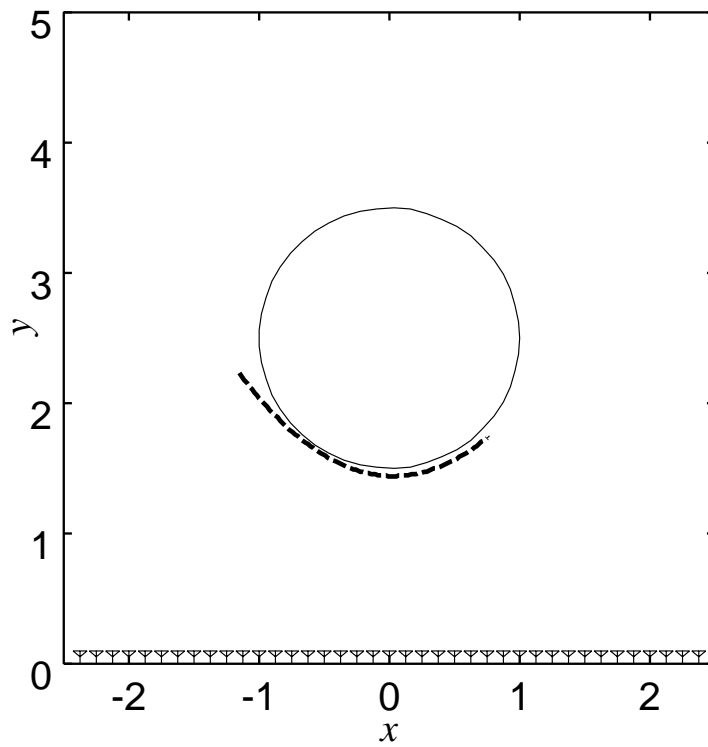
Figure 4.8: Estimated target shape for random media.
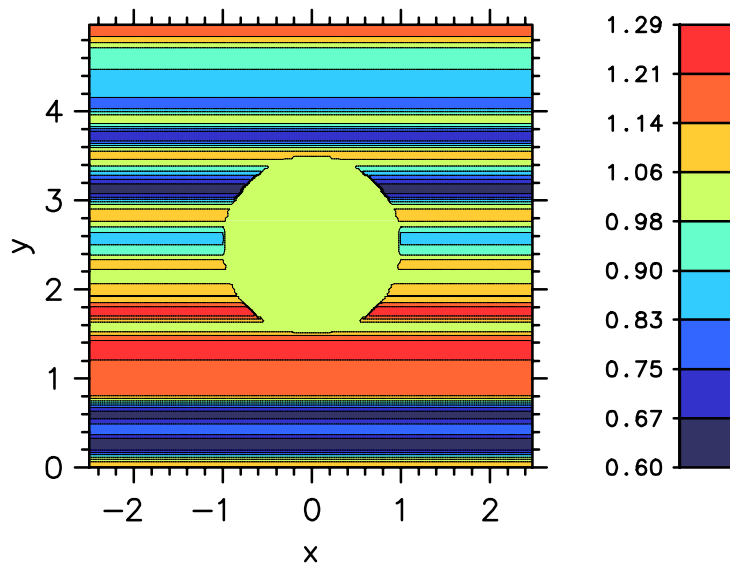
Figure 4.9: Permittivityε_{r} of layered media.
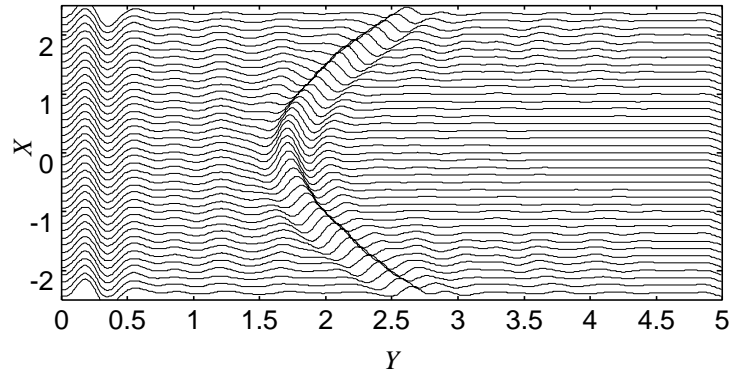
Figure 4.10: Received signal in layered media.
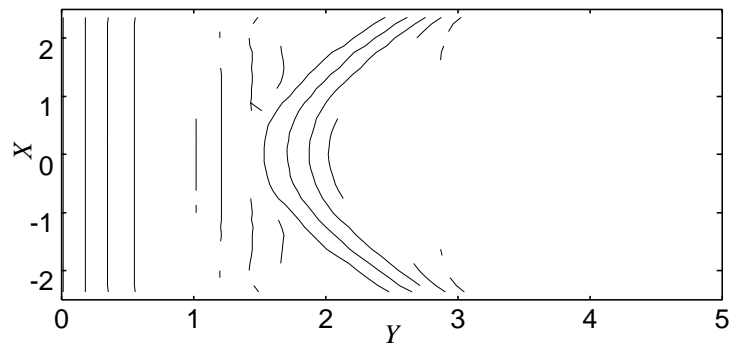
Figure 4.11: Extracted quasi wavefronts in layered media.
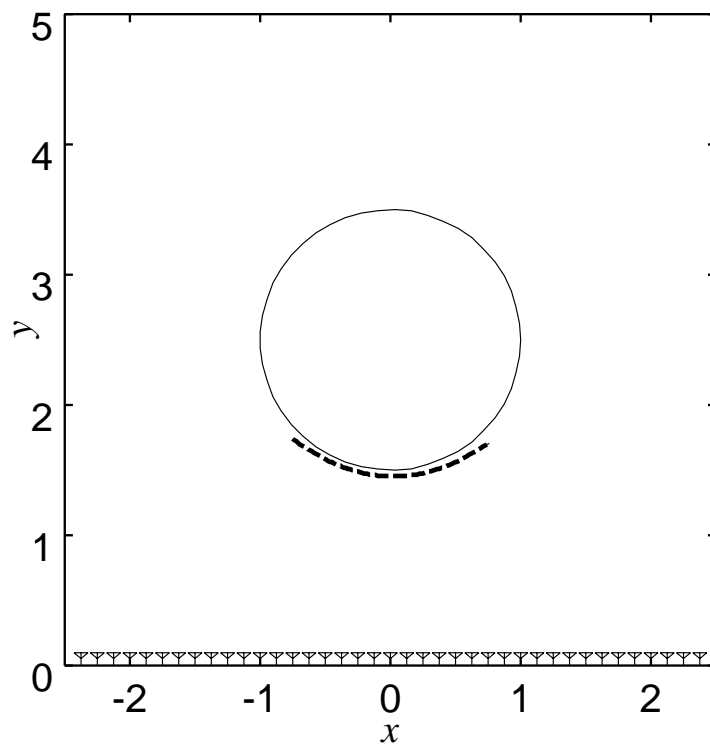
Figure 4.12: Estimated target shape for layered media.

Chapter 5

Phase Compensation Algorithm for High-Resolution Pulse Radars

5.1 Introduction

High-resolution algorithms utilize not only the envelope of the received signal but also the phase of carrier signal. However, it should be noted that the received carrier phase depends on the shape of targets. Especially, $\pi/2$ phase rotation caused by concave is well-known in the field of electric-magnetic wave theory. The effect has not been regarded as a serious problem so far for pulse radar systems, because conventional systems having a narrow bandwidth do not deal with the accuracy. However, in the near future, the problem will become a bottleneck in improving the accuracy of radar systems using UWB pulses. In this chapter, we propose an algorithm to compensate the phase rotation caused by the concave and show an application example. The algorithm is presented firstly, which is followed by numerical simulations for validation of the algorithm.

5.2 System Model

We assume a mono-static radar system in this chapter, which is same as in the previous section. An omni-directional antenna is scanned along a straight line. UWB pulses are transmitted at a fixed interval and received by the antenna. The received data is A/D converted and stored in a memory. We estimate target shapes using the data. We deal with a 2-dimensional problem, and TE-mode wave. Targets and the antenna are located on a plane.

5.3 Phase Rotation and High-resolution Imaging

5.3.1 Phase Rotation and Boundary Shape

In this section, we explain the $\pi/2$ phase rotation caused by concaves. A wave changes its phase after it passes through a caustic [86, 87]. Here, physically singular points are called caustics. The similar effect is also known in the field of optics, which is called Guoy phase [88].

First, we introduce geometric optics in order to explain this effect. By using Luneburg-Kline expansion, an electric field can be expressed as

$$E(\boldsymbol{r}) \simeq \mathrm{e}^{-\mathrm{j}k\Phi(\boldsymbol{r})} \sum_{m=0}^{\infty} (-\mathrm{j}k)^{-m} E_m(\boldsymbol{r}), \tag{5.1}$$

where k is the wave number, $E(\boldsymbol{r})$ is the electric field at the position vector $\boldsymbol{r}$ and $\Phi(\boldsymbol{r})$ is called eikonal. Constant values of the eikonal represent surfaces of constant phase. Therefore, $\nabla\Phi$ represents the direction of the propagation.

The reflected wave comes from the part of target boundary which is orthogonal to $\nabla\Phi$ as in Fig. 5.1. This means that the electromagnetic wave of constant phase along the target boundary is re-emitted toward the antenna. In the figure, E_0 is the 0-th factor of the reflected electric field in Eq. (5.1). Therefore, $E_0(\sigma_1)$ in Fig. 5.1 can be expressed with $E_0(\sigma_0)$ using GO (Geometric Optics) theory as

$$E_0(\sigma_1) = \sqrt{\sigma_0/\sigma_1}E_0(\sigma_0). \tag{5.2}$$

In the same way, we obtain $E_0(-\sigma_2)$ using GO theory as

$$E_0(-\sigma_2) = \sqrt{-\sigma_0/\sigma_2}E_0(\sigma_0). \tag{5.3}$$

Note that the inside of the square root in Eq. (5.3) becomes negative in this case because $\sigma_0, \sigma_2 > 0$ holds. We can interpret the negative value in square root as an imaginary number, which means the phase of $E_0(\sigma_2)$ is advanced compared to $E_0(\sigma_0)$ by $\pi/2$. This explanation helps us to develop a phase compensation algorithm because it is obvious what is the main factor of the phase rotation.

5.3.2 An Example of Phase Rotation

In this subsection, we show an example of phase rotation explained in the previous subsection. Fig. 5.2 shows a received waveform for each antenna position. Here, the antenna is omni-directional and used as a monostatic radar. The target is a round perfect conductor with a concave at the bottom side. Note that the antenna "a" is inside the concave and the antenna "b" is outside the concave. The received waveform ideally corresponds to an auto-correlation function of the original waveform only if the received signal suffers no

81
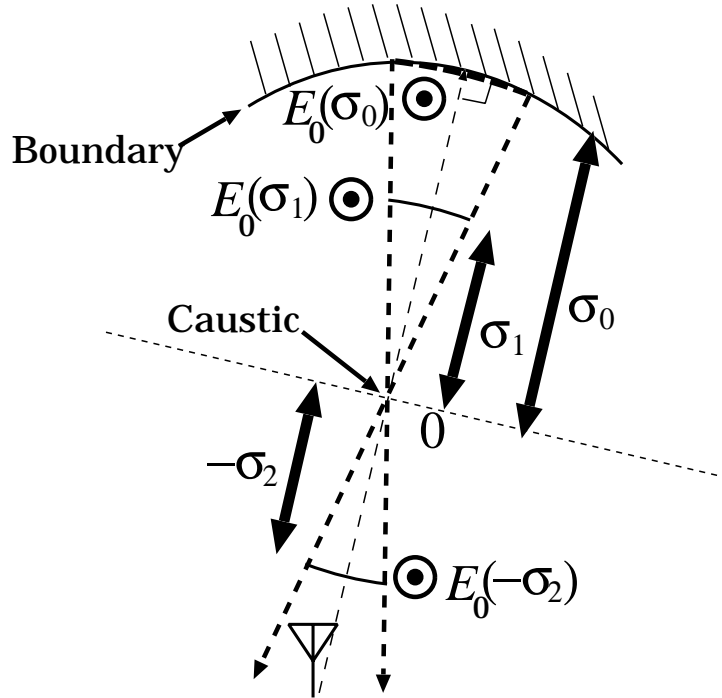
Figure 5.1: A concave and phase rotation of signal.

phase rotation because the received waveforms are the output of a matched filter. The waveform "a" has a peak at the center because it has not passed through a caustic. On the other hand, the waveform "b" has a peak shifted by $\lambda/4$. We have also confirmed the difference of peak positions between "a" and "b" is precisely $\lambda/4$, which means the phase rotation of $\pi/2$. All we have to do is to detect the waves which passed through caustics and to compensate for the phase rotation.

5.4 SEABED Algorithm

5.4.1 Outline of SEABED Algorithm

We propose a phase compensation algorithm in this chapter. As an example, we utilize SEABED algorithm because it has an advantage that the detection of caustic is easy compared to other methods. Here, we briefly explain the SEABED algorithm first.

We have already described a non-parametric shape estimation algorithm based on BST (Boundary Scattering Transform). We call the algorithm SEABED. The algorithm utilizes the existence of a reversible transform BST between target shapes and pulse delays. However, phase rotations of scattered waves caused by concave surfaces cause a
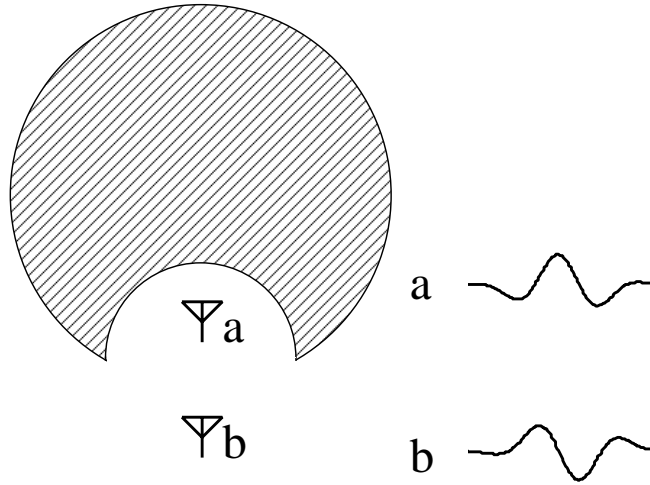
Figure 5.2: Phase rotation and antenna position.

great deal of degradation in estimating accuracies. We have proposed an algorithm which simultaneously estimates target locations and scattered waveforms in Chapter 2. The algorithm works well, but it is applicable only for point targets. Therefore, it is required to develop a phase compensation algorithm which can estimate the shape of more general targets.

5.4.2 Boundary Scattering Transform

The SEABED utilizes the existence of a reversible transform between quasi wavefronts and target boundary surfaces. We assume that each target has a uniform complex permittivity, and surrounded by a smooth boundary. We also assume that the propagation speed is known. Here, we assume the medium of direct path is vacuum for simplicity.

Boundary Scattering Transform (BST) is expressed as

$$X = x + y \mathrm{d}y/\mathrm{d}x, \tag{5.4}$$

$$Y = y\sqrt{1 + (\mathrm{d}y/\mathrm{d}x)^2}, \tag{5.5}$$

where (X, Y) is a point on a quasi wavefront. (x, y) is a point on target boundary, and we assume $y > 0$ and $Y > 0$. We have clarified that the inverse transform of BST is given by

$$x = X - Y \mathrm{d}Y/\mathrm{d}X, \tag{5.6}$$

$$y = Y\sqrt{1 - (\mathrm{d}Y/\mathrm{d}X)^2}, \tag{5.7}$$

where we assume $|\mathrm{d}Y/\mathrm{d}X| \leq 1$. We call the transform in Eq. (5.6) and (5.7) Inverse Boundary Scattering Transform (IBST).

5.4.3   SEABED Procedure

First, we extract a quasi wavefront from $s(X,Y)$ in SEABED. Quasi wavefronts have to satisfy the condition $\mathrm{d}s(X,Y)/\mathrm{d}Y = 0$ and $|\mathrm{d}Y/\mathrm{d}X| \leq 1$. The latter condition ensures Y in Eq. (5.7) to be a real number. Furthermore, we adopt a condition

$$|s(X_i, Y_i)/s(X_{i+1}, Y_{i+1})| < T_\mathrm{r} \tag{5.8}$$

to prevent an interference, where (X_i, Y_i) and (X_{i+1}, Y_{i+1}) are points on a quasi wavefront and next to each other. This condition is based on that large changes of amplitude in the same quasi wavefront is not rational. We sequentially extract the set of points (X,Y). Next, we select quasi wavefronts with large power and eliminate undesirable components. Finally, we apply IBST to the extracted quasi wavefront and estimate the target shape.

5.4.4   An Application Example of SEABED

We show an example of application of SEABED algorithm. Fig. 5.3 shows an example of target boundary surface. The inner domain in the figure is filled with perfect electric conductor, and the outer domain is filled with air. Estimation of this target shape is one of the most difficult cases because it includes convex surfaces, a concave surface and edge points. In most of actual situations, estimation of a target shape is easier than this example.

Fig. 5.4 shows the received data from the assumed target. We assume S/N $= \infty$ in this section for simplicity. We obtain this signal by utilizing FDTD (Finite Difference Time Domain) method. We receive the signal at the 39 locations whose intervals are 0.125λ. Next, we extract quasi wavefronts using the conditions mentioned in the previous subsection. We adopt an empirically chosen value $T_\mathrm{r} = 1.11$. The extracted quasi wavefronts are shown in Fig. 5.5. Five quasi wavefronts are extracted in the figure. Finally, we obtain the estimated target boundaries by applying IBST to the extracted wavefronts. Fig. 5.6 shows the estimated target boundary surfaces using the SEABED. The symbols located at the bottom of the figure show the locations of the antenna, where we receive signals. The broken line and the solid lines are the real target boundary surface and the estimated target boundary surfaces, respectively. The estimation accuracy on the concave surface suffers degradation compared to the straight surface. This is caused by the phase rotation occurred at the caustic to the echoes from the concave surface.

5.5   Phase Compensation for IBST

5.5.1   Phase Compensation Algorithm for IBST

In the previous section, we described that the SEABED has an estimation error caused by the phase rotation. The phase rotation depends on the shape of target. It is possible
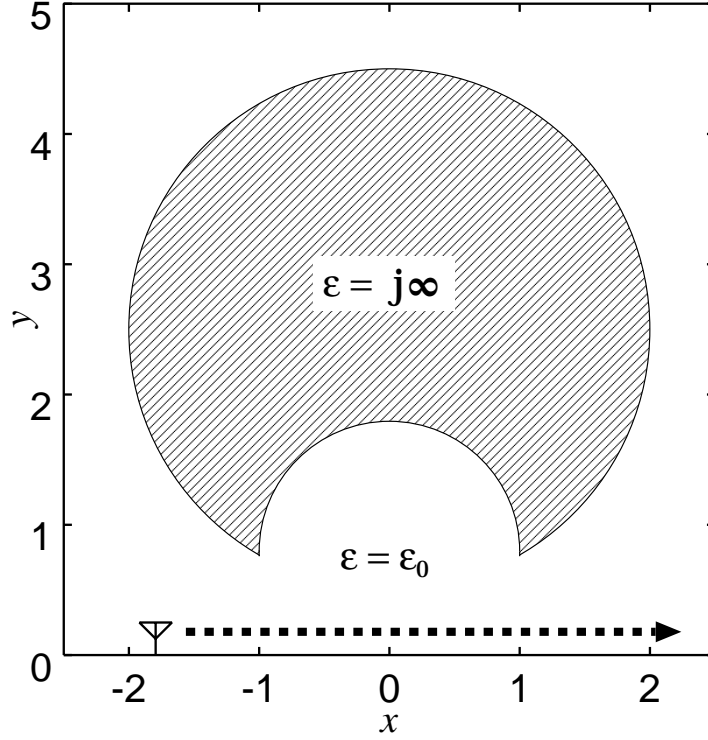
Figure 5.3: Target model.

to compensate for the phase rotation if the condition of phase rotation can be expressed using the extracted quasi wavefronts. We define the IBST vector $\boldsymbol{v}_{\mathrm{IBST}}$ as

$$\boldsymbol{v}_{\mathrm{IBST}} = \left[\begin{array}{c} -Y \, \mathrm{d}Y/\mathrm{d}X, \\ Y \sqrt{1 - (\mathrm{d}Y/\mathrm{d}X)^2} \end{array} \right]. \tag{5.9}$$

Eq. (5.6) and Eq. (5.7) are expressed as

$$\left[\begin{array}{c} x \\ y \end{array} \right] - \left[\begin{array}{c} X \\ 0 \end{array} \right] = \boldsymbol{v}_{\mathrm{IBST}}. \tag{5.10}$$

The caustic curve of a target boundary is given as

$$x_{\mathrm{f}} = x - \frac{\mathrm{d}y/\mathrm{d}x}{\mathrm{d}^2 y/\mathrm{d}x^2} \left\{ (\mathrm{d}y/\mathrm{d}x)^2 + 1 \right\}, \tag{5.11}$$

$$y_{\mathrm{f}} = y + \frac{1}{\mathrm{d}^2 y/\mathrm{d}x^2} \left\{ (\mathrm{d}y/\mathrm{d}x)^2 + 1 \right\}. \tag{5.12}$$

85
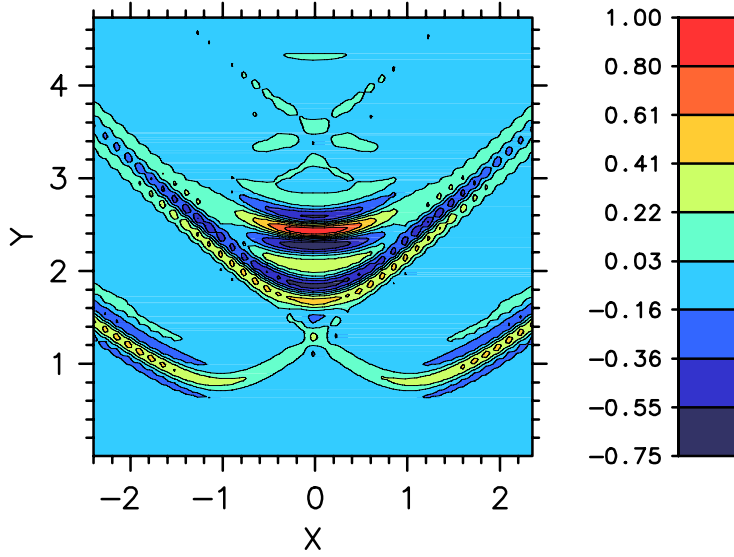
Figure 5.4: Observed signal.

Substituting Eq. (5.7) for Eq. (5.5) and solving for dy/dx, we obtain

$$dy/dx = \frac{dY/dX}{\sqrt{1 - (dY/dX)^2}}. \tag{5.13}$$

Similarly, we obtain d^2y/dx^2 as

$$\frac{d^2y}{dx^2} = \frac{\dfrac{d^2Y}{dX^2}}{\left\{1 - \left(\frac{dY}{dX}\right)^2\right\}^{3/2} \left\{1 - \left(\frac{dY}{dX}\right)^2 - Y\frac{d^2Y}{dX^2}\right\}}. \tag{5.14}$$

It is remarkable that the 1st- and 2nd-order derivatives of the target boundary is expressed using the quasi wavefront and its 1st- and 2nd-order derivatives. It is thus possible to express the right-hand side of Eq. (5.11) and Eq. (5.12) using the quasi wavefront and its 1st- and 2nd-order derivatives. We obtain

$$\begin{bmatrix} x_{\mathrm{f}} \\ y_{\mathrm{f}} \end{bmatrix} - \begin{bmatrix} X \\ 0 \end{bmatrix} = \tan\phi \boldsymbol{v}_{\mathrm{IBST}}, \tag{5.15}$$

where ϕ is defined as

$$\phi = \tan^{-1}\left\{\frac{1 - (dY/dX)^2}{Y\,d^2Y/dX^2}\right\}. \tag{5.16}$$

We see that a caustic is on the line which connects the antenna and the boundary. ϕ is the parameter which shows the relative position of the caustic for the antenna. As
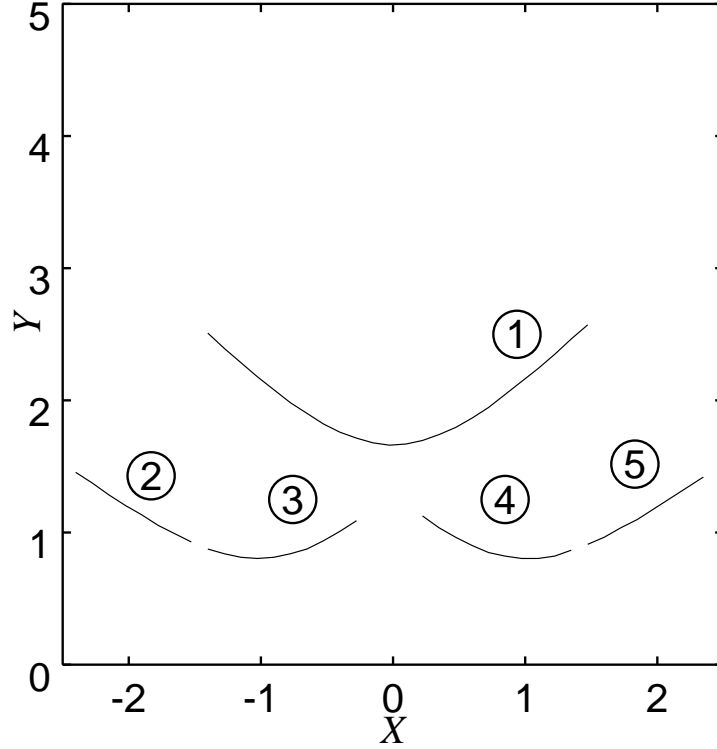
Figure 5.5: Extracted quasi wavefronts.

we mentioned in the previous section, we observe the phase rotation of $\pi/2$ in received signals if the antenna is located in the outer part of caustic for a concave boundary. This condition can be expressed using the quasi wavefront as

$$0 < \phi < \pi/4. \tag{5.17}$$

The relationship between ϕ and target shapes is shown in Table. 5.1. Fig. 5.7 illustrates the angle ϕ and the target shape. Fig. 5.8 explains the meaning of ϕ using $\boldsymbol{v}_{\mathrm{IBST}}$ and $\boldsymbol{v}_{\mathrm{c}}$, where we define $\boldsymbol{v}_{\mathrm{c}} = [x_{\mathrm{f}}, y_{\mathrm{f}}]^{\mathrm{T}} - [X, 0]^{\mathrm{T}}$.

In order to compensate for the phase rotation, we modify IBST as

$$x = X - \{Y + f(\phi)\}\, \mathrm{d}Y/\mathrm{d}X, \tag{5.18}$$

$$y = \{Y + f(\phi)\}\, \sqrt{1 - (\mathrm{d}Y/\mathrm{d}X)^2}, \tag{5.19}$$

where $f(\phi)$ is defined as

$$f(\phi) = \begin{cases} 1/8 & (0 < \phi < \pi/4) \\ 0 & (\text{otherwise}). \end{cases} \tag{5.20}$$

87
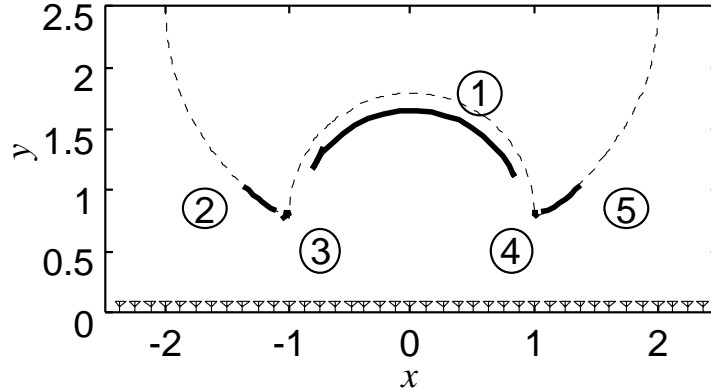
Figure 5.6: Estimated target shape using SEABED.

Table 5.1: ϕ and the relative location of caustic for the antenna.

ϕ	shape
$-\pi/2$	plane
$\vdots$	inside of concave
0	on caustic of concave
$\vdots$	outside of concave
$\pi/4$	point target
$\vdots$	convex
$\pi/2$	plane

Note that the compensation of $\lambda/8$ is required because the phase rotation $\lambda/4$ corresponds to a round-trip delay. We can directly detect a caustic and antenna position with quasi wavefronts utilizing ϕ.

5.6 An Application Example of the Phase Compensation Algorithm

In this section, we show an application example of the phase compensation algorithm. We assume S/N $= \infty$ in this section for simplicity. Fig. 5.9 shows a calculated ϕ for each quasi wavefront. The calculated ϕ is plotted with X in the figure. Calculated ϕ are located in the correct region for quasi wavefronts "2" and "5". On the other hand, edge diffraction "3" and "4" have ϕ around $\pi/4$, which means it is close to a point target. As for quasi wavefront "1", calculated ϕ is about $\pi/8$ at the center, but the both ends has
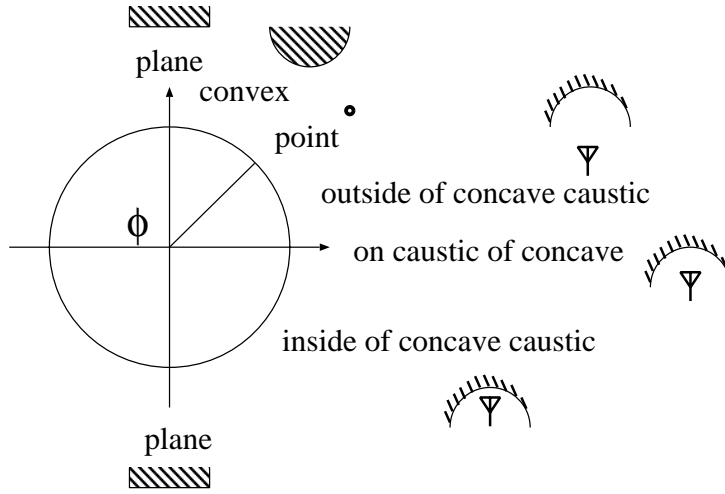
Figure 5.7: ϕ and boundary shape.
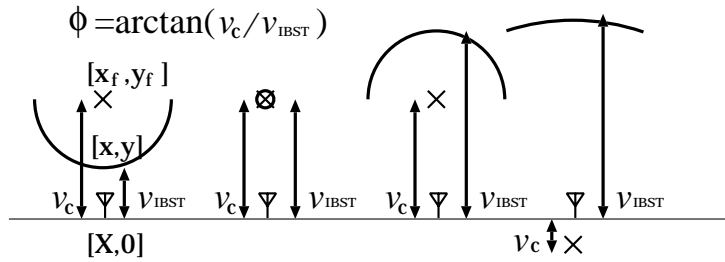
Figure 5.8: Locations of antenna, caustic and target.

wrong ϕ in the convex region.

We show an application example of the modified IBST using the calculated ϕ above. Fig. 5.10 shows the estimated target shapes using the modified IBST. Most of the errors at the caustic in Fig. A.8 are improved in this case. However, the both ends of "1" still have error because they are regarded as convex by the algorithm. Furthermore, the estimation of edge points have error in this case because part of them are regarded as concave and undesirable phase compensation was made.

In order to prevent the problems of phase compensation, we propose another algorithm for phase compensation. First, we calculate the average ϕ for each quasi wavefront. Next, we determine phase compensation using the averaged ϕ. We set margin for the threshold to make the algorithm stable. We adopt empirically chosen condition $5° < \phi < 40°$ for phase compensation. Averaged ϕ for each quasi wavefront is shown in Table. 5.2. Fig. 5.11 shows the estimated target shape using averaged ϕ. We see the estimation accuracy is improved without sacrificing the resolution.
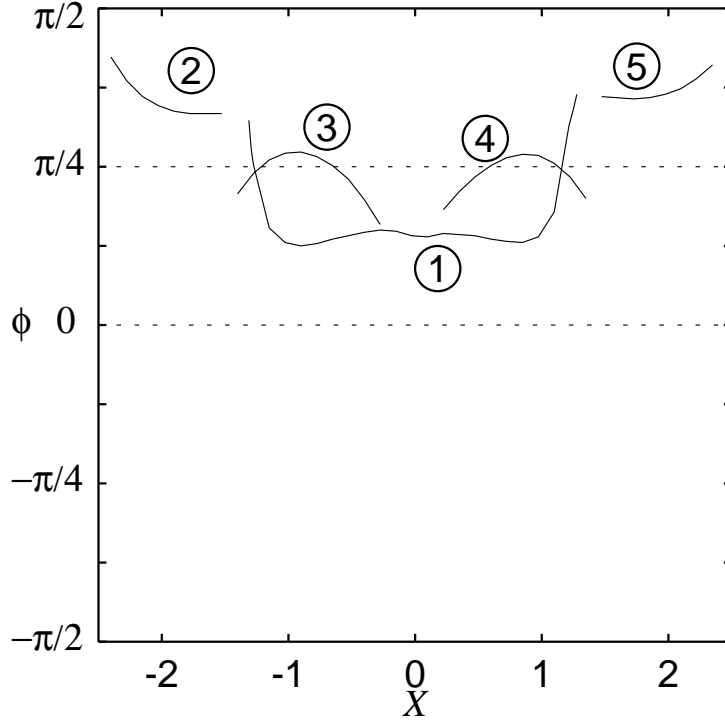
Figure 5.9: ϕ for each quasi wavefront.

5.7 Limitation of the Proposed Algorithm

In this section, we explain the limitation of the proposed algorithm. First, we investigate the performance of the proposed algorithm in a noisy environment. Fig. 5.12 shows the simulation result of the shape estimation for S/N=20dB. The proposed algorithm works well to some extent in this case even with noise. However, one of the edge points ("3" in Fig. 5.11) is not estimated because the power of the diffracted wave is smaller than that of the reflected waves. Fig. 5.13 shows the simulation result of the shape estimation for S/N=10dB. In this figure, we see that the concave surface ("1" in Fig. 5.11) is erroneously divided into two parts ("1_a" and "1_b" in Fig. 5.13) in the extraction procedure of quasi wavefronts in SEABED algorithm. Furthermore, the phase compensation algorithm does not work for one of them although it works properly for the other. This is because the phase compensation algorithm requires the 2nd-order derivatives of quasi wavefronts, which can be unstable in noisy situation. Additionally, neither of the edge points are detected because of the same reason as in the case of 20dB. This result shows that the proposed algorithm requires a relatively high S/N, which is usually satisfied for the indoor applications considered in this paper. The estimation accuracy degrades for low S/N although the averaging procedure of ϕ contribute to the stability of the algorithm to some extent. Further studies are required to make this algorithm applicable to situations with

90
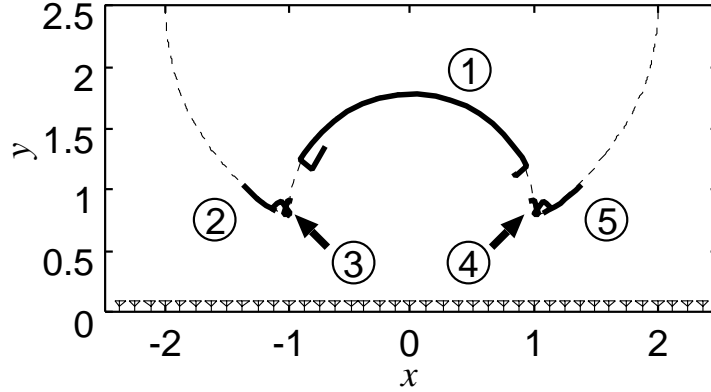
Figure 5.10: Phase compensated estimation.

Table 5.2: Average ϕ and shape determination.

Quasi wavefront	ϕ [degree]	Estimated shape
#1	28.1	concave
#2	64.3	convex
#3	42.4	concave
#4	42.7	concave
#5	66.9	convex

low S/N such as GPR (Ground Penetrating Radar) systems.

We have shown an application example of the proposed algorithm only for a target in Fig. 4.1. However, we have confirmed that the proposed algorithm is applicable for targets with any size of concave or convex structures as far as the reflected waves from such structures can be identified in the received signals. In addition, it is also applicable for an edge point because SEABED can deal with a diffraction wave. However, it is difficult to apply the proposed algorithm to targets which cause severe interference. This is because the proposed algorithm needs directly scattered wave including a reflection wave and diffraction wave from the target.

5.8   Conclusion

High-resolution shape estimation algorithms utilize the information of carrier phase. The estimation accuracy degrades on a certain condition because the carrier phase depends on the target shape. We proposed a phase compensation algorithm for SEABED algorithm. SEABED is a non-parametric algorithm of estimating target shapes for pulse radar
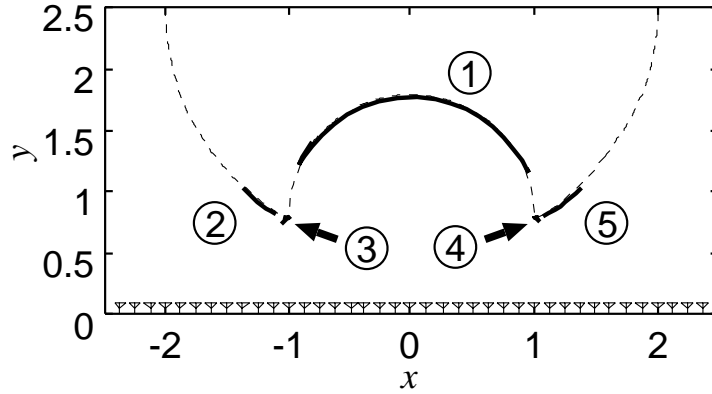
Figure 5.11: Estimation with a margin of decision for ϕ.
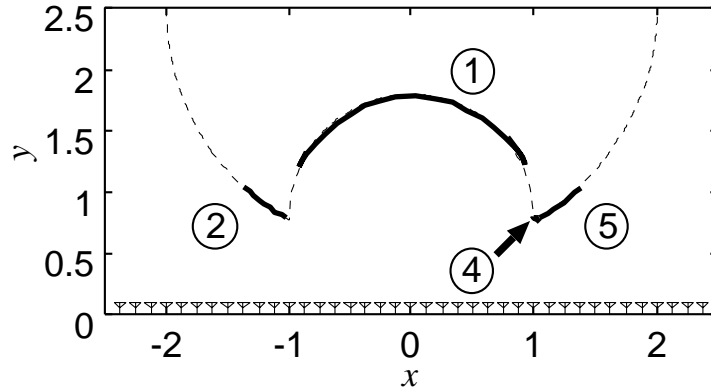
Figure 5.12: Estimated target shape for S/N=20dB.

systems. SEABED first extracts quasi wavefronts, which is suitable for phase compensation. We have clarified that phase compensation can be possible using a value ϕ which is calculated using a quasi wavefront and its 1st- and 2nd-order derivatives. We have modified IBST to compensate for phase rotation using ϕ. The modified IBST has a problem of instability of ϕ. We should note that ϕ suffers instability of 2nd-order derivative. We also modified the phase compensation algorithm to improve stability using averaged ϕ. The proposed phase compensation algorithm works well and estimated target surface accurately including its edge points.
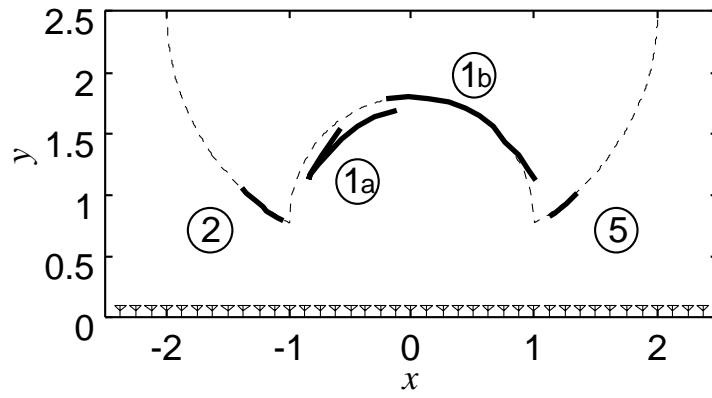
Figure 5.13: Estimated target shape for S/N=10dB.

Chapter 6

Non-Parametric 3-Dimensional Imaging Algorithm

6.1 Introduction

3-dimensional environment measurement is important issue for various applications including rescue robots. The imaging should be reliable if the algorithm affects a person's life. Pulse radar systems have an advantage that they work even in critical situations where optical measurement is not available. Estimating target shapes using data received by a scanned omni-directional antenna is known as one of ill-posed inverse problems. Conventional algorithms to solve this problem are not sufficient because their calculation time cannot be accepted. This problem is partly caused by the increase of the number of parameters in these algorithms. The 3-dimensional imaging requires even more parameters compared to the 2-dimensional imaging, which is a substantially serious problem.

We proposed a high-speed imaging algorithm for 2-dimensional systems in Chapter 3. The algorithm is based on Boundary scattering transform (BST), which is a reversible transform and can be used for direct estimation of target shapes. This transform can be easily extended from 2-dimension to 3-dimension. The calculation time can be considerably reduced compared to conventional algorithms. In this chapter, we propose a fast 3-dimensional imaging algorithm based on BST. Moreover, we show an application example of this algorithm to check the feasibility of the algorithm.

6.2 System Model

Most of the assumptions are the same as in the 2-dimensional problem. We assume a monostatic radar system in this chapter. We assume that each target has a uniform complex permittivity, and surrounded by a smooth boundary. An omni-directional antenna is scanned on a plane as in Fig. 6.1. Pulses are transmitted at a fixed interval and received
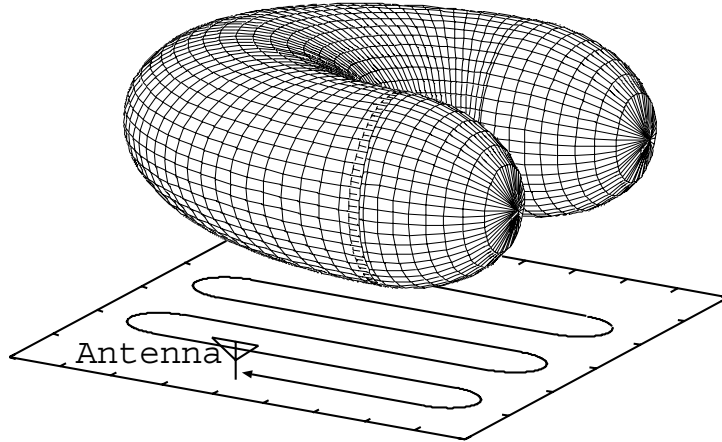
Figure 6.1: System model and antenna scanning.

by the same antenna. The received data is A/D converted and stored in a memory. We estimate target shapes using the data. The transmitted pulse is a mono-cycle pulse. We deal with 3-dimensional problems, and linear polarization.

We define r-space as the real space, where targets and the antenna are located. We express r-space with the parameter (x, y, z). All of x, y and z are normalized by λ, which is the center wavelength of the transmitted pulse in vacuum. We assume $z > 0$ for simplicity. The antenna is scanned on the plane spanned with x-axis and y-axis in r-space. We define $s'(X, Y, Z)$ as the received electric field at the antenna location $(x, y, z) = (X, Y, 0)$, where we define Z with time t and speed of the light c as $Z = ct/(2\lambda)$. We apply a matched filter of transmitted waveform to $s'(X, Y, Z)$. We define $s(X, Y, Z)$ as the output of the filter. We define d-space as the space expressed by (X, Y, Z). We normalize X and Y by λ and Z by the center period of transmitted waveform, respectively. It should be noted that the received data is expressed with (X, Y, Z) in d-space and target shapes are expressed with (x, y, z) in r-space. Transform from (X, Y, Z) to (x, y, z) corresponds to the imaging we deal with in this chapter.

6.3 Boundary Scattering Transform

We define q as the boundary surface which is expressed as a differentiable single-valued function. This assumption includes the case where the target complex permittivity is divided into multiple areas. This assumption is valid for most of artificial targets in the environment for household or rescue robots. We define several sets in order to explain Boundary scattering transform. We define P, which is a subset of d-space, as $P = \{(X, Y, Z) \,|\, \partial s(X, Y, Z)/\partial Z = 0, |s(X, Y, Z)| \geq T_s\}$, where T_s is a threshold to prevent picking up noise values. Next, we connect the points close to each other in P. We
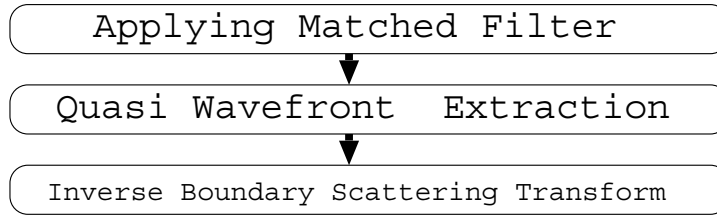
Figure 6.2: The outline of the proposed algorithm.

express each surface as p, which we call a quasi wavefront. We define G as the set of all $p \in P$. Here, we assume that the medium of direct path is vacuum, but the following argument is valid for any uniform media only if the propagation speed of the wave is known. We assume p corresponds to the direct scattered wave of q. By utilizing the relationship between the antenna location and the length of perpendicular line to q from the antenna location, the point (X, Y, Z) on p is expressed as

$$\begin{cases} X &= x + z\partial z/\partial x \\ Y &= y + z\partial z/\partial y \\ Z &= z\sqrt{1 + (\partial z/\partial x)^2 + (\partial z/\partial y)^2}, \end{cases} \qquad (6.1)$$

where (x, y, z) is a point on q, and we assume $z > 0$ and $Z > 0$. We define the transform in Eq. (6.1) as Boundary Scattering Transform (BST).

The inverse transform of BST is given by

$$\begin{cases} x &= X - Z\partial Z/\partial X \\ y &= Y - Z\partial Z/\partial Y \\ z &= Z\sqrt{1 - (\partial Z/\partial X)^2 - (\partial Z/\partial Y)^2}, \end{cases} \qquad (6.2)$$

which is obtained in the similar way as the 2-dimensional case. The existence of the inverse transform is very meaningful because it can be used for a direct and unique estimation of target boundary shapes. The estimated target boundaries are expressed not as an image but surfaces. This is the advantage and the characteristic of our algorithm. The condition of existence of IBST is differentiability of the quasi wavefront and $(\partial Z/\partial X)^2 + (\partial Z/\partial Y)^2 \leq 1$. This inequality is required because if it is not satisfied, the estimated z using IBST becomes an imaginary number, which is not rational.

6.4   3-Dimensional SEABED Algorithm

In this section, we propose a 3-dimensional imaging algorithm based on BST and IBST. We have already defined the set P. The procedure of extraction of P is easy because all

we should do is to check the derivative of given data. Next, we go on to the procedure of extracting p from P. In an actual procedure, we sequentially connect the points in P which satisfy a required condition. The i-th set p_i is determined as follows. The first element of p_i is an arbitrary element of P which is not included in $p_1, p_2, \cdots, p_{i-1}$. The domain I_i for p_i is set to (X, Y) of the first element. The second element of p_i is chosen from P which satisfies $(\partial Z / \partial X)^2 + (\partial Z / \partial Y)^2 \leq 1$. Here, Z should have only one value for the same (X, Y). Then, domain I_i is updated according to the newly chosen element. In this way, we expand the set p_i until there is no other element which can be included into p_i. Next, we calculate $\partial Z / \partial X$ and $\partial Z / \partial Y$ for an extracted quasi wavefront using a 2-dimensional B-spline smoothing algorithm. Finally, we apply IBST in Eq. (6.2) to the data and obtain an estimated target surface. Fig. 6.2 illustrates the outline of the algorithm we propose in this chapter.

6.5   Application Example

We show an application example of the proposed algorithm. The antenna transmits pulses at 51×51 positions with intervals of $\lambda / 4$. The assumed target is shown in Fig. 6.3. The inner part of the surface is filled with perfect electric conductor. The scanning plane is $z = 3$, which means the plane is 1λ apart from the nearest target surface. We obtain the received data $s(X, Y, Z)$ using a ray-tracing method, which cannot deal with the polarization and the phase rotation at caustics. First, we extract a quasi wavefront p from $s(X, Y, Z)$ as in Fig. 6.4. Next, we calculate $\partial Z / \partial X$ and $\partial Z / \partial Y$ in order to apply IBST to the data. The estimated target surface is shown in Fig. 6.5. As for the calculation time, the proposed algorithm with 51×51 positions takes 0.1 sec with a single Xeon 2.8GHz processor for the entire reconstruction. This procedure does not include the smoothing process with B-spline functions. Therefore, it is difficlt to directly compare the result with that of 2-dimensional SEABED algorithm.

6.6   Conclusion

In this chapter, we have proposed a new 3-dimensional imaging algorithm based on BST for pulse radar systems. BST is known as a reversible transform between target surfaces and received wave delay for 2-dimensional systems. We have extended BST to 3-dimensional systems and apply it for 3-dimensional imaging. First, we have shown the extended transform and its inverse transform. Secondly, we have proposed a 3-dimensional imaging algorithm based on BST. Finally, we have shown an application example of the proposed algorithm. We have clarified that the proposed algorithm's calculation time is considerably short compared to conventional algorithms, so that the proposed algorithm can be readily implemented to realtime applications. Additionally, the estimated target
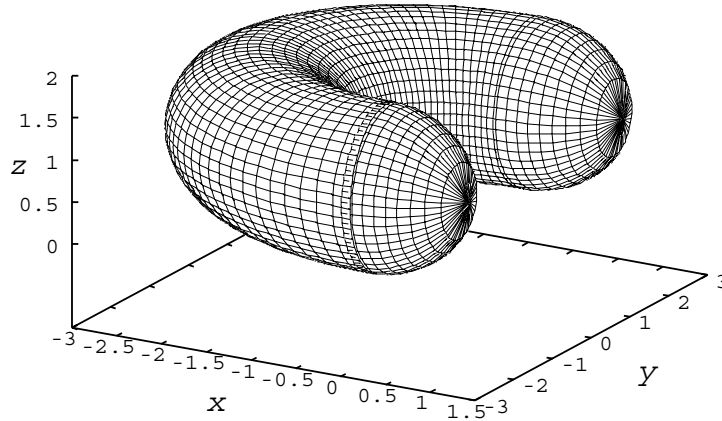
Figure 6.3: True target shape.

shape is accurate enough on the condition that the directly scattered waveform can be obtained. In this chapter, we have shown an application example without noise.

The echoes in 3-dimensional problems can suffer from phase rotation at caustics, which should be compensate for. However, in this chapter, we utilized ray-tracing method to obtain the simulated data, which does not include this effect. It is important to apply the phase compensation algorithm proposed in the previous chapter to 3-dimensional SEABED algorithm. Furthermore, investigating the performance of the proposed algorithm under noisy conditions will be an important future task.
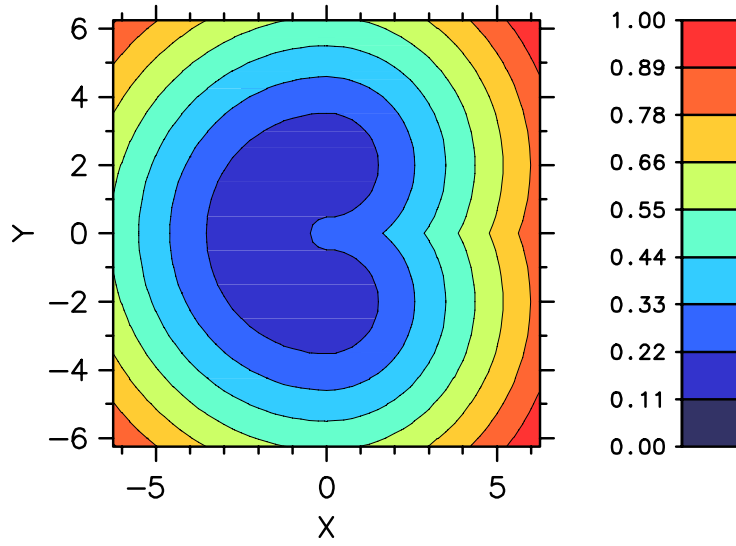
Figure 6.4: Extracted quasi wavefront.
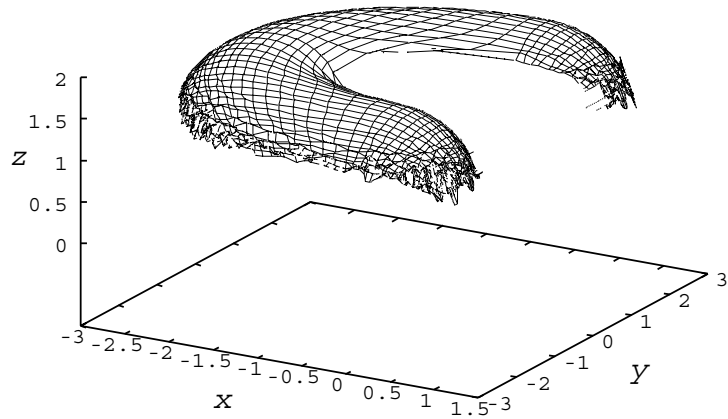
Figure 6.5: Estimated target shape. Computation time for the reconstruction is 0.1 sec.

Chapter 7

Concluding Remarks

In the present study, we have developed fast and accurate imaging algorithms for pulse radar systems. The IHCT algorithm and the SEABED (Shape Estimation Algorithm based on Boundary scattering transform and Extraction of Directly scattered waves) algorithm have been proposed and confirmed to have an efficient performance by numerical simulations. The IHCT algorithm simultaneously estimates the target location and scattered waveforms, whose accuracies are interdependent. The scattered waveforms are estimated using the coherent integration because the scattered waveforms depend on the target properties. The SEABED algorithm utilizes the existence of a pair of reversible transforms which connect the real space and the data space. The SEABED algorithm requires the condition as follows:

- Each target should have a uniform permittivity with a clear boundary.

- The propagation velocity should be known or at least estimated prior to its application.

These conditions are almost always satisfied for rescue robots and other applications which require shape estimation in the air. The SEABED algorithm can achieve a high-resolution shape estimation for 2-dimensional and 3-dimensional problems. Furthermore, we have improved the algorithm to avoid the problem of the phase shift caused by the concave scatterers. These problems were dealt with using analytic methods, which has led to concise closed-form numerical solutions.

In Chapter 2, the IHCT algorithm has been proposed to estimate target locations accurately. This algorithm is based on the iterative improvement which eliminates the inconsistency of target locations and scattered waveforms. Additionally, the algorithm implicitly extracts the narrow-band dominant frequency components which have high S/N compared to others. The estimation accuracy was compared with that of conventional methods and the theoretical lower bound CRLB (Cramer-Rao Lower Bound). The accuracy of the proposed algorithm was shown to be close to the CRLB, which indicates the

algorithm is the sub-optimal solution for the problem. Next, we clarified that some modifications for the IHCT algorithm are required to estimate multiple point targets although it has a remarkable performance for estimation of only one point target. This performance degradation of the IHCT algorithm is caused by the interference waves from other targets, which causes the erroneous estimation of the scattered waveforms. We proposed the interference suppression algorithm based on the neural networks, and confirmed its performance by numerical simulations.

In Chapter 3, the SEABED algorithm has been proposed for 2-dimensional fast and accurate imaging. First, we have shown that the reversible transform exists between a target shape and a delay time, which is named BST (Boundary Scattering Transform). The SEABED algorithm utilizes this transform for the estimation of target boundaries. This algorithm extracts quasi-wavefronts from the observed data, and IBST is applied to them. We have clarified that the SEABED has an advantage of direct estimation of target boundaries using the inverse transform, which is a mathematically complete solution for the inverse problem. The algorithm has a remarkable performance in estimating target shapes, which has been confirmed by numerical simulations. In addition, the performance of the SEABED algorithm against noisy environment has been investigated.

In Chapter 4, the performance of the SEABED algorithm for inhomogeneous media was shown. The performance of the SEABED algorithm for inhomogeneous media has not been touched in Chapter 3 because the SEABED algorithm was proposed with the assumption of homogeneity of the media. The inhomogeneity of the media is the typical model of soil, which is often dealt with in the field of GPRs (Ground Penetrating Radars). The performance was checked by applying the SEABED algorithm to random and layered media with a cylindrical perfect conductor.

In Chapter 5, the phase compensation algorithm for high-resolution imaging radar systems was proposed. The result of numerical simulation in Chapter 3 shows that there are offset errors at concave estimation, which is caused by the phase shift phenomenon. This phase shift phenomenon is well-known in the field of electromagnetic field theory, which has not been considered as a problem for a radar signal processing because the conventional radar systems do not discuss the accuracy of the order of its carrier wavelength. This problem is typical for UWB pulse radar systems because the UWB pulse has a relative bandwidth close to 100%. The phase shift was analytically studied and expressed with quasi-wavefronts, which enables us to modify the BST to compensate for the phase shift. The performance of the algorithm is clarified by numerical simulations, which shows it works well in a relatively high S/N environment.

In Chapter 6, the SEABED algorithm has been extended to 3-dimensional imaging, which we call the 3-D SEABED. The BST was also extended to deal with 3-dimensional imaging problems, which was used in the 3-D SEABED algorithm. The algorithm was proposed first, which was followed by the numerical simulations. We have clarified that the 3-dimensional imaging was accomplished quickly and accurately. The calculation time to obtain the entire image is 0.1 sec with a Xeon 2.8GHz processor.

In Chapter 6, we neglect the effect of the phase rotation at a caustic for simplicity. However, we have to apply the phase compensation algorithm to the 3-D SEABED by extending the phase compensation algorithm to a 3-dimensional one in future study. Some fast and accurate imaging algorithms have been proposed in this study, whose performances were confirmed only with numerical simulations. Further studies are needed to investigate the performance of the algorithms for experimental data. Additionally, polarimetry, which is one of the most important properties of the electromagnetic field, has not been used for imaging in this study. Combining the information of the polarization with the wavefronts can be a tremendous breakthrough for radar imaging techniques.

Appendix A

Optimum Signal Processing for Coherent Integrations

A.1 Optimum Signal Processing for Coherent Integrations

We define data vector $\boldsymbol{X}(\omega)$ as

$$\boldsymbol{X}(\omega) = \begin{bmatrix} S(\omega) + N_1(\omega) \\ S(\omega) + N_2(\omega) \\ \vdots \\ S(\omega) + N_M(\omega) \end{bmatrix}, \tag{A.1}$$

where $S(\omega)$ is a signal, and $N_i(\omega)$ are white Gaussian noises independent of one another.

We define $W(\omega)$ as a Wiener filter which output the Dirac delta function $\delta(t)$. We also define S_{ab} as the covariance matrices between a and b, where a and b are given matrices. For example, $S_{ab} = \mathrm{E}\{a^\mathrm{T}(\omega)b(\omega)\}$. We can express $W(\omega)$ as

$$\begin{aligned} W(\omega) &= S_{x\delta}(\omega)S_{xx}^{-1}(\omega) \tag{A.2} \\ &= \begin{bmatrix} \mathrm{E}\left\{1(S(\omega) + N_1(\omega))^*\right\} \\ \mathrm{E}\left\{1(S(\omega) + N_2(\omega))^*\right\} \\ \vdots \\ \mathrm{E}\left\{1(S(\omega) + N_M(\omega))^*\right\} \end{bmatrix} \\ &\cdot\ S_{xx}^{-1}(\omega). \tag{A.3} \end{aligned}$$

Here, we define

$$\begin{aligned} A &= \mathrm{diag}\{\sigma_1^2, \sigma_2^2, \cdots, \sigma_N^2\}, \tag{A.4} \\ \boldsymbol{v} &= \begin{bmatrix} S(\omega) & \cdots & S(\omega) \end{bmatrix}^\mathrm{T}. \tag{A.5} \end{aligned}$$

103

Then, we can express $W(\omega)$ as

$$
\begin{aligned}
W(\omega) \;=\;& S^*(\omega) \begin{bmatrix} 1 \\ 1 \\ \vdots \\ 1 \end{bmatrix} \\
& \cdot \left\{ A + |S(\omega)|^2 \begin{bmatrix} 1 & \cdots & 1 \\ \vdots & \ddots & \vdots \\ 1 & \cdots & 1 \end{bmatrix} \right\}^{-1}
\end{aligned}
\tag{A.6}
$$

$$
=\; S^*(\omega) \begin{bmatrix} 1 \\ 1 \\ \vdots \\ 1 \end{bmatrix} \left\{ A + \boldsymbol{v}\boldsymbol{v}^{\mathrm{H}} \right\}^{-1}
\tag{A.7}
$$

By applying the following formula for matrix inversion

$$
(A + \boldsymbol{v}\boldsymbol{v}^{\mathrm{H}})^{-1} = A^{-1} - \frac{A^{-1}\boldsymbol{v}\boldsymbol{v}^{\mathrm{H}}A^{-1}}{1 + \boldsymbol{v}^{\mathrm{H}}A^{-1}\boldsymbol{v}}
\tag{A.8}
$$

to Eq. (A.7), we obtain

$$
\begin{aligned}
W(\omega) \;=\;& \frac{1}{\displaystyle\sum_{j=1}^{M}\sigma_j^{-2}} \frac{S^*(\omega)}{|S(\omega)|^2 + \left(\displaystyle\sum_{j=1}^{M}\sigma_j^{-2}\right)^{-1}} \\
& \cdot \begin{bmatrix} \sigma_1^{-2} \\ \sigma_2^{-2} \\ \vdots \\ \sigma_M^{-2} \end{bmatrix}
\end{aligned}
\tag{A.9}
$$

And thus, we see the optimum signal processing require a weight in proportion to each signal power. This is the reason why we need a term $1/\sqrt{u(x, \boldsymbol{T}_i)}$ in Eq. (2.7).

A.2   Derivation of Eq. (5.2) and (5.3)

We show the derivation of Eq. (5.2) and (5.3) based on the reference papers [86, 87]. Helmholtz equation is given as

$$
\nabla^2 \boldsymbol{E} + k^2 \boldsymbol{E} = 0.
\tag{A.10}
$$

Eq. (5.1) can be expressed as

$$
\boldsymbol{E}(\boldsymbol{r}) \simeq \mathrm{e}^{-\mathrm{j}k\Phi(\boldsymbol{r})} \sum_{m=0}^{\infty} (-\mathrm{j}k)^{-m} \boldsymbol{E}_m(\boldsymbol{r})
\tag{A.11}
$$

104

using the vector $\boldsymbol{E}(\boldsymbol{r})$ of electric field. Substituting the asymptotic expression Eq. (A.11) into Eq. (A.10), we obtain the 0-th order transport equation as

$$(\nabla\Phi\cdot\nabla)\boldsymbol{E}_0 + \frac{1}{2}(\nabla^2\Phi)\boldsymbol{E}_0 = 0. \tag{A.12}$$

The general solution of Eq. (A.12) is

$$\boldsymbol{E}_0(\sigma) = \boldsymbol{E}_0(\sigma_0)\mathrm{e}^{-\frac{1}{2}\int_{\sigma_0}^{\sigma}\nabla^2\Phi\,\mathrm{d}\sigma}, \tag{A.13}$$

where σ is the length along a lay path. $\nabla^2\Phi$ is expressed as

$$\nabla^2\Phi = \frac{1}{\sigma} \tag{A.14}$$

with σ in the coordinates in Fig. 5.1. Finally, substituting Eq. (A.14) into Eq. (A.13), we obtain

$$\boldsymbol{E}_0(\sigma) = \boldsymbol{E}_0(\sigma_0)\sqrt{\sigma_0/\sigma}. \tag{A.15}$$

Eq. (A.15) can easily lead to Eq. (5.2) and (5.3). Here, we should note that 2-dimensional TE-mode wave has only one component which can be expressed using a scalar variable.

A.3 Derivation of Eq. (5.11) and (5.12)

We show the derivation of Eq. (5.11) and (5.12) in this section. First, let us define $\boldsymbol{v}_\mathrm{f}$ as

$$\boldsymbol{v}_\mathrm{f} = \begin{bmatrix} x_\mathrm{f} \\ y_\mathrm{f} \end{bmatrix} - \begin{bmatrix} x \\ y \end{bmatrix}. \tag{A.16}$$

$\boldsymbol{v}_\mathrm{f}$ should satisfy the conditions such as

$$|\boldsymbol{v}_\mathrm{f}| = r_\mathrm{c}, \text{and} \tag{A.17}$$

$$\boldsymbol{v}_\mathrm{f} \parallel \boldsymbol{v}_\mathrm{n}, \tag{A.18}$$

where r_c and $\boldsymbol{v}_\mathrm{n}$ are the radius of curvature and the normal vector of a target boundary surface, respectively. The radius of curvature of a target boundary surface is given as

$$r_\mathrm{c} = \frac{\left\{1 + (\mathrm{d}y/\mathrm{d}x)^2\right\}^{3/2}}{|\mathrm{d}^2y/\mathrm{d}x^2|}. \tag{A.19}$$

The normal vector of a target boundary surface is given as

$$\boldsymbol{v}_\mathrm{n} = \frac{\mathrm{d}^2y/\mathrm{d}x^2}{|\mathrm{d}^2y/\mathrm{d}x^2|\sqrt{1 + (\mathrm{d}y/\mathrm{d}x)^2}} \begin{bmatrix} -\mathrm{d}y/\mathrm{d}x \\ 1 \end{bmatrix}. \tag{A.20}$$

Therefore, we can conclude that $\boldsymbol{v}_\mathrm{f}$ can be expressed as

$$\boldsymbol{v}_\mathrm{f} = \frac{1 + (\mathrm{d}y/\mathrm{d}x)^2}{\mathrm{d}^2y/\mathrm{d}x^2} \begin{bmatrix} -\mathrm{d}y/\mathrm{d}x \\ 1 \end{bmatrix}. \tag{A.21}$$

Finally, the caustic curve $[x_\mathrm{f}, y_\mathrm{f}]$ is expressed as in Eq. (5.11) and (5.12).

A.4　Derivation of Eq. (5.14)

Differentiating the both sides of Eq. (5.13) with regard to x, we obtain

$$\frac{\mathrm{d}^2 y}{\mathrm{d}x^2} = \frac{\dfrac{\mathrm{d}^2 Y}{\mathrm{d}X^2}}{\left\{ 1 - \left(\dfrac{\mathrm{d}Y}{\mathrm{d}X}\right)^2 \right\}^{3/2}} \frac{\mathrm{d}X}{\mathrm{d}x}. \tag{A.22}$$

In order to obtain $\mathrm{d}X/\mathrm{d}x$ in the right hand side of Eq. (A.22), we have to differentiate the both sides of Eq. (5.4) with regard to x. We utilize a chain rule to get a derivative as

$$\frac{\mathrm{d}X}{\mathrm{d}x} = \frac{\partial X}{\partial x} + \frac{\partial X}{\partial y}\frac{\mathrm{d}y}{\mathrm{d}x} + \frac{\partial X}{\partial(\mathrm{d}y/\mathrm{d}x)}\frac{\mathrm{d}^2 y}{\mathrm{d}x^2}. \tag{A.23}$$

Substituting Eq. (5.4) into Eq. (A.23), we obtain

$$\mathrm{d}X/\mathrm{d}x = 1 + (\mathrm{d}y/\mathrm{d}x)^2 + y\mathrm{d}^2 y/\mathrm{d}x^2. \tag{A.24}$$

Next, substituting Eq. (A.24) into Eq. (A.22), we obtain

$$\frac{\mathrm{d}^2 y}{\mathrm{d}x^2} = \frac{\mathrm{d}^2 Y}{\mathrm{d}X^2} \frac{\left\{ 1 + (\frac{\mathrm{d}y}{\mathrm{d}x})^2 + y\frac{\mathrm{d}^2 y}{\mathrm{d}x^2} \right\}}{\left\{ 1 - \left(\frac{\mathrm{d}Y}{\mathrm{d}X}\right)^2 \right\}^{3/2}}. \tag{A.25}$$

Solving Eq. (A.25) for $\mathrm{d}^2 y/\mathrm{d}x^2$, we obtain

$$\frac{\mathrm{d}^2 y}{\mathrm{d}x^2} = \frac{\frac{\mathrm{d}^2 Y}{\mathrm{d}X^2}\left\{ 1 + (\frac{\mathrm{d}y}{\mathrm{d}x})^2 \right\}}{\left\{ 1 - \left(\frac{\mathrm{d}Y}{\mathrm{d}X}\right)^2 \right\}^{3/2} - y\frac{\mathrm{d}^2 Y}{\mathrm{d}X^2}}. \tag{A.26}$$

Finally, substituting Eq. (5.7) and (5.13) into Eq. (A.26), we obtain Eq. (5.14).

Bibliography

[1] M. Hebert, "Active and passive range sensing for robotics," *Proc. Int. Conf. on Robotics and Automation*, pp. 102–110, Apr. 2000.

[2] S. Nobuhara and T. Matsuyama, "Dynamic 3D shape from multi-viewpoint images using deformable mesh model," *Proc. IEEE*, pp. 192–197, Sep. 2003.

[3] T. S. Huang and A. N. Netravali, "Motion and structure from feature correspondences: A review," *Proc. IEEE*, vol. 82, no. 2, pp. 252–268, Feb. 1994.

[4] K. Sakaue, A. Amano, and N. Yokoya, "Optimization approaches in computer vision and image processing," *IEICE Trans. Inf. & Syst.*, vol. E82-D, no. 3, pp. 534–547, 1999.

[5] H. Jeong and Y. Oh, "Fast stereo matching using constraints in discrete space," *IEICE Trans. Inf. & Syst.*, vol. E83-D, no. 7, pp. 1592–1600, 2000.

[6] U. R. Dhond and J. K. Aggarwal, "Structure from stereo — A review," *IEEE Trans. Syst. Man. & Cybern.*, vol. 19, no. 6, pp. 1489–1510, 1989.

[7] N. Yokoya, T. Shakunaga, and M. Kanbara, "Passive range sensing techniques: Depth from images," *IEICE Trans. Inf. & Syst.*, vol. E82-D, no. 3, pp. 523–533, 1999.

[8] Y. Yagi, "Omnidirectional sensing and its applications," *IEICE Trans. Inf. & Syst.*, vol. E82-D, no. 3, pp. 548–557, 1999.

[9] T. Joochim and K. Chamnongthai, "Mobile robot navigation by wall following using polar coordinate image from omnidirectional image sensor," *IEICE Trans. Inf. & Syst.*, vol. E85-D, no. 1, pp. 264–274, 2002.

[10] H. Ukida and K. Konishi, "3D shape reconstruction using three light sources in image scanner," *IEICE Trans. Inf. & Syst.*, vol. E84-D, no. 12, pp. 1713–1721, 2001.

[11] S. Ozawa, "Image processing for intelligent transport systems," *IEICE Trans. Inf. & Syst.*, vol. E82-D, no. 3, pp. 629–636, 1999.

[12] J. T. Ylitalo and H. Ermert, "Ultrasound synthetic aperture imaging: Monostatic approach," *IEEE Trans. Ultrasonics, Ferroelectrics, & Freq. Control*, vol. 41, no. 3, pp. 333–339, May 1994.

[13] A. E. Yagle and J. L. Frolik, "On the feasibility of impulse reflection response data for the two-dimensional inverse scattering problem," *IEEE Trans. Antennas Propagat.*, vol. 44, no. 12, pp. 1551–1564, 1996.

[14] G. R. Lockwood, J. R. Talman, and S. S. Brunke, "Real-time 3-D ultrasound imaging using sparse synthetic aperture beamforming," *IEEE Transactions on Ultrasonics, Ferroelectrics, and Frequency control*, vol. 45, no. 4, pp. 980–988, July 1998.

[15] M. M. Bronstein, A. M. Bronstein, M. Aibulevsky, and H. Azhari, "Reconstruction in diffraction ultrasound tomography using nonuniform FFT," *IEEE Trans. Medical Imaging*, vol. 21, no. 11, pp. 1395–1401, 2002.

[16] I. Catapano and L. Crocco, "A simple two-dimensional inversion technique for imaging homogeneous targets in stratified media," *Radio Sci.*, vol. 39, no. RS1012, 2004.

[17] P. D. Walker and M. R. Bell, "Noniterative techniques for GPR imaging through a nonplaner air-ground interface," *IEEE Trans. Geoscience & Remote Sensing*, vol. 40, no. 10, pp. 2213–2223, Oct. 2002.

[18] R. J.-M. Cramer, R. A. Scholtz, and M. Z. Win, "Evaluation of an ultra-wide-band propagation channel," *IEEE Trans. Antennas Propagat.*, vol. 50, no. 5, pp. 561–570, 2002.

[19] G. F. Ross, *Transmission and reception system for generating and receiving baseband duration pulse signals for short base-band pulse communications system*. U. S. Patent 3,728,632, 1973.

[20] K. S. Kunz and R. J. Luebbers, *The Finite Difference Time Domain Method for Electromagnetics*. CRC Press, 1993.

[21] T. Suzuki and I. Arai, "Advance on underground radars," *IEICE Trans. Commun.*, vol. E74-B, no. 2, pp. 289–294, Feb. 1991.

[22] K. Suwa and M. Iwamoto, "Bandwidth extrapolation technique for polarimetric radar data," *IEICE Trans. Commun.*, vol. E87-B, no. 2, pp. 326–334, 2004.

[23] G. P. Otto and W. C. Chew, "Microwave inverse scattering - local shape function imaging for improved resolution of strong scatterers," *IEEE Trans. Microwave Theory & Tech.*, vol. 42, no. 1, pp. 137–142, 1994.

[24] R. Ferraye, J.-Y. Dauvignac, and C. Pichot, "An inverse scattering method based on contour deformations by meas of a level set method using frequency hoping technique," *IEEE Trans. Antennas Propagat.*, vol. 51, no. 5, pp. 1100–1113, 2003.

[25] H. Hung and M. Kaveh, "Focussing matrices for coherent signal-subspace processing," *IEEE Trans. Acoustics, Speach and Signal Processing*, vol. 36, no. 8, pp. 1272–1282, 1988.

[26] S. Sivanand, J. Yang, and M. Kaveh, "Focusing filters for wide-band direction finding," *IEEE Trans. Signal Processing*, vol. 39, no. 2, pp. 437–445, 1991.

[27] G. Gelli and L. Izzo, "Cyclostationarity-based coherent methods for wideband-signal source location," *IEEE Trans. Signal Processing*, vol. 51, no. 10, pp. 2471–2482, 2003.

[28] R. O. Schmidt, "Multiple emitter location and signal parameter estimation," *IEEE Trans. Antennas Propagat.*, vol. AP-34, pp. 276–280, 1988.

[29] M. Okada, T. Kaneko, and K. T. Miura, "Underground pipe signal extraction using LoG filter from pulse radar images," *IEICE Trans. Inf. & Syst.*, vol. E83-D, no. 1, pp. 112–115, 2000.

[30] E. Bermani, S. Caorsi, and M. Raffetto, "Microwave detection and dielectric characterization of cylindrical objects from amplitude-only data by means of neural networks," *IEEE Trans. Antennas Propagat.*, vol. 50, no. 9, pp. 1309–1314, 2002.

[31] J. C. Chen, R. E. Hudson, and K. Yao, "Maximum-likelihood source localization and unknown sensor location estimation for wideband signals in the near-field," *IEEE Trans. Signal Processing*, vol. 50, no. 8, pp. 1843–1854, 2002.

[32] K. Nagamune, K. Taniguchi, S. Kobashi, and Y. Hata, "Automated extraction system of embedded tubes from pulse radar image based on fuzzy expert system," *IEICE Trans. Fundamentals*, vol. E86-A, no. 7, pp. 1778–1789, 2003.

[33] T. Miwa and I. Arai, "Application of MUSIC algorithm to localization of cylindrical targets using cross borehole radar measurement," *IEICE Trans. Commun.*, vol. E87-B, no. 4, pp. 975–983, 2004.

[34] ——, "Super-resolution imaging for point reflectors near transmitting and receiving array," *IEEE Trans. Antennas Propagat.*, vol. 52, no. 1, pp. 220–229, 2004.

[35] S. Liu and M. Sato, "Electromagnetic logging technique based on borehole radar," *IEEE Trans. Geosci. Remote Sensing*, vol. 40, no. 9, pp. 2083–2092, 2002.

[36] A. Quinquis, E. Radoi, and F.-C. Ttir, "Some radar imagery results using superresolution techniques," *IEEE Trans. Antennas Propagat.*, vol. 52, no. 5, pp. 1230–1244, 2004.

[37] J. P. Fitch, *Synthetic Aperture Radar.* New York, Springer-Verlag, 1988.

[38] W. M. Boerner and Y. Yamaguchi, "Wideband polarimetry, interferometry and polarimetric interferometry in synthetic aperture remote sensing," *IEICE Trans. Commun.*, vol. E83-B, no. 9, pp. 1906–1915, 2000.

[39] S. Cloude, K. P. Papathanassiou, and E. Pottier, "Radar polarimetry and polarimetric interferometry," *IEICE Trans. Electron.*, vol. E84-C, no. 12, pp. 1814–1822, 2001.

[40] E. J. Bond, X. Li, S. C. Hagness, and B. D. van Veen, "Microwave imaging via space-time beamforming for early detection of breast cancer," *IEEE Trans. Antennas Propagat.*, vol. 51, no. 8, pp. 1690–1705, 2003.

[41] R. M. Narayanan, X. Xu, and J. A. Henning, "Radar penetration imaging using ultra-wideband (UWB) random noise waveforms," *IEE Proc.-Radar Sonar Navig.*, vol. 151, no. 3, pp. 143–148, 2004.

[42] D. L. Mensa, G. Heidbreder, and G. Wade, "Aperture synthesis by object rotation in coherent imaging," *IEEE Trans. Nuclear Science*, vol. 27, no. 2, pp. 989–998, Apr. 1980.

[43] J. Fortuny, "An efficient 3-D near-field ISAR algorithm," *IEEE Trans. Aerospace & Electronic Systems*, vol. 34, no. 4, pp. 1261–1270, Oct. 1998.

[44] A. Broquetas, J. Palau, L. Jofre, and A. Cardama, "Spherical wave near-field imaging and radar cross-section measurement," *IEEE Trans. Antennas Propagat.*, vol. 46, no. 5, pp. 730–735, May 1998.

[45] A. Franchois and C. Pichot, "Microwave imaging — Complex permittivity reconstruction with a Levenberg-Marquardt method," *IEEE Trans. Antennas Propagat.*, vol. 45, no. 2, pp. 203–215, 1997.

[46] A. Abubakar, P. M. Berg, and B. J. Kooij, "A conjugate gradient contrast source technique for 3D profile inversion," *IEICE Trans. Electron.*, vol. E83-C, no. 12, pp. 1864–1874, 2000.

[47] S. D. Rajan and G. V. Frisk, "A comparison between the Born and Rytov approximations for the inverse backscattering problem," *Geophysics*, vol. 54, no. 7, pp. 864–871, 1989.

[48] A. J. Devaney, "Geophysical diffraction tomography," *IEEE Trans. Geosci. Remote Sensing*, vol. 22, no. 1, pp. 3–13, 1984.

[49] C. Pichot, L. Jofre, G. Peronnet, and J. C. Bolomey, "Active microwave imaging of inhomogeneous bodies," *IEEE Trans. Antennas Propagat.*, vol. 33, no. 4, pp. 416–425, 1985.

[50] D. Nahamoo, S. X. Pan, and A. C. Kak, "Synthetic aparture diffraction tomography and its interpolation-free computer implementation," *IEEE Trans. Sonics and Ultrasonics*, vol. 31, no. 4, pp. 218–229, 1984.

[51] N. V. Budko, R. F. Remis, and P. M. Berg, "Two-dimensional imaging and effective inversion of a three-dimensional buried object," *IEICE Trans. Electron.*, vol. E83-C, no. 12, pp. 1889–1895, 2000.

[52] M. S. Zhdanov and S. Fang, "Three-dimensional quasilinear electromagnetic inversion," *Radio Sci.*, vol. 31, no. 4, pp. 741–754, 1996.

[53] C. Zhou and L. Liu, "Radar-diffraction tomography using the modified quasi-linear approximation," *IEEE Trans. Geosci. Remote Sensing*, vol. 38, no. 1, pp. 404–415, 2000.

[54] T. J. Cui, Y. Qin, G. L. Wang, and W. C. Chew, "High-order inversion formulas for low-frequency imaging of 2D buried targets," *Proceedings of 2004 IEEE Antennas and Propagation Society International Symposium*, vol. 1, pp. 189–192, 2004.

[55] W. C. Chew and Y. M. Wang, "Reconstruction of two dimensional permittivity distribution using the distorted Born iterative method," *IEEE Trans. Med. Imaging*, vol. 9, no. 2, pp. 218–225, 1990.

[56] A. Roger, "Newton-Kantorovitch algorithm applied to an electromagnetic inverse problem," *IEEE Trans. Antennas Propagat.*, vol. 29, no. 3, pp. 232–238, 1981.

[57] C. C. Chiu and Y. W. Kiang, "Microwave imaging of multiple conducting cylinders," *IEEE Trans. Antennas Propagat.*, vol. 40, no. 8, pp. 933–941, 1992.

[58] P. Lobel, R. E. Kleinman, C. Pichot, L. Blanc-Feraud, and M. Barlaud, "Conjugate-gradient method for solving inverse scattering with experimental data," *IEEE Antennas and Propagation Magazine*, vol. 38, no. 3, pp. 48–51, June 1996.

[59] P. Lobel, C. Pichot, L. Blanc-Feraud, M. Barlaud, and A. K. Louis, "Image reconstruction from the 1997 Ipswich data using a conjugate-gradient algorithm," *IEEE Antennas and Propagation Magazine*, vol. 41, no. 1, pp. 48–51, Feb. 1999.

[60] P. Lobel, C. Pichot, L. Blanc-Feraud, and M. Barlaud, "Microwave imaging: Reconstructions from experimental data using conjugate gradient and enhancement by edge-preserving regularization," *International Journal of Imaging Systems and Technology*, vol. 8, no. 4, pp. 337–342, Dec. 1998.

[61] C. Dourthe, C. Pichot, J. Y. Dauvignac, L. Blanc-feraud, and M. Barlaud, "Regularized bi-conjugate gradient algorithm for tomographic reconstruction of buried objects," *IEICE Trans. Electron.*, vol. E83-C, no. 12, pp. 1858–1863, 2000.

[62] M. Moghaddam and W. C. Chew, "Study of some practical issues in inversion with the Born iterative method using time-domain data," *IEEE Trans. Antennas Propagat.*, vol. 41, no. 2, pp. 177–184, 1993.

[63] P. Chaturvedi and R. G. Plumb, "Electromagnetic imaging of underground targets using constrained optimization," *IEEE Trans. Geosci. Remote Sensing*, vol. 33, no. 3, pp. 551–561, 1995.

[64] Y. Yu, T. Yu, and L. Carin, "Three-dimensional inverse scattering of a dielectric target embedded in a lossy half-space," *IEEE Trans. Geosci. Remote Sensing*, vol. 42, no. 5, pp. 957–973, 2004.

[65] T. B. Hansen and P. M. Johansen, "Inversion scheme for monostatic ground penetrating radar that takes into account the planar air-soil interface," *IEEE Trans. Geosci. Remote Sensing*, vol. 38, no. 1, pp. 496–506, Jan. 2000.

[66] T. J. Cui and W. C. Chew, "Diffraction tomographic algorithm for the detection of three-dimensional objects buried in a lossy half space," *IEEE Trans. Antennas Propagat.*, vol. 50, no. 1, pp. 42–49, Jan. 2002.

[67] T. J. Cui, W. C. Chew, X. X. Yin, and W. Hong, "Study of resolution and super resolution in electromagnetic imaging for half-space problems," *IEEE Trans. Antennas Propagat.*, vol. 52, no. 6, pp. 1398–1411, 2004.

[68] J. V. Candy and C. Pichot, "Active microwave imaging : A model-based approach," *IEEE Trans. Antennas Propagat.*, vol. 39, no. 3, pp. 285–290, 1991.

[69] P. Chaturvedi and R. G. Plumb, "Electromagnetic imaging of underground targets using constrained optimization," *IEEE Trans. Geosci. Remote Sensing*, vol. 33, no. 3, pp. 551–561, 1995.

[70] H. Harada, D. Wall, T. Takenaka, and M. Tanaka, "Conjugate gradient method applied to inverse scattering problem," *IEEE Trans. Antennas Propagat.*, vol. 43, no. 8, pp. 784–792, 1995.

[71] T. Sato, K. Takeda, T. Nagamatsu, T. Wakayama, I. Kimura, and T. Shinbo, "Automatic signal processing of front monitor radar for tunnelling machines," *IEEE Trans. Geosci. Remote Sensing*, vol. 35, no. 2, pp. 354–359, 1997.

[72] T. Sato, T. Wakayama, and K. Takemura, "An imaging algorithm of objects embedded in a lossy dispersive medium for subsurface radar data processing," *IEEE Trans. Geosci. Remote Sensing*, vol. 38, no. 1, pp. 296–303, 2000.

[73] I. T. Rekanos, T. V. Yioultsis, and T. D. Tsiboukis, "Inverse scattering using the finite-element method and a nonlinear optimization technique," *IEEE Trans. Microwave Theory & Tech.*, vol. 47, no. 3, pp. 336–344, 1999.

[74] C. C. Chiu and W. T. Chen, "Electromagnetic imaging for an imperfectly conducting cylinder by the genetic algorithm," *IEEE Trans. Microwave Theory & Tech.*, vol. 48, no. 11, pp. 1901–1905, 2000.

[75] C. Chiu, C. Li, and W. Chan, "Image reconstruction of a buried conductor by the genetic algorithm," *IEICE Trans. Electron.*, vol. E84-C, no. 12, pp. 1946–1951, 2001.

[76] T. Takenaka, H. Jia, and T. Tanaka, "Microwave imaging of an anisotropic cylindrical object by a forward-backward time-stepping method," *IEICE Trans. Electron.*, vol. E84-C, no. 12, pp. 1910–1916, 2001.

[77] A. Qing and C. K. Lee, "A study on improving the convergence of the real-coded genetic algorithm for electromagnetic inverse scattering of multiple perfectly conducting cylinders," *IEICE Trans. Electron.*, vol. E85-C, no. 7, pp. 1460–1471, 2002.

[78] A. Qing, "Electromagnetic imaging of two-dimensional perfectly conducting cylinders with transverse electric scattered field," *IEEE Trans. Antennas Propagat.*, vol. 50, no. 12, pp. 1787–1794, 2002.

[79] ——, "Electromagnetic inverse scattering of multiple two-dimensional perfectly conducting objects by differential evoluation strategy," *IEEE Trans. Antennas Propagat.*, vol. 51, no. 6, pp. 1251–1262, 2003.

[80] ——, "Electromagnetic inverse scattering of multiple perfectly conducting cylinders by differential evoluation strategy with individuals in groups," *IEEE Trans. Antennas Propagat.*, vol. 52, no. 5, pp. 1223–1229, 2004.

[81] M. B. Dobrin and C. H. Savit, *Introduction to Geophysical Prospecting, Fourth Edition, publisher =*.

[82] C. J. Leuschen and R. G. Plumb, "A matched-filter-based reverse-time migration algorithm for grond-penetrating radar data," *IEEE Trans. Geoscience & Remote Sensing*, vol. 39, no. 5, pp. 929–936, May 2001.

[83] J. van der Kruk, C. P. A. Wapenaar, J. T. Fokkema, and P. M. van den Berg, "Three-dimensional imaging of multicomponent ground-penetrating radar data," *Geophysics*, vol. 68, no. 4, pp. 1241–1254, 2003.

[84] C. R. Rao, *Linear Statistical Inference and Its Applications*, 2nd ed. New York, Wiley, 1984.

[85] L. Cohen, "Time-frequency distributions – A review," *Proc. IEEE*, vol. 77, pp. 941–981, 1989.

[86] G. L. James, *Geometrical Theory of Diffraction for Electromagnetic Waves, IEE Electromagnetic waves series 1, Peter Peregrinus Ltd., UK.* IEE Electromagnetic waves series 1, Peter Peregrinus Ltd., UK, 2004.

[87] D. A. McNamara, C. W. I. Pistorius, and J. A. G. Malherbe, *Introduction to the Uniform Geometrical Theory of Diffraction.* Artech House, Boston, 1990.

[88] A. E. Siegman, *Lasers.* University Science Books, Mill Valley, 1986.

Major Publications

Refereed Papers

1. T. Sakamoto and T. Sato, "A Target Shape Estimation Algorithm for Pulse Radar Systems Based on Boundary Scattering Transform," *IEICE Transaction on Communications* Vol. E87-B, No. 5, pp. 1357–1365, May 2004.

2. T. Sakamoto and T. Sato, "An Estimation Algorithm of Target Location and Scattered Waveforms for UWB Pulse Radar Systems," *IEICE Transaction on Communications* Vol. E87-B, No. 6, pp. 1631–1638, June 2004.

3. T. Sakamoto and T. Sato, "A Phase Compensation Algorithm for High-Resolution Pulse Radar Systems," *IEICE Transaction on Communications* Vol. E87-B, No. 11, pp. 3314–3321, Nov. 2004.

Refereed Conference Proceedings

1. T. Sakamoto and T. Sato, "An estimation method of target location and scattered waveforms for UWB pulse radar systems," *Proc. 2003 IEEE International Geoscience and Remote Sensing Symposium*, pp. 4013–4015, Toulouse, France, July, 2003.

2. T. Sakamoto and T. Sato, "A fast algorithm of 3-dimensional imaging for pulse radar systems," *Proc. 2004 IEEE AP-S International Symposium and USNC/URSI National Radio Science Meeting*, Vol. 2, pp. 2099-2102, Monterey, California, USA, June, 2004.

3. T. Sakamoto and T. Sato, "A Phase Compensation Algorithm for High-Resolution Pulse Radar Systems," *Proc. 2004 International Symposium on Antennas and Propagation*, pp. 585–588, Sendai, Japan, Aug., 2004.

4. T. Sakamoto and T. Sato, "Fast imaging of a target in inhomogeneous media for pulse radar systems," *Proc. 2004 IEEE International Geoscience and Remote Sensing Symposium*, Vol. 3, pp. 2070–2073, Anchorage, USA, Sep., 2004.